Thrombocyte and Melanoma Cell Adhesion under Various Complex Flow Conditions

A dissertation by doctoral degree candidate

Mohammad Amin Fallah

Submitted to:

Faculty of Mathematic and Natural Sciences

Augsburg University

Ph.D. Advisers:

Prof. Dr. A. Wixforth

Prof. Dr. M. F. Schneider

Chair for Experimental Physics I
Physics Institute
Augsburg University
June 2011

First Referee:

Prof. Dr. A. Wixforth

Second Referee:

Univ.-Prof. Dr. S. W. Schneider

Examination Board:

Prof. Dr. A. Wixforth

Univ.-Prof. Dr. S. W. Schneider

Prof. Dr. B. Stritzker

Priv.-Doz. I. Goychuk

Expected Examination Date:

July,19th ,2011

Table of Contents

1.   Introduction: A Summary of Adhesion under Flow

1.1. Blood and the Microvascular System

The cardiovascular system consists of heart, blood vessels, and blood. One of the main functions of the system is to transport oxygen from long to the tissues and transporting the nutrients and hormones to various organs, in addition to bringing the waste products to the kidneys for filtration. Blood also contains cells of the immune system and transports them to sites of infection, and produces clots by supplying thrombocytes and coagulation factors following injury to blood vessels.

Transporting fluids over distances no matter how long needs pumps. The heart is a four-chambered pump consisting of muscle tissue that transports blood. It is divided into left and right sides. The right side of the heart receives blood from venous system and pumps it to lungs. Blood then passes into the left side of the heart, where it is pumped to the body. Oxygenated blood leaves the heart through arteries and returns to heart with low oxygen concentration via veins. Hence, the system of blood vessels can be described as being consisted of three sub-systems based on the vessel categories. The *arterial system* and the *venous system* as described above, and *microcirculation system* that is consisted of small blood vessels in which solutes and solvents are exchanged with tissue [1].

The structure of vascular system is adapted to its function. The arterial system is a high-pressure and high-flow-rate system. The system is highly adaptable duo to the complex structure of vessel. Blood vessels consist of endothelium, smooth muscle cells, and extracellular matrix. Arteries are consisted of three layers: the intima, the media, and the adventitia. The intima is composed of the endothelium and a layer of extracellular matrix consisting of proteoglycans and collagen. The media consists of extracellular matrix and smooth muscle cells beneath an internal elastic lamina, providing structure and elasticity to the vessel. Contraction and relaxation of the smooth muscle cells regulate the blood vessel's diameter. The adventitia is a layer of loose connective tissue, smooth muscle cells, and fibroblast. Capillaries and lymphatic vessels outer portion of the arterial wall are located within the adventitia. Capillaries are the sites of fluid and mass transfer between the blood and the tissue [1].

1.2.   Fluid Dynamics, Newtonian and non-Newtonian Fluids

1.2.1.   Forces on Fluid Elements

Forces acting on the control volume are divided into *body forces* and *surface forces*. Body forces such as gravity, and electromagnetic fields act on the entire fluid mass. Forces per unit area, acting on control volume surfaces, are known as *stresses*, with units of force per unit area. Stresses are tensors and each element of the tensor has two directional components associated with it. Stresses are represented as σ_{ij} or $\boldsymbol{\sigma}$, where index *i* refers to the plane on which the stress acts and the index *j* refers to the direction in which the stress acts.
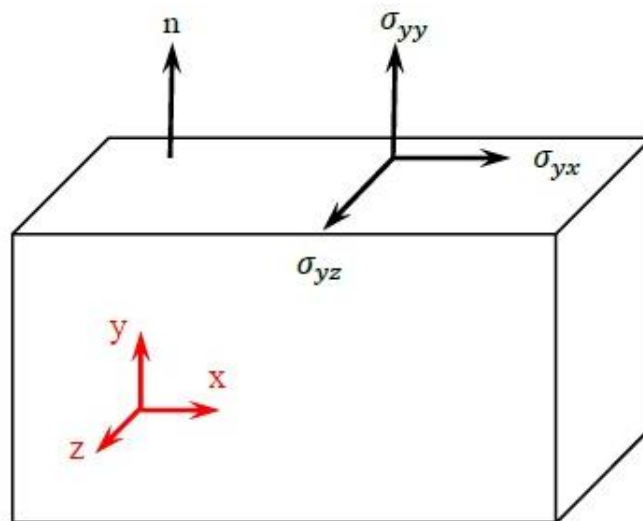
Fig.1.1. Cubic fluid element showing the stresses acting on a face of constant y.

Stresses act normal or tangential to a control volume surface. Tangential stresses are also known as *shear stresses*. An important fluid property is that a fluid at rest does not support a shear stress, so if a shear stress is applied to a fluid in rest, it will begin to flow. Pressure is the only stress that acts on a fluid at rest. Pressure is compressive and acts normal to the surface. At rest a point pressure is uniform in all directions. Due the distinction between stresses that can be supported statically and stresses under motion, the stress tensor σ is divided into two components as follows [1], [2]:

$$\boldsymbol{\sigma} = \text{-}p\mathbf{I} + \boldsymbol{\tau} \; . \tag{1.1}$$

Here, p is the pressure, $\boldsymbol{\tau}$ the so-called deviatoric stress, and I is the identity matrix. The matrix has diagonal elements of unit magnitude and off-diagonal elements equal to zero. The negative sign is introduced since the pressure acts as a compressive normal stress, that is parallel but in the opposite direction to normal vector to the surface [1], [2].

At the fluid-solid boundary, the "no-slip" condition for velocity is applied. This boundary condition expresses the fact that the fluid velocity tangent to the impermeable solid interface equals the velocity of the solid interface. Hence, the fluid elements closest to the solid wall are stationary, while the tangential velocity increases with distance from the wall [1-3].

1.2.2. Constitutive Relations

1.2.2.1. Newton's Law of Viscosity

In fluid mechanics, constitutive equations provide the needed relations between the shear stress and the fluid velocity. Unlike a conservative relationship, which is valid for all materials, a constitutive relationship is not universal and applies to a limited class of materials. Thus, Empirical measures are needed to derive constitutive relationships.The application of a shear stress to a control volume produces a deformation of the control volume. Assuming a change of angle $\Delta\theta$ in a time interval Δt, for a fixed time the increase in
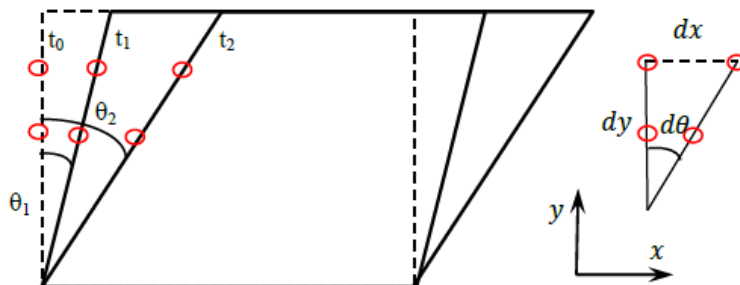
Fig.1.2. Left: Deformation of fluid volume exposed to a shear stress.
Right: Location of a material point after a time interval dt in a fluid
exposed to a shear stress τ_{xy}. [1]

shear stress results in an increase of the deformation angle of the fluid volume. An increase of the shear stress in a shorter time interval produces the same change in the deformation angle. Hence, the shear stress proportional to the rate of deformation, not the deformation itself. The rate of deformation ($d\theta/dt$) is sometimes called tangential rate of deformation [1].

Considering the change of location of a material element in a small time differential Δt after the application of a shear stress, we have:

$$\tan(\Delta\theta) = \Delta x/\Delta y \; . \tag{1.2}$$

For small changes in angle (i.e., $\Delta\theta \ll 30°$):

$$\tan(\Delta\theta) \approx \Delta\theta \; . \tag{1.3}$$

Since $\Delta x = \Delta V_x \, \Delta t$, we have:

$$\frac{\Delta\theta}{\Delta t} = \frac{\Delta v_x \Delta t}{\Delta t \Delta y} = \frac{\Delta v_x}{\Delta y} \; . \tag{1.4}$$

Or $\Delta t \to 0$

$$\frac{d\theta}{dt} = \frac{dv_x}{dy} \; . \tag{1.5}$$

The velocity gradient is known as the shear rate, $\dot{\gamma}_x$. Thus, the constitutive relation should adopt the following form:

$$\tau_{yx} = f(\dot{\gamma}_x) \tag{1.6}$$

Experimental data are needed to specify the form of the Equation (1.6) for a particular fluid. The simplest possible functional relationship, valid for many fluids, is a linear relation between shear stress and shear rate, as shown in *Newton's law of viscosity* [1-3]:

$$\tau_{yx} = \mu\dot{\gamma}_x = \mu \; \frac{dv_x}{dy} \; . \tag{1.7}$$

Where the coefficient of proportionality is the *viscosity*, μ. Fluids that obey Equation (1.7) are called *Newtonian fluids* [1-3].

Non-Newtonian Fluids

Rheology is a branch of mechanics that studies the deformation of fluids. The distinction between Newtonian and non-Newtonian fluids can be explained when looking into the relation between the shear stress and the shear rate. In general, the *apparent viscosity* is simply defined as the ratio [1]:

$$\eta_{app}(T, p, \dot{\gamma}_x) = \frac{\tau_{yx}}{\dot{\gamma}_x}.$$ (1.8)

The term *apparent viscosity* is used to indicate that, unlike a "true" fluid viscosity, as defined by Newton's law of viscosity, the ratio of the shear stress to the shear rate depends on the shear rate. For a Newtonian fluid, the apparent viscosity is constant for all ratios of shear stress and shear rate. With several classes of fluid have been defined on the basis of the relationship between the shear stress and the shear rate, as a few popular ones are explained below:

Newtonian Fluid: for which, the shear stress is proportional to the shear rate and the apparent viscosity equals the true viscosity ($\eta_{app} = \mu$), given by the formula (1.7). [1]

Bingham Plastic: A Bingham plastic is a material that has solid as well as fluid-like properties. It does not flow until the applied stress exceeds the yield stress, τ_0. Below that yield stress, the shear rate and velocity gradient vanish [1]:

$$|\tau_{yx}| < \tau_0 \qquad \dot{\gamma}_x = 0$$ (1.8)

Above the yield stress, the relationship between the shear stress and shear rate is:

$$|\tau_{yx}| > \tau_0 \qquad \tau_{yx} = \pm\tau_0 + \mu_0\dot{\gamma}_x$$ (1.9)

Where μ_0 depends upon the temperature and pressure and is independent of the shear rate. The sign in the Equation (1.9) is positive when the shear stress is positive and negative when the shear stress is negative. The condition is similar to the Newton law of viscosity, except that the fluid exhibits a yield stress.

Power Law Fluids: In general a power law fluid is a type of fluid for which the *apparent viscosity* is function of the shear rate raised to a power. For power law fluids, the apparent viscosity can be written as [1]:

$$\eta_{app} = \text{m } |\dot{\gamma}_x|^{n-1} \tag{1.10}$$

The quantities m and n depend on the particular fluid. One should note that n is dimensionless, but the units of m depend upon the value of n (g cm^{-1} s^{n-2}). Power law fluids are classified as follows:

n = 1: Newtonian fluid (m = μ)

n < 1: Shear-thining, or pseudoplastic fluid

n > 1: Shear-thickening, or dilatant fluid

High molecular weight polymers are shear-thining fluids. Slurries and suspensions are shear thickening fluids. Blood exhibits both shear-thinning behavior and a yield stress [1].

1.2.2.2.   Pressure Driven Flow

Since most of the problems in physiological fluid mechanics deal with incompressible Newtonian fluids, the generalized constitutive relationship developed for such fluids is applied in such situations [1]. Such fluid dynamic conditions are explained by Navier-Stokes equation:

$$\rho \frac{d\mathbf{v}}{dt} + \rho \mathbf{v}.\nabla \mathbf{v} = -\nabla p + \mu \nabla^2 \mathbf{v} + \rho g \tag{1.11}$$

In which μ is viscosity of the fluid. And the term $\mu \nabla^2 v$ is correlated to shear stress tensor and respectively to normal stress tensor:

$$\tau_{ij} = \mu \left(\frac{\partial v_i}{\partial x_j} + \frac{\partial v_i}{\partial x_j} \right) \tag{1.12}$$

$$\sigma_{xx} = -p + \mu \frac{dv}{dx} \tag{1.13}$$

The x component of the volume, Navier-Stokes equation reads:

$$\rho\left(\frac{\partial v_x}{\partial t} + v_x \frac{\partial v_x}{\partial x} + v_y \frac{\partial v_x}{\partial y} + v_z \frac{\partial v_x}{\partial z}\right) = -\frac{\partial p}{\partial x} + \mu\left[\frac{\partial^2}{\partial x^2}v_x + \frac{\partial^2}{\partial y^2}v_x + \frac{\partial^2}{\partial z^2}v_x\right] + \rho g \tag{1.14}$$

For an inviscid fluid the shear components in Navier-Stokes are zero, and just the surface force normal (σ) to interface remains. This is the hydrostatic pressure p:

$$-p = \sigma_{xx} = \sigma_{yy} = \sigma_{zz} \tag{1.15}$$

This leads to Euler equation:

$$\rho g - \nabla p = \rho \frac{D\mathbf{V}}{Dt} = \rho [\frac{d\mathbf{V}}{dt} + (\mathbf{V}.\nabla)\mathbf{V}] \tag{1.16}$$

1.2.2.2.1. Pressure Driven Flow through Narrow Rectangular Channels

Examining the pressure driven flow through a narrow rectangular channel of height h and width w, is vital, since this kind of ducts are often used in biomedical devices in order to study the effect of fluids dynamics of cell adhesion. We consider a parallel plate channel as described in Fig.1.3.
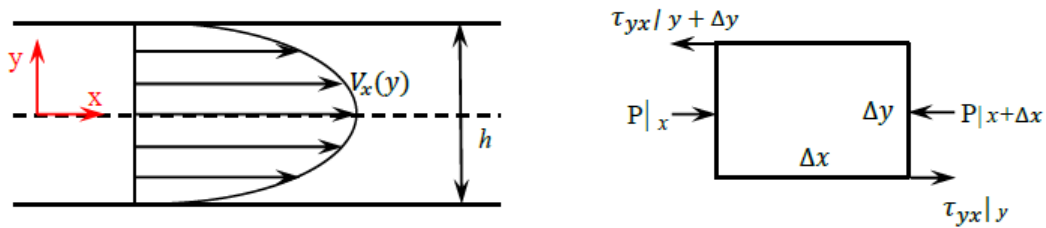
Fig. 1.3. Left: Pressure-driven flow through a rectangular channel with height of h, and width of w.
Right: Momentum balance applied to a cubic control volume.

Due to the no-slip boundary condition, the velocity is zero at either the upper or lower plates. Following assumptions simplify the analysis of the flow in such geometries [1]:

1. The fluid density is constant, which indicates the condition of incompressible fluid.
2. Pressure, shear stress, and velocity do not change with time, in other words, flow is steady.
3. The fluid is Newtonian.
4. Flow is fully developed. The prerequisite for a fully developed flow is that the channel length is much longer than the entrance length L_e where the velocity depends upon the axial distance along the channel, $L_e \ll L$. Hence, the shear stress and velocity field do not change along the x direction, so v_x is only a function of y.

5. Edge effects are neglected. To meet this assumption, one requires a long, wide channel, where $h/w \ll 1$, and $h/L \ll 1$.

6. The flow is laminar.

7. The pressure varies only in flow direction.

As shown in the control volume in Fig. 1.3, there is no net momentum flow and the flow is steady. Hence, the sum of all forces must equal zero, and the only forces arising are those due to pressure and shear stress. A momentum balance in the x direction yields

$$(P|x - P|x+\Delta x)\Delta x\Delta z + (\tau_{yx}|y + \Delta y - \tau_{yx}|y + \Delta y)\,\Delta x\Delta z = 0 \tag{1.17}$$

Dividing by $\Delta x\Delta y\Delta z$ and taking the limit as Δx, Δy, and Δz each to go to zero results in the following ordinary differential equation:

$$\frac{dp}{dx} = \frac{d\tau_{yx}}{dy} \tag{1.18}$$

The pressure changes only in the x direction ($p = f(x)$), and the shear stress varies in the y direction ($\tau_{yx} = g(y)$). Thus,

$$\frac{df(x)}{dx} = \frac{dg(y)}{dy} \tag{1.19}$$

The left- and the right-hand side of Equation (1.19) can be equal only if the derivatives are each equal to a constant C_1. Thus, the left side of Equation (1.20) can be integrated to yield

$$p = C_1 x + C_2 \tag{1.20}$$

The pressure can be specified at two locations, away from both entrance and exit. Hence, at $x = x_0$, $p = p_0$, and at $x = x_L$, $p = p_L$. Defining $\Delta p = p_0 - p_L$, and $x_L - x_0 = L$, we find that the pressure is

$$p = p_0 + \frac{\Delta p}{L}\,(x_0 - x) \tag{1.21}$$

and Equation (1.18) becomes

$$-\frac{\Delta p}{L} = \frac{d\tau_{yx}}{dy} \tag{1.22}$$

Integrating Equation (1.22) results in

$$\tau_{yx} = - \frac{\Delta p}{L} y + C_3 \qquad (1.23)$$

Since the velocity is known and the stresses are not defined on any boundary, one should determine the velocity and apply the boundary condition that at $y = \pm h/2$, $v_x = 0$. In order to find the velocity, one has to insert the Newton's law of viscosity, into Equation (1.23) to obtain

$$\mu \frac{dv_x}{dy} = - \frac{\Delta p}{L} y + C_3 \qquad (1.24)$$

After integrating Equation (1.18), one obtains

$$v_x = - \frac{\Delta p}{2\mu L} y^2 + \frac{C_3}{\mu} y + C_4 \qquad (1.25)$$

Applying the boundary results in $C_3 = 0$ and $C_4 = \Delta p h^2 / 8 \mu L$. The velocity profile is

$$v_x = \frac{\Delta p h^2}{8 \mu L} \left(1 - \frac{4y^2}{h^2} \right) \qquad (1.26)$$

Equation (1.26) describes parabola and the velocity is a maximum at $y = 0$ with a value of

$$v_{max} = \frac{\Delta p h^2}{8 \mu L} \qquad (1.27)$$

The Equation (1.21) can be written as

$$v_x = v_{max} \left(1 - \frac{4y^2}{h^2} \right) \qquad (1.28)$$

The volumetric flow rate is the integral of the velocity over the cross-sectional area through which fluid flows; that is,

$$Q = \int_{-h/2}^{h/2} \int_{0}^{w} v_x \, dz dy = v_{max} \, w \int_{-h/2}^{h/2} \left(1 - \frac{4y^2}{h^2} \right) dy \qquad (1.29)$$

or

$$Q = \frac{2 v_{max} w h}{3} \qquad (1.30)$$

13

The average velocity through the cross-section area A is

$$< v > = \frac{1}{A} \int_A v_x dA = \frac{1}{wh} \int_{-h/2}^{h/2} \int_0^w v_x \, dzdy \tag{1.31}$$

The volumetric flow rate can be written as

$$Q = < v > wh \tag{1.32}$$

To relate the average and maximum velocities for flow through a channel, equate Equation (1.30), (1.32)

$$< v > = \frac{2}{3} v_{max} \tag{1.33}$$

Since $C_3 = 0$, the shear stress, Equation (1.23), is

$$\tau_{yx} = - \frac{\Delta p}{L} \, y \tag{1.34}$$

The shear stress distribution τ_{yx} is sketched in Fig.1.4.
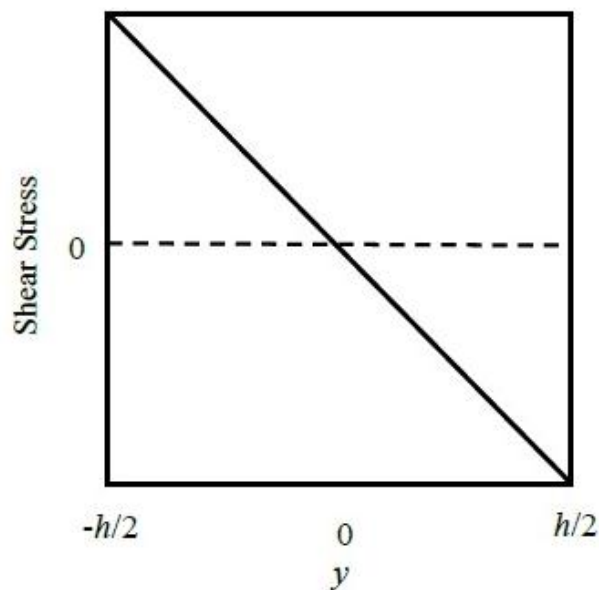
Fig.1.4. Shear stress distribution for flow between parallel plates.

1.2.2.2.2. Pressure-Driven Flow through a Cylindrical Tube

Laminar flow of a Newtonian fluid through a cylindrical tube arises in many biomedical applications, such as dialysis units, bioreactors, needles, infusion systems. This type of flow occurs in the cardiovascular system too, although the flow is often unsteady, and blood behaves as a non-Newtonian fluid.
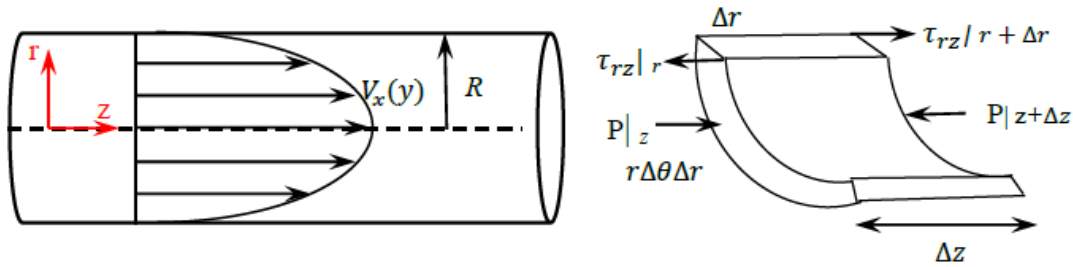
Fig.1.5. Left: Laminar flow of a Newtonian fluid through a cylinder of radius R. Right: Momentum balance on a differential volume r$\Delta\theta\Delta r\Delta z$.

Control volume and momentum balances are shown in Fig.1.5. Since there is no momentum flow due to the assumption of fully developed flow, and since the flow is considered to be steady, the sum of all forces is zero. The only arising forces are those due to pressure and shear stress, so we have [1]:

$$(P|_z - P|z+\Delta z)r\Delta\theta\Delta r + ((r + \Delta r)\ \tau_{rz}|\ r + \Delta r\ - \tau_{rz}|\ _r)\Delta\theta\Delta z = 0 \tag{1.35}$$

Deviding by $r\Delta\theta\Delta r\Delta z$, and taking the limit as Δr and Δz approach zero, together with using the definition of derivative, one finds out [1]:

$$-\frac{dp}{dz} = \frac{1}{r}\frac{d(r\tau_{rz})}{dr} \tag{1.36}$$

Where the expression on the left hand side simply equals to pressure drop over the length L of the tube, or

$$-\frac{dp}{dz} = \frac{\Delta p}{L} \tag{1.37}$$

This leads to

$$\frac{1}{r}\frac{d(r\tau_{rz})}{dr} = -\frac{\Delta p}{L} \qquad (1.38)$$

Which leads to calculation if the shear tensor as following:

$$\tau_{rz} = \mu \frac{dv_z}{dr} \qquad (1.39)$$

The velocity gradient would be

$$\frac{dv_z}{dr} = -\frac{\Delta pr}{2\mu L} \qquad (1.40)$$

Where the $\frac{\Delta p}{L}$ is the pressure drop over the length (L) of the tube. Applying no-slip boundary condition at $r = R$, the velocity profile reads:

$$v_z = \frac{\Delta pR^2}{4\mu L}\left(1 - \frac{r^2}{R^2}\right) \qquad (1.41)$$

The velocity is a parabolic function of radial position with a maximum value at $r = 0$.

$$v_{max} = \frac{\Delta pR^2}{4\mu L} \qquad (1.42)$$

The definition of the average velocity in cylindrical coordinates is the integral of the velocity over the cross-sectional area through which flow occurs, divided by the cross-sectional area, or

$$<v> = \frac{1}{A}\int_A v_z dA = \frac{1}{\pi R^2}\int_0^R\int_0^{2\pi} v_z\, rd\theta dr \qquad (1.43)$$

Using Equations (1.39) and (1.42), the average and maximum velocities are related as follows:

$$<v> = \frac{1}{2}v_{max} \qquad (1.44)$$

The volumetric flow rate Q equals $<v>\pi R^2$, so the flow rate reads

$$Q = \frac{\Delta p\pi R^4}{8\mu L} \qquad (1.45)$$

Equation (1.45) is in known as *Poiseuille's Law*.

Quantitive statements can be made about entrance effects. As the fluid enters a cylindrical tube, the velocity changes in the r and z directions. Variations in the z direction become insignificant for lengths greater than the entrance length L_e. This length has been measured experimentally for Newtonian fluids and found to be [1]:

$$L_e = 0.058 \, DRe \tag{1.46}$$

Where D is the inner diameter of the cylinder. For rectangular slits, the entry length must be greater than $0.04h\text{Re}$, where $\text{Re} = (<v> D_h) / \mu$, where [1]:

$$D_h = \frac{4\,(cross-sectional\ area)}{Perimeter} \tag{1.47}$$

1.2.2.2.3. Pressure Driven Flow of a Power Law Fluid in a Cylindrical Tube

Considering the flow of a power law fluid through a cylindrical tube, the momentum balance boundary conditions discusses in section 1.2.3.3.2 are still valid. Since the shear stress must be finite at $r = 0$, the integrated momentum balance is [1]:

$$\tau_{rz} = -\frac{\Delta pr}{2L} \tag{1.48}$$

The constitutive equation of power law fluid is

$$\tau_{rz} = m \left| \frac{dv_z}{dr} \right|^{n-1} \left(\frac{dv_z}{dr} \right) \tag{1.49}$$

The velocity is a maximum at the centerline and declines towards zero toward zero with increasing radial distance. Thus, the velocity gradient is negative, and

$$\tau_{rz} = -m \left| \frac{dv_z}{dr} \right|^{n} = -\frac{\Delta pr}{2L} \tag{1.50}$$

Rearranging Equation (1.51) in terms of the velocity gradients yields

$$\frac{dv_z}{dr} = - \left(\frac{\Delta p}{2mL} \right)^{1/n} r^{1/n} \tag{1.51}$$

By integration with respect to r, and applying the no-slip condition at $r = R$, the resulting velocity profile is

17

$$v_z = \left(\frac{\Delta p}{2mL}\right)^{1/n} \left(\frac{R^{1+1/n}}{1+1/n}\right) \left[1 - \left(\frac{r}{R}\right)^{1+1/n}\right] \tag{1.52}$$

For a Newtonian fluid, $m = \mu$, $n = 1$. [1]

Normalized velocity profiles for power law fluids are shown in Fig. 1.5. A Newtonian fluid serves as a reference. For a shear-thining fluid ($n < 1$), the apparent viscosity declines as the shear stress decreases. Thus, the viscosity is lower near the wall than near the centerline. As a result of the reduced viscosity near the wall, the viscosity increases with increasing shear rate, and the velocity is less than the corresponding velocity for the Newtonian fluid.[1]

The flow rate is obtained by multiplying the average velocity by the cross-sectional area πR^2 through which flow occurs:

$$Q = \frac{n\pi}{3n+1} \left(\frac{\Delta p}{2mL}\right)^{1/n} R^{(3n+1)/n} \tag{1.53}$$

1.3.   Hemostasis and Biophysics of Thrombocyte Adhesion

Bleeding at the site of vascular injury is a common phenomenon. The reason that a healthy human being normally does not suffer from hemorrhage or in strong contrast from hemostasis lies in the equilibrium between pro-coagulant and anti-coagulant mechanisms. Pro-coagulation mechanisms halt hemorrhage in case of injuries by formation of blood clots. After a successful halt of bleeding the anti-coagulant mechanism bring the equilibrium back to the vascular system by moving the system toward restoring the normal blood flow [5], [6]. Although, pro-coagulant mechanisms include platelet adhesion and aggregation, and fibrin clot formation, described thoroughly in literature [6-40], we would like to discuss the pro-coagulation in details here again in order to clarify their importance. Among the pro-coagulation factors, glycoprotein von Willebrand Factor (VWF) is of extreme importance due to its numerous interactions with other proteins and cells in microvascular system [10-48]. Thus, section 1.3.3 is dedicated to VWF. The natural inhibitors of coagulation and fibrinolysis are among the anticoagulation factors. Hemostasis is naturally regulated in order to maintain the blood flow. However, the nature of the phenomenon is to seal blood flow at the sites of vascular injury.
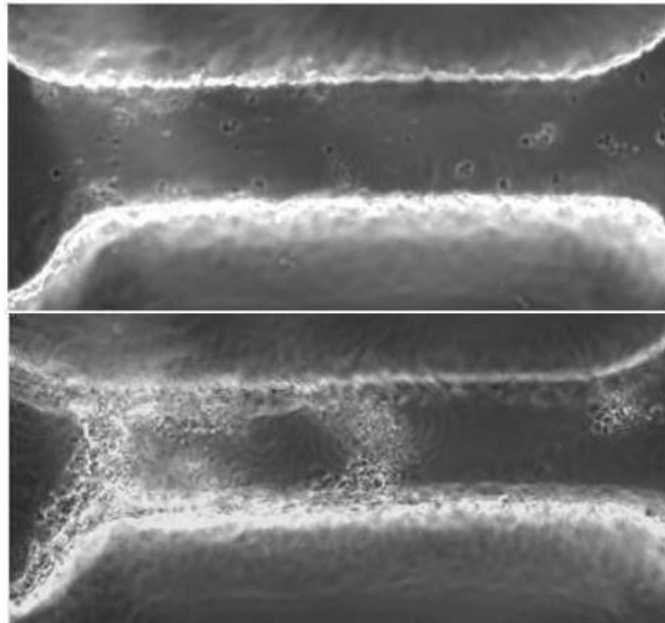
Fig.1.6. Above: Adhesion of single thrombocytes on the footprint of a microchannel coated with VWF under wall shear rate of 1000 s^{-1}. Bottom: VWF dependent thrombus formation on the channel footprint at 10000 s^{-1} after 4 minutes. The Platelets for these experiments are separated from whole blood and re-suspended in blood plasma. Images have been captured by a 20X objective, employing phase contrast microscopy.

1.3.1. Thrombotic Mechanisms

Platelets adhere to the sites of vascular injury. Their adhesion is primarily mediated by von Willebrand Factor, a large multimeric protein existing in both plasma and the extracellular matrix of the subendothelial vessel wall [6], [21], [24], [29]. Platelet adhesion can also be initiated by direct binding of thrombocytes to subendothelial collagen through specific platelet membrane collagen receptors. Platelet adhesion also leads to platelet activation and aggregation. Activated thrombocytes undergo the release reaction during which they secrete contents that further promote aggregation (platelet-platelet interaction), and inhibit the naturally anticoagulant endothelial cell factors. During platelet aggregation additional platelets adhere to the site of injury, leading to formation of a blocking platelet thrombus. Development of fibrin mesh stabilizes the platelet plug [6]. The most abundant receptor on the platelet surface is the platelet glycoprotein (Gp) IIb/IIIa with a concentration of 50000 fibrinogen binding sites per platelet. Platelet activation due to different reasons including

coming in contact with tissue, can cause a rapid formation of an occlusive platelet thrombus. Considering the normal hemostasis is consisted of different steps including *platelet plug formation* and *fibrin clot formation*. The former has been briefly explained above. However, in order to describe the latter one has to consider that the plasma coagulation proteins or the so called clotting normally circulate in plasma in their inactive form. Coagulation in initiated by tissue factor exposure. The immediate trigger for coagulation is vascular damage that exposes the blood to tissue factor that is expressed on the surface of subendothelial cellular components of the vessel wall, such as smooth muscle cells, and fibroblasts. The tissue factor is also present at in circulating microparticles, presumably released from cells including monocytes and platelets. Tissue factor (TF) together with *factor VIIa*, activates *factor IX* and factor *X,* which in turn with *factor VIII* and *factor V* as cofactors results in thrombin formation. Thrombin is an enzyme that converts soluble plasma fibrinogen to an insoluble fibrin matrix. Thrombin also activates *factor XIII* to *factor XIIIa*, which covalently cross-links and thereby stabilizes the fibrin clot [6].

1.3.2.   Antithrombotic Mechanisms

Clotting is prevented under normal circumstances by several physiological mechanisms. Endothelial cells have many antithrombotic effects. By producing platelet binding inhibitors like *prostacyclin*, *nitric oxide*…etc.; and producing anticoagulant factors including *heparin proteoglycans*, *antithrombin*, *tissue factor pathway inhibitor*, and *thrombomoduline*. Antithrombin is a major plasma protease inhibitor of thrombin and the other clotting factors in coagulation. Protein C is a plasma glycoprotein that becomes an anticoagulant when it is activated by thrombin, and the tissue factor pathway inhibitor (TFPI) is a plasma protease inhibitor that regulates the TF-.induced pathway of coagulation. Plasmin also works as major protease enzyme of fibrinolytic system, acting to digest fibrin to fibrin degradation products [6]. Size regulation of the VWF polymers that play an important role in thrombus formation and coming the *Rolling Platelet Aggregates* into existence is much dependent on metalloproteinase, *ADAMTS-13* [13], [14].

1.3.3. Von Willebrand Factor

Clotting initiation is very much dependent of a polymeric glycoprotein called *von Willebrand Factor* (VWF). VWF is required for normal hemostasis. Deficiency of VWF, also known as *von Willebrand Desease* (VWD), is the most common inherited bleeding disorder [21]. VWF not only mediates the adhesion of platelets to subendothelial connective tissue, but also acts a carrier for blood clotting factor VIII that can be vanished from blood circulation in absence of VWF, due to protease. Factor VIII's absence is the reason for hemophilia [21], [24]. VWF is made by endothelial cells and the megakaryocytes, and is to be found in blood plasma, platelet α-granules, and subendothelial connective tissue. Purified VWF visualized by electron microscopy appears as filamentous structures of a diameter of 2-3 nm and a length of up to 1300 nm, close to the diameter of a platelet, or as loosely coiled molecules with an apparent diameter of 200-300 nm [31]. Atomic force microscopy has shown that the extended forms of are 'uncoiled' forms of the molecule that have acquired an starched chain shape in the direction flow under the effect of shear forces [32]. The natural building block of the VWF subunit as at least made of one dimer. The largest VWF multimers however are consisted of many dimers. The larger VWF multimers contain multiple sites of interaction with platelets and vessel wall components. Hence, they possess a higher thrombogenic potential. The degree of polymerization of mature VWF appears to vary with the anatomical location of the molecule. The largest multimers with the great thrombogenic potential are present in cellular storage, including endothelial cells and platelets, and not in blood plasma. However, understanding the role of different structural domains of VWF in adhesion is as vital as understanding the polymer's length and it shape conformation under shear force. Domain C1 is the site for the activated platelet integrin $b\beta3$, while the domain A3 is binding site for Collagen and the domain A1 is the proper binding site for platelet glycoprotein GPIb, and finally the blood clotting factor 8 can bind itself to domains D´and D3 [21].
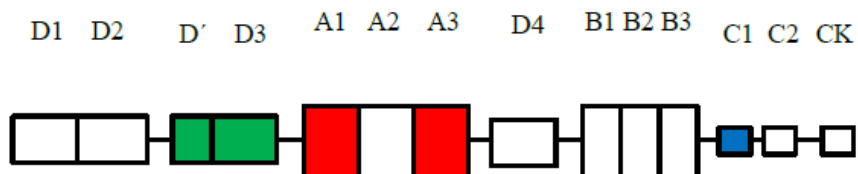

Fig. 1.7. Domains structure of von Willebrand Factor. [21]

VWF performs haemostatic functions through binding to factor VIII, to platelet surface glycoproteins or to parts of the connective tissue. Damage to endothelium allows VWF to bind to subendothelium connective tissue. VWF is also known to bind to several collagens in vitro, including types I, II, III, IV, V, VI [21-24].

Once the VWF is immobilized in subendothelial connective tissue platelets recognized and adhere to it. This requires *glycoprotein Ib-IX-V*, the only receptor on a non-activated platelet with significant affinity for VWF. VWF also binds to *Platelet Integrin* $\alpha_{IIb}\beta_3$ which is a member of cell-surface receptors. On a resting Platelet $\alpha_{IIb}\beta_3$ does not bind to VWF. However, by activation of platelet by thrombin or other agonists, it becomes able to bind to VWF [21], [24]. Von Willebrand Factor is one the largest soluble proteins known, assembled via covalent disulfide bonds from hundreds of monomeric units. The activity of VWF seems to be regulated by hydrodynamic shear. Over a threshold shear level the polymer transforms from a globular form to a stretched form [27], [28]. The allosteric transformation exposes the necessary structural domains for VWF-dependent platelet adhesion at higher shear rates. The size of the released von Willebrand Factor multimers is regulated by the metalloproteinase, *ADAMTS-13* [30]. The cleavage VWF multimers by ADAMTS-13 prevents abnormal aggregation and thrombus formation. Endothelial or plasma VWF multimers are cleaved by ADAMTS-13 in a time dependent process. In fact, ADAMTS-13 can effectively regulate the size and persistence in time of plasma VWF-mediated platelet aggregates [29],[30].

Blood platelets aggregation at the sites of vascular injury may cause thrombi formation. Thrombi formation contributes to arrest bleeding. However, thrombi may block the arteries causing cardiac diseases [33]. Thrombus formation occurs in successive stages. First, individual platelets adhere to injured vascular surfaces. Platelets get activated due to contact to the altered surfaces of vascular system. As a result, the *Integrin* $\alpha_{IIb}\beta_3$ on the platelet surface can bind plasma protein. The VWF, fibrinogen, and fibronectin bind to the $\alpha_{IIb}\beta_3$. This results to formation of an adhesive substrate for accumulation of more platelets. These result in thrombus growth and platelet aggregation. These events happen in under dynamic conditions, and are directly affected by fluid dynamics of the circulation system. At shear rates exceeding $1000s^{-1}$ in human circulation system initial platelet arrest depends on the glycoprotein $Ib\alpha$ ($GPIb\alpha$) binding to VWF. Rapidly forming VWF- GPIbα bonds can keep platelets on contact with a surface or other platelets for a limited time, until integrin receptors establish additional bonds. [24], [29], [31-33]

1.4.   Cancer Cell Adhesion and Extravasation

It has previously been shown that freely circulating melanoma cells can firmly bind to the extracellular matrix of the blood vessel possibly initiated by integrins [41]. There is increasing evidence that cancer cell spreading is accompanied by an activation of the coagulatory machinery [42]. Among different coagulation proteins von Willebrand factor (VWF) plays a key role in initiating the cellular hemostasis by binding platelets even under high shear flow conditions. Since in the first step circulating cancer cells have to adhere on blood vessels' wall in order to metastasize successfully later, studying the hematogenous tumor cell metastasis is a multifaceted process depending on numerous interactions happening in vascular system [43]. While, studying metastasis and hemostasis fails under static condition, designing in-vitro experimental set-ups for mimicking complex arising in-vivo fluid dynamics conditions is of extreme importance [43], [44].

2. Fluid Dynamics of Constriction in Different Reynolds Numbers

Constricted geometries are frequently found in vascular system. Complex hydrodynamic condition in constricted geometries makes them a special target for dynamic processes like hemostasis, inflammation …etc. Experimental and numerical investigation of fluid dynamic in a constricted geometry is vital for understanding the non-linear inertia effects at larger Reynolds numbers on the shear stress evolution in the fluid. This is of particular importance for blood flow since some biophysical processes in blood are sensitive to shear stress, for example VWF initiated thrombus formation, cancer cell adhesion, and leukocyte adhesion in inflammation [44-48]. It is also known that arterial plaque and stents favor the emergence of blood clots [24], [45], [49], [50], [53]. Besides such biochemical reasons, one possible physical cause for clotting may be the destructive influence of large local shear stresses in the vicinity of constrictions [24], [32], [33], [45]. Physically, the flow boundary conditions are modified by the presence of obstacles. Depending on the Reynolds number, obstacles can have a significant impact on the flow properties, even beyond the location of the obstacle. One of the simplest symmetric, yet non-trivial, flow geometry is a duct with a bottleneck-like constriction as sketched in Fig. 2.1. Using this obstacle, fundamental properties of the fluid flow at different Reynolds numbers between 0.1 and 100 is investigated in this work. Since one is interested in the basic physical effects of inertia in a constricted geometry, the problem can be simplified. In particular, the fluid is assumed to be steady, and a Newtonian fluid is used (water in the experiments) where the Reynolds number is the only relevant physical parameter. The assumption of a Newtonian fluid limits the validity of the experiments and simulations to larger blood vessels, since at those scales the individual motion of the red blood cells can be neglected and the viscosity is virtually independent of the shear rate [51]. However, this is no severe restriction since in this case one is mainly interested in the blood flow in human coronary arteries with average diameters of 3–4mm [52] which is 1000 times the radius of a red blood cell. Typical Reynolds numbers in coronary arteries are of order 100 [53].

2.1. Experimental Set-up

2.1.1. Experimental Study of the Hydrodynamics in Constriction

The employed geometry is a square duct (*width = height = H*) in the yz-plane. A 3D projection is shown in Fig.2.1. The flow enters at the inlet in x-direction. A constriction of total length $L_{con} = 5H/4$ is located halfway between the inlet and the outlet. In the constriction, the width of the duct (along the y-axis) is decreased, but the height (along the z-axis) remains constant. The constricted width is equal to *H/2*, leading to an average flux velocity two times larger than in the main duct. Due to the milling technique employed for the channel mold preparation the inner edges of the constriction are rounded with radius *r = H/4*. The origin of the coordinate system is always located at the center of the constriction. The experimental setup consists of the duct, cf. Fig. 1, a syringe pump and tubes for connecting the pump to the duct. The height of the duct is H = 2 mm. The flux is driven at a desired rate by application of the syringe pump (NE-1000, New Era Pump Systems, Inc., NY, USA). Connection between the pump and the duct succeeds over tubes connecting the syringe needle to the inlet. The duct itself consists of two parts. The upper part is made of polydimethylsiloxane (PDMS), casted into a mold produced by milling. This part is then converted to a completely closed duct by being attached to a microscope glass slide which plays the role of the lower deck of the duct. Inlet and outlet are punched into the duct before attachment of the PDMS to the glass slide. Attachment succeeds by plasma oxidation of the PDMS and the glass slide.
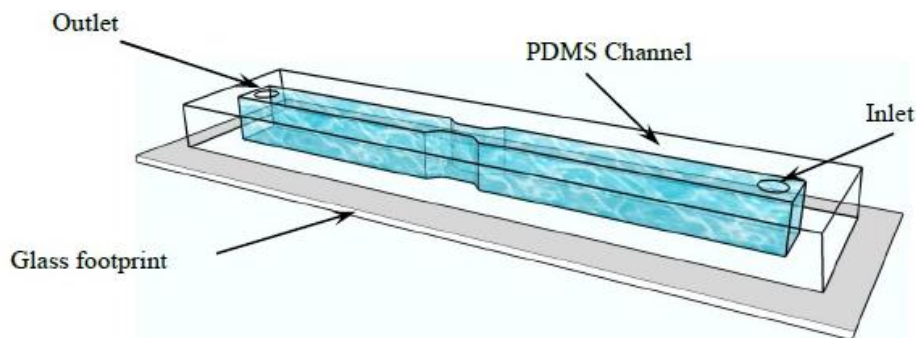

Fig.2.1. A schematic figure of the constricted pattern made of PDMS, and a glass footprint.

The local fluid velocity in the duct is measured by tracking polystyrene beads (Polysciences. Inc.,Warrington, PA, USA) with a diameter of 10 μm which are suspended in the carrier fluid ,water (density $\rho = 1000$ kgm^3 and viscosity $\eta = 10^3$ Pas at 20°C). The experiments are conducted on a Zeiss Axiovert 200 inverted microscope typically using a 2.5x objective. The velocities of the beads are observed at a height of 1mm over the footprint of the duct (i.e., in the middle between bottom and top). For each Reynolds number, a video of the flux inside the duct is made using an ultrafast camera (Fastcam, Photron, CA, USA). The video analysis for calculation of flow profile in the duct is done by the software 'Image J' afterwards.

2.1.2. Phase Contrast Microscopy*

Phase contrast microscopy is the method of choice for tracking the polystyrene beads in order to study the flow profile of the fluid in this work. Hence, describing the basics of the technique is rather necessary. This microscopy method was first described by Fritz Zernike in 1934 [54]. Phase contrast microscopy is a technique well suited to produce high contrast images of transparent specimens. This method employs an optical mechanism in order to translate minute variations in phase into respective changes in amplitude that can be visualized as differences in image contrast.

An incident wave front present in an illuminating beam of light is divided into two components, the *surround wave* (S) that passes through specimen, without interacting with them, and *diffracted spherical wave* (D) that gets scattered over a wide arc that passes through the full aperture of the objective. After leaving the specimen plane, surround and diffracted light waves enter the objective front lens element, and are subsequently focused at the intermediate image plane where they combine through interference and produce a resultant particle wave (P). The mathematical equation governing the relationship between the various light waves generated in phase contrast microscopy can be described as:

$$P = S + D \tag{2.1}$$

Detection of the specimen image depends on the relative differences, and therefore on the amplitudes of the particle, and surround waves are significantly different in the intermediate image plane. Hence, the specimen acquires a considerable amount of contrast and is easily visualized in the microscope eyepieces.

---

*Partly taken from Nikon Microscopy Basics and Tutorials

The portion of the incident that transverses the specimen (D-wave), but doesn't pass through the surrounding medium (S-wave) is slightly retarded. In Phase Contrast Microscopy the role of the specimen in altering the optical path length (here, the relative phase shift) is of high importance. In classical optics the optical path length (OPL) through an object or space is the product the refractive index (n) and the thickness (t) of the object or the intervening medium.

$$OPL = n \times t \tag{2.2}$$

As the light passes from one medium into another, the velocity is altered proportionally to the refractive index differences between the two media. Thus, when a coherent light wave emitted by the focused microscope filament passes through a phase specimen having a specific thickness (t) and refractive index (n), the wave is either increased or decreased in velocity. The resulting difference in location of an emergent wave front between the specimen and surrounding medium is called phase shift (φ) and defined in radians:

$$\varphi = 2\pi\Delta / \lambda \tag{2.3}$$

Where, the term Δ is the *optical path difference.*

$$\Delta = (n_2 - n_1) \times t \tag{2.4}$$

Where, n_2 is the refractive index of the specimen and n_2 is the refractive index of the surrounding medium.

The concept underlying the design of a phase contrast microscope is the segregation of surround and diffracted wave fronts emerging from a specimen, together with reducing the amplitude of the surround wave light and delaying or advancing it, in order to maximize the differences between the specimen and the background in the image plane. The mechanism for
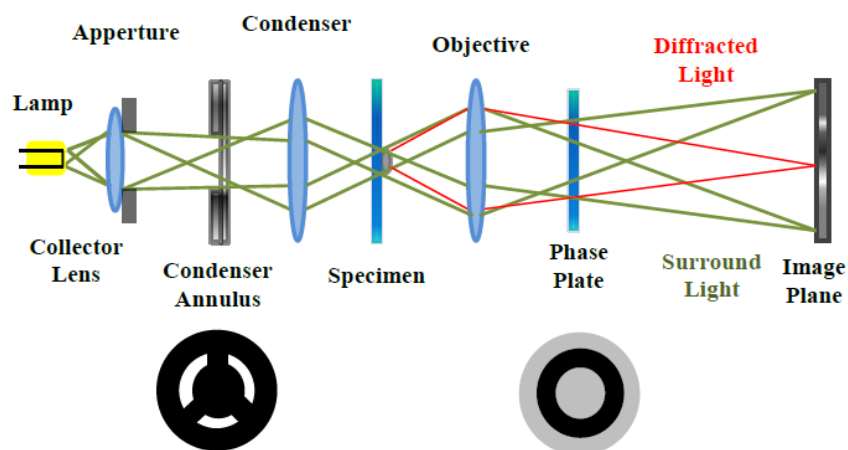

Fig.2.2. Phase Contrast Microscope Optical Train.

generating phase retardation is a two-step process. With the diffracted waves being retarded in phase by a quarter wavelengths at the specimen, while the surround waves are advanced or retarded in phase by a phase plate positioned in or very close to the objective rear focal plane. Using two specialized components one can convert a bright field microscope for phase contrast observation. A specially designed annular diaphragm, which is matched in diameter and optically conjugates to an internal phase residing in the objective rear focal plane, is placed in the condenser front focal plane.

The *condenser annulus* is typically constructed as a light absorbing plate with a transparent annular ring, which is positioned in the front focal plane of the condenser so the specimen can be illuminated by defocused, parallel light wave fronts emanating from the ring to infinity, as the objective produces an image at the rear focal plane. The circular geometry of phase contrast illumination and detections enables specimen observation without orientation-dependent artifacts.

Phase contrast microscopy is an excellent method for enhancing the contrast of thin transparent specimens without loss of resolution. This method also simplifies the investigation of the dynamic effects in specimen without artificial staining techniques when it comes to living cells.

2.2. Theoretical Study of Hydrodynamics of Flow in Constricted Patterns under Different Reynolds Number Values, Using Lattice-Boltzmann Method

2.2.1. The Lattice Boltzmann Method

Lattice Boltzmann is an established modeling method that can be considered as a new approach to modeling the flow of the multiphase fluid mixtures. Using Lattice Boltzmann method simple models of discrete particles confined to a lattice can be used to solve complicated flow problems. The Lattice Boltzmann method is based on the Boltzmann equation for the time rate of change of the particle distribution function in a particular state. It simply states that the rate of change is the number of particles scattered into a space minus the number scattered out of that space. The method is fully parallel and local. Parallel means that the same calculations are performed at every lattice site, local means that only neighboring particles at the lattice site interact with each other. It also yields a good approximation to the

standard equations of fluid flow, the Navier-Stokes equations, in the limit of long wavelengths and low frequencies. The lattice methods begin from a particle description of matter. A gas of particles exists on a set of discrete points that are spaced at regular intervals to form a lattice. Time is also divided discrete time steps, during which particles jump to next lattice site and then scatter according to kinetic rules that conserve mass, momentum, energy [55-58]. In contrast to the "top-down" and "bottom-up" approaches to modeling, the lattice methods begin from a particle description of a matter, while top-down approaches like Navier-Stokes equations for incompressible fluid flows start with a continuum description of macroscopic phenomena provided by partial differential equations. Numerical methods like finite-difference and finite-element methods are then used to transform the continuum description into a discrete one in order to solve the equations numerically on a computer. The "bottom-up" approach is based on the microscopic, particle description provided by equations of molecular dynamics; here the position and velocity of each atom or molecule in the system are closely followed by solving Newton's equations of motion.

In the lattice-Boltzmann method, space is divided into a regular lattice, and real numbers at each lattice site represent the single-particle distribution function at that site, that is equal to the expected number of identical particles in each of the available particle states i. In the simplest model, each particle state i is defined by a particle velocity, which is limited to a discrete set of allowed velocities. During each discrete time step of the simulation, particles move, or hop, to the nearest lattice site along their direction motion; where they collide with
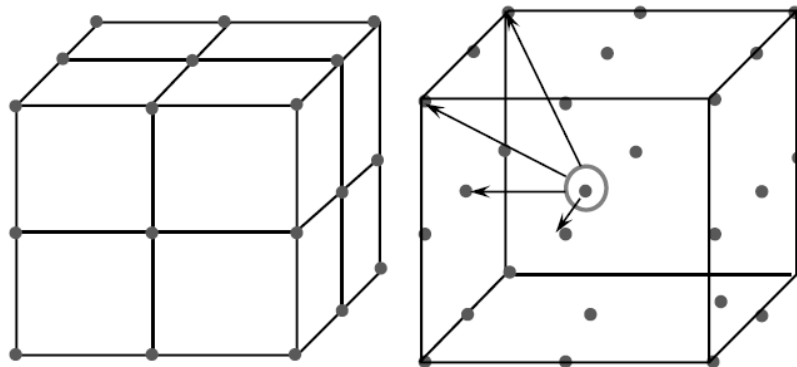
Fig.2.3. Allowed Velocities at a Lattice Site. The arrows show the magnitude and directions of the allowed velocities e_i at a lattice site in a three dimensional Lattice Boltzmann simulation. The sphere at the lattice site represents zero velocity, $e_0 = 0$. Lattice Boltzmann simulations are based on a proper equilibrium particle distribution and this minimum set of velocities preserved the desired isotropy of fluid properties. [32]

other arriving particles. The outcome of the collision is determined by solving the kinetic (Boltzmann) equation for the new particle-distribution-function at that site and the particle distribution function is updated. [32]

More specifically, the single-particle distribution function at a single site in a simple cubic lattice is represented by a set of real numbers, $f_i(\mathbf{x}, t)$, the expected number of particles at lattice site $\mathbf{x}$ and time t moving along the lattice vector $\boldsymbol{e}_i$, where each value of the index i specifies one of the allowed directions of motion. Figure.2.3. shows these directions. The ball in the center denotes the vector e_0 is equal to zero and represents particles that are not moving. [58]

There are two operations in each time step Δt of the calculation. The first is to advance the particles to the next lattice site along their directions of motion. Since speed equals the distance traveled divided by the time of travel (Δt), this model has just three speeds, zero for particles at rest, c for particles moving to the next sites along body diagonals, and $\sqrt{3}c$ for the particles moving to the next sites along the body diagonals.
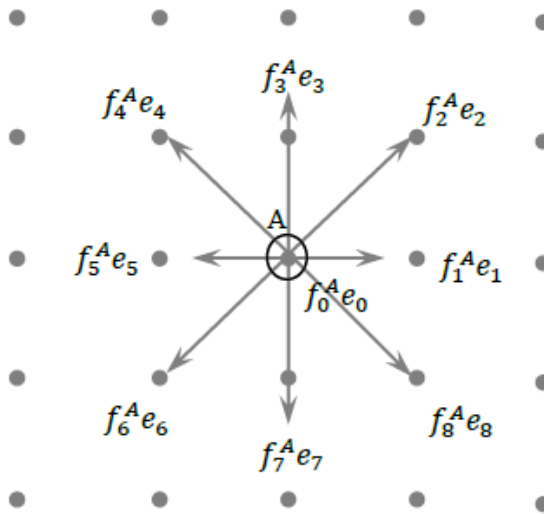
Fig.2.4. Momentum Distributions in Two Dimensions. The single-particle distribution function at each lattice site, $f_i(\mathbf{x}, t)$, equals the expected number of identical particles in each of the available particle state i. Particle velocities $\boldsymbol{e}_i$ are limited to a discrete set defined by the geometry of the lattice, and the momentum distribution at the lattice site is equal to $f_i(\mathbf{x}, t)\, \boldsymbol{e}_i$. On a two dimensional square lattice, eight directions of motion are available, so $i = 0,1,2,\dots,8$. [58]

Usually the units are chosen such that the distance to nearest neighbors and Δt are unity, so that $c = 1$ and the lattice vector $\boldsymbol{e}_i$ is numerically equal to the velocity of the particles moving in direction i. If one also sets the mass of each particle equal to unity, the momentum in direction i at site $\mathbf{x}$ and time t is just $f_i(\mathbf{x}, t)\,\boldsymbol{e}_i$ [32]. Figure 2.4 illustrates sample momentum distributions in two dimensions. The total momentum at lattice site A = $\sum_{i=1}^{8} f_i^A \boldsymbol{e}_i$.

The second operation is to simulate particle collisions, which cause the particles at each lattice site to scatter into different directions. The collision rules are chosen to leave the sum of the f_i's unchanged. In other words no particle is lost. The rules are also selected to conserve the total energy and momentum at each lattice site. To ensure that the particles have zero average velocity at boundaries, both perpendicular and parallel to walls, one normally imposes "bounce-back" boundary conditions, where any flux of the particles that hits a boundary simply reverses its velocity so that the average velocity at the boundary is automatically zero.

The outcome of the collisions is approximated by assuming that the momenta of the interacting particles will be redistributed at some constant rate toward equilibrium distributionf_i^{eq}. This simplification is called the single-time-relaxation approximation. The net momentum of the incoming state is zero. Indeed, if no external forces exist, the equilibrium distribution consists simply of equal amounts of momentum in each of the allowed directions of motion. External forces like gravity and electromagnetic forces can be added to the model and make the f_i's grow in the direction of the net force and shrink in the opposite direction [58]. Although lattice models consist of a very simple set of rules, those rules may lead to very complicated flow patterns discussed in details elsewhere [55-60].

2.2.2. Theoretical Investigation of the Constricted Channel

Due to the non-linear character of the Navier-Stokes equations, at large Reynolds numbers, abrupt changes in cross-section may lead to spatial variations of velocity and shear stress which cannot be fully understood from dimensional considerations or the Stokes equations. For this reason, we study the impact of a bottleneck-like constriction on the local properties of the fluid as a function of the Reynolds number. We are particularly interested in the spatial asymmetry and the magnitude of the shear stress. In order to emphasize the nonlinear effects arising at high Reynolds numbers, we vary the Reynolds number over three order of magnitude, $(0.1 - 100)$, thus covering both the fully viscous and inertial regimes. At large

Reynolds numbers, the spatial flow velocity and shear stress fields are asymmetric, even in a symmetric geometry. The cause is the convective term in the Navier-Stokes equations. This asymmetry introduces a distinction of the pre- and post-constriction regions. Moreover, one can observe that the peak values of the shear stress close to the constriction increase faster than linearly with the Reynolds number, showing the significance of the inertia effects. [60]

Fig.2.5. A 2D projection of the constriction geometry used both in the experiments and simulations. The fluid enters the geometry from the left. Numerically, the inlet and outlet velocities $\mathbf{u}_a(y, z)$ are taken from the analytic solution of the steady duct flow problem. The origin of the coordinate system is at the center of the constriction. The initial width (along y-axis) and height (along z-axis) are H, and the constricted width is $H = 2mm$. The total length of the constriction is $L_{con} = 5H/4$, and the initial inclination of the constriction walls is $45°$. The rounded corners with radius $r = H/4$ are due to the milling technique used for fabricating the duct. The numerical values of the inlet and outlet duct lengths L_{in} and L_{out} are chosen in such a way that the flow can fully develop.

The theoretical study of the fluid dynamics of succeeds by understanding the theoretical fluid dynamics with the boundary conditions sketched in Fig.2.5. The detailed information on the theoretical fluid dynamics and the calculations can be found in Appendix.1. In order to capture the physical boundary conditions of both the constriction-fluid surface (no slip) and the inlet and outlet cross-sections of the simulation box (fully developed flow), we employ the standard LBM bounce-back boundary condition. At the inlet and outlet of the computational box, a fully developed velocity profile $\mathbf{u}_a(y,z)$ is imposed. The velocity boundary condition used has been proposed by Latt et al. [59]. We compute the pressure p, velocity vector u, and the full shear stress tensor in the entire numerical grid. From this data, we can calculate the

effects of inertia on the spatial velocity and shear stress distributions. We trace the maximum values of velocity and shear stress.

2.3. Results

Fig.2.6. Locations of the velocity measurements in the experiments (black dots). All positions and distances are given in units of mm. The origin is located at the center of the constriction. The flow enters from the left. The velocities have been measured at three positions along the x-axis (x = -1.85 mm, 0.05 mm, and 1.85 mm) and five positions along the y-axis (y = 0 to 0.8mm in steps of 0.2 mm). In the constriction, only three data points have been taken (y = 0, 0.2 mm, and 0.4 mm). In order to compute the velocities, the times of travel of the tracer particles between the dotted lines have been measured (Δx = 0.8mm and Δy = 0, respectively).

Table.2.1. Measured and simulated velocities in the constriction at selected positions (x, y) midway between the bottom and top walls, cf. Fig. 2.6. All velocities are given in units of mms^{-1}. The deviations are also shown.

position		Re = 0.1			Re = 1			Re = 10			Re = 100		
x[mm]	y[mm]	exp	sim	dev	exp	sim	dev	exp	sim	dev	exp	sim	dev
−1.85	0.0	0.092	0.109	16%	1.2	1.08	11%	9.8	10.6	8%	87	106	18%
−1.85	0.2	0.088	0.104	15%	1.1	1.03	7%	9.4	10.2	8%	85	101	16%
−1.85	0.4	0.076	0.0894	15%	0.98	0.891	10%	8.9	8.85	1%	76	88.7	14%
−1.85	0.6	0.054	0.0669	19%	0.81	0.669	21%	6.0	6.69	10%	63	67.1	6%
−1.85	0.8	0.038	0.0370	3%	0.50	0.371	35%	4.1	3.70	11%	43	35.8	20%
0.05	0.0	0.17	0.199	15%	1.9	1.99	5%	27	19.4	39%	151	161	6%
0.05	0.2	0.14	0.165	15%	1.5	1.65	9%	25	16.1	55%	144	150	4%
0.05	0.4	0.049	0.0662	26%	0.93	0.662	40%	9.2	6.55	40%	103	71.1	45%
1.85	0.0	0.085	0.109	22%	1.0	1.10	9%	14	12.8	9%	144	155	7%
1.85	0.2	0.072	0.104	31%	0.92	1.05	12%	10	11.9	16%	140	140	0%
1.85	0.4	0.071	0.0894	21%	0.42	0.897	53%	6.2	9.58	35%	103	95.2	8%
1.85	0.6	0.065	0.0669	3%	0.33	0.669	51%	5.8	6.57	12%	32	42.8	25%
1.85	0.8	0.045	0.0370	22%	0.22	0.369	40%	4.8	3.35	43%	21	8.46	148%

Fig. 2 demonstrates the locations of the velocity measurements in the experiments. The velocities have been estimated by measuring the time of travel of representative tracer particle

between two positions along the x-axis ($\Delta x = 0.8$mm and $\Delta y = 0$). The resultant velocity is assumed to be the velocity midway between the two points. The experimental data is shown together with the corresponding velocities from the simulations and the relative deviations in Table.2.1.

Although, the experiments have been carried out with great care, as can be seen in Tab. 2.1, the quantitative comparison of the experimental and simulation velocity data reveals some deviations. The major reason is that the velocities cannot be measured locally in the experiments. Instead, the motion of the tracer beads is followed over a finite distance of *0.4H (0.8 mm)*, and the velocity at the middle of this line is assumed to be the average velocity, cf. Fig. 2.6. This approach can only be accurate if the length over which the particles are
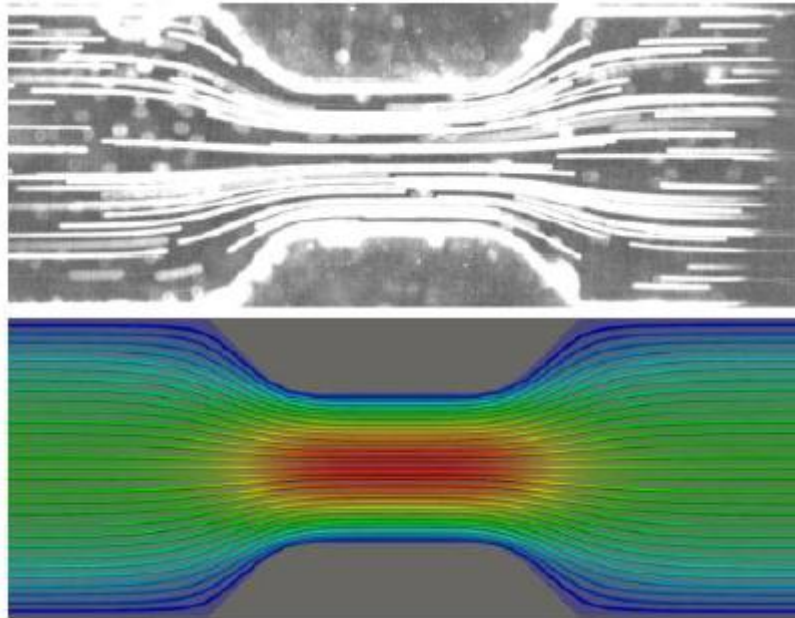
Fig.2.7. The streamlines at Re = 1 and seen in the experiments (top) and in the simulations (bottom) at z = 0 (midway between bottom and top walls), respectively. The fluid enters from the left. The colors in the simulation figures correspond to the velocity magnitudes. [60]

observed is small compared to the typical length for the change of the velocity field. This characteristic length is of order *H/4* which is half the width of the duct inside the constriction. Consequently, there is an intrinsic uncertainty in the velocity measurement. The particles do not always move on straight lines which can be recognized from the shape of the streamlines (Fig. 2.7). This makes it hard to achieve a good estimate for the local velocities even when the time resolution of the measurements is high. Especially close to the walls (*y = 0.8mm* before

and after the constriction, and *y = 0.4mm* inside the constriction), the deviations are expected to be larger. The reason is that the velocity gradient is maximal in the vicinity of the walls. If the position of the tracer beads is slightly shifted along the y-axis, this will lead to a large uncertainty in the velocity measurement.
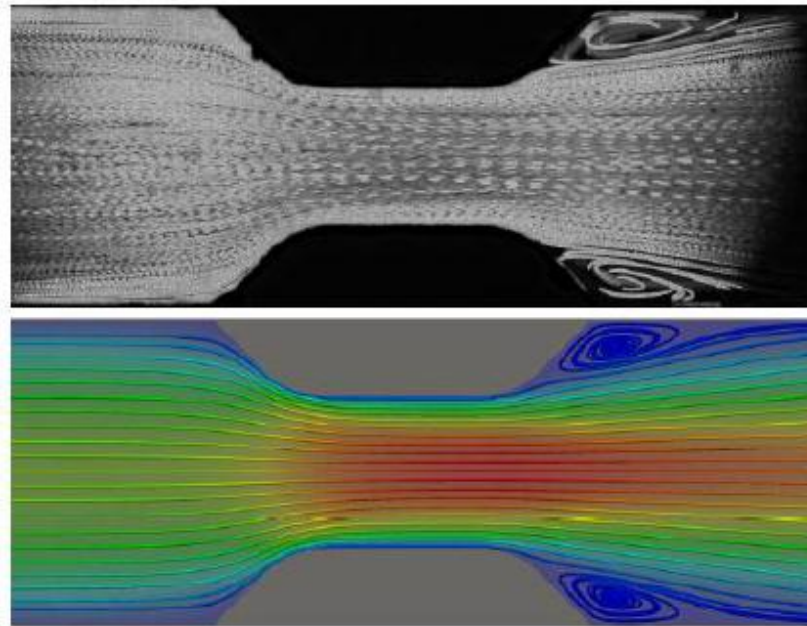

Fig.2.8. The streamlines at Re = 100 and seen in the experiments (top) and in the simulations (bottom) at z = 0 (midway between bottom and top walls), respectively. The fluid enters from the left. The colors in the simulation figures correspond to the velocity magnitudes. [60]

However, as clearly shown in Fig. 2.7 and Fig.2.8 it is encouraging to see that the qualitative shape of the experimental streamlines are excellently recovered by the computer simulations, especially the shape of the vo8rtices at Re = 100. Taking those considerations into account, the agreement between experiments and simulations is satisfactory.

In order to estimate the impact of inertia on the shear stress in coronary arteries, we have employed the lattice Boltzmann method together with experimental methods to simulate the flow in a constricted geometry with Reynolds numbers between 0.1 and 100. We assumed the fluid to be Newtonian since the particulate nature of blood and its non-Newtonian properties are only significant in small blood vessels like venules and arterioles.

It is noteworthy to mention that shear rate or shear stress tensor is a full 3×3 tensor, but in the literature, shear rates are usually reported as scalars, the expected one for the simple shear flow [60]. For this reason, we have to compute a representative scalar from the tensor. The common approach is to compute the von Mises stress (magnitude) of the tensor, as defined in Eq.2.5. This choice ensures that the effective shear rate extracted from the tensor is exactly the expected one for simple shear flow. The effective shear rate is the shear stress divided by the dynamic viscosity.

$$\sigma_{eq} = \sqrt{\frac{1}{2}\sum_{\alpha\beta}\sigma_{\alpha\beta}\sigma_{\alpha\beta}} \tag{2.5}$$

The major observation is that the peak value of the effective von Mises stress σ_{vM} (the scalar equivalent stress that can computed from stress tensor) grows disproportionally fast with the Reynolds number in the inertial regime [Appendix.1]. At Re = 100, a common value of the Reynolds number in coronary arteries, the peak value of σ_{vM} is about 70% larger than expected from assuming the validity of the Stokes flow. This observation indicates that a combination of pathological blood vessel geometries and large Reynolds numbers may increase the risk of blood clotting in presence of coagulation factors specially VWF due to its shear dependent shape conformation as described in chapter 1. This is a pure hydrodynamic effect.

We further observe that the influence of the constriction is noticeable only inside and behind itself, and in the upstream of the constriction; the flow field and the shear stress are not significantly influenced. In particular, the inertial effects break the symmetry of the flow field upstream and downstream of the constriction.

3. Thrombocytes Adhesion in Stenotic Geometries

3.1. Introduction to Microcirculatory Condition of Small Vessels

Experiments in glass capillary tubes with diameters less than 300μm show that blood rheology is influenced by the two phase nature of the blood. In flowing blood, there is a narrow region near the tube wall that is free of red blood cells. The red blood cell free region is a result of cell exclusion near the surface. In large tubes/vessels, the red cell free region is a small fraction of the tube's cross section on which the hematocrit is approximately uniformly distributed. But, as the tube size decreases, the cell free region becomes a larger fraction of the cross sectional area. *Fahreus-Lindquist effect* explains the phenomenon in which the apparent viscosity of blood decreases in tubes with diameters between 30μm and 300μm. For tube diameters less than 10μm, the tube hematocrit and the blood viscosity in tube increase with decreasing tube diameter, since the tube radius approaches the size of a red blood cell. [1]

The *Fahraeus-Lindqvist effect* indicates that the flow resistance in arterioles and capillaries should be less than which is predicted by bulk viscosity of blood. However, measurements of the resistance to flow in capillaries indicate that the flow resistance is greater than believed [61]. In this case the change in resistance can not be explained just on the basis of hematocrit. The shape and inner topography of the arterioles and capillaries due to presence of endothelial surface layer, that is consisted of a layer of glycoproteins and glycolipids, and the complex interaction of red blood cells and white blood cells cause an increase in flow resistance and add to the complexity of fluid dynamic in small vessels.[1], [61]

The blood flow in complex small vessels and its effect on thrombotic activities has also been studied in details elsewhere before [61-64]. Our approach to study the thrombotic behavior in complex narrow constricted geometries is *in vivo* investigation of specific adhesion of separated thrombocytes on matrix and coagulation proteins under complex flow conditions, by mimicking the stenotic flow conditions.

3.2. Experimental Set-up to Mimic Microcirculatory Conditions

3.2.1. Stenotic Micro-Channel

The employed geometry is a rectangular duct with a width of $\approx 500\mu m$ and height of $\approx 40\mu m$. A 2D and 3D projection is shown in Fig.3.1. The flow enters at the inlet in x-direction. The constriction is located closer to outlet between inlet and outlet. In the constriction, the width of the duct (along the y-axis) is decreased to $\approx 60\mu m$, whereas the height (along the z-axis) is constant. The duct itself consists of two parts. The upper part is made of polydimethylsiloxane (PDMS). It is prepared by molding the PDMS on a micro-structured silicon wafer, on which the structural geometry of the channel's micro-structure is deposited on the silicon substrate. Microstructure deposition on the silicon wafer succeeds by standard photolithographic methods using SU8 photoresist (MicroChem, MA, USA). The detailed photolithography process is described in details elsewhere [61], [62]. After pouring the PDMS into the produced mold, the PDMS is heat treated in order to accelerate the polymer crosslinking process. Finally, the upper part of the channel made of PDMS is separated from the substrate and attached to a microscope glass slide by plasma oxidation. The microscope glass slide plays the role of the channel's footprint.
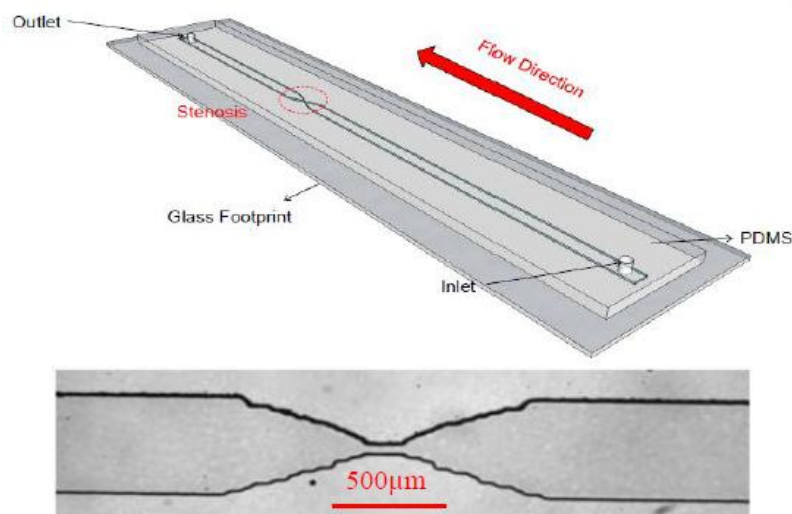

Fig.3.1. Above: The schematic sketch of the duct with a stenotic geometry. Below: A top view image of the produced channel captured with the 2.5X objective.

The experimental set-up consists of the above mentioned microchannel, a syringe pump, syringe, and tubes to connect to the channel to a syringe at inlet, and to waste chamber at outlet. The flux is driven at a desired rate by application of a syringe pump (NE-1000, New Era Pump Systems, Inc., NY, USA). Study of the platelet adhesion to the biofunctionalized channel succeeds by application a of Zeiss Axio Observer Z.1 (Carl Zeiss AG, Oberkochen, Germany) capable of performing Phase Contrast-, Fluorescence-, and Reflection Interference Contrast- Microscopy.

3.2.2. Fluorescence Microscopy

Materials can absorb, reflect, and radiate energy in form of light. When a material reradiates light after former light absorption, the process is typically of fluorescence or phosphorescence nature. Fluorescence emission is nearly simultaneous with the absorption of the excitation light with a time delay between photon absorption and emission that is typically less than a microsecond. Stokes used the term *fluorescence* for the first time in the middle of the 19th century as he observed that the mineral fluorspar emitted red light when it was illuminated by ultraviolet (UV) excitation. Fluorescence microscopy is an essential tool in biology as well as in materials science as it has characteristics that are not readily available in other optical microscopy techniques. Even if one does not consider the specimens that auto-fluoresce, an array of fluorochromes utilize the identification of cells, submicroscopic cellular components and entities with a high degree of specificity. The fluorescence microscope makes detection of a single fluorescing molecule possible. In a sample with more than one component identification of several target molecules is possible by application of multiple staining. Although the fluorescence microscope cannot provide spatial resolution below the diffraction limit of the respective objects, the detection of fluorescing molecules below such limits is possible. [65], [66]

For fluorescence microscopy the specimen is irradiated with the desired wavelength and the much weaker emitted (fluorescent) light is separated from the excitation light. Only the emission light should reach the eye or a detector so that the resulting fluorescing areas are contrasted against a dark background. The detection is only possible by the darkness of the background. The exciting light is typically 10^5 or 10^6 times brighter than the emitted light. [66]

Among the different fluorescence microscopy optic arrangements the *Epi-fluorescence microscope* is the overwhelming choice of users. Thus, we discuss this optical alignment in

more details here. This is basically a reflected light microscopy mode in which the wavelength of the reflected light is longer than that of the excitation. J.S. Ploem is credited with the development of the vertical illuminator for reflected light fluorescence microscopy. In this device, light of a specific wavelength or set of wavelengths, often in the UV wavelength, is produced by passing light from a lamp through a wavelength filter. The desired wavelength light reflects off a dichromatic (dichroic) mirror, through the microscope objective lens to the specimen. If the specimen fluoresces, the collected emission light then passes through the dichromatic mirror and is subsequently filtered by a barrier filter that blocks the excitation wavelengths. It should be noted that this is the only mode of microscopy in which the specimen, subsequent to excitation, gives off its own light [66].
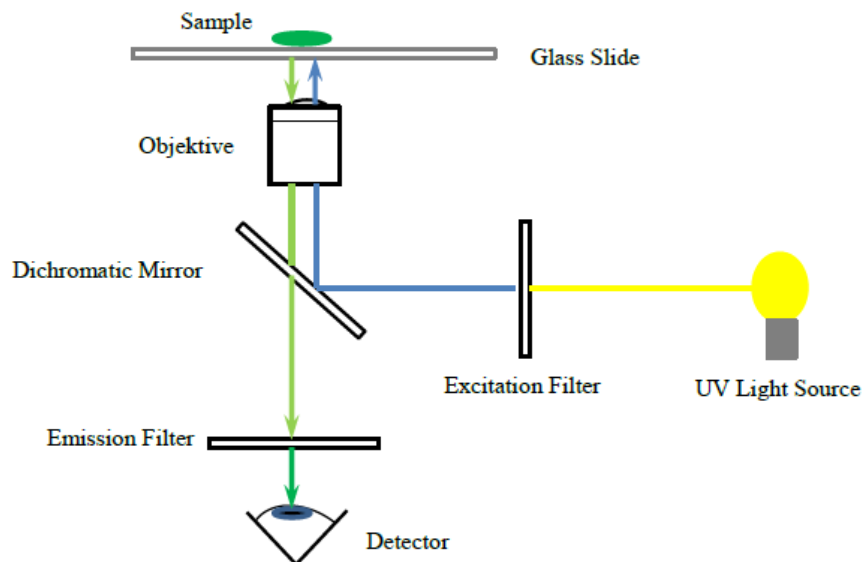
Fig.3.2. A schematic sketch of the optical alignment of an inverted Epi – Fluorescence microscope.

As sketched in Fig.3.2 the illuminator in Epi-Fluorescence is designed to direct light onto the specimen by first passing the light through the microscope objective on its way toward the specimen and then using that same objective to capture the emitted light. There are some advantages for this alignment. Among those is that the objective is serving as a well-corrected condenser as well as the image capturing light gatherer, and it always stays in the correct alignment. Beside those, most of the unused excitation light passes through specimen and travels away from the objective; the illuminated area is restricted to that which is observed. The last but not least is the possibility of combination or alternation of the reflected fluorescence light with transmitted light. The light source is usually a mercury or xenon

lamp. The light travels along the illuminator perpendicular to the optical axis of the microscope, and passes through collector lenses and aperture diaphragm, and then through a variable, centerable field. It impinges upon the excitation filter where selection of the excitation wavelength and blockage of undesired wavelengths occurs. The selected wavelengths reach the dichromatic beam splitting mirror. This special type of interference filter efficiently reflects shorter wavelengths of light and passes longer wavelengths. The dichromatic beam splitter is tilted at 45° to the incoming excitation light and reflects the excitation light at a 90° angle directly through the objective and onto the specimen. The fluorescent light emitted by the specimen is gathered by the objective. Since, the emitted light consists of longer wavelengths; it passes through the dichroic mirror. Before the emitted light can reach the eyepiece or detector, it passes through a suppression filter that blocks any residual excitation light and passes the desired longer emission wavelengths. In most reflected light fluorescence illuminators, the excitation filter, dichroic mirror, and barrier filter are incorporated in a cube. [66], [67]

3.2.3. Reflection Interference Contrast Microscopy

Reflection Interference Contrast Microscopy (RICM) is the term for a microscopy method employing the interference pattern of polarized incoming light, being reflected at an object, in order to reconstruct the height profile the object at an interface. The RICM is a powerful technique to study the interaction of cells with surface [81], [82]. Considering a cell in contact with a transparent substrate e.g. glass, the light reflected from the cell surface (object beam I'') and the light reflected from the glass surface (reference beam I') are brought to interference.
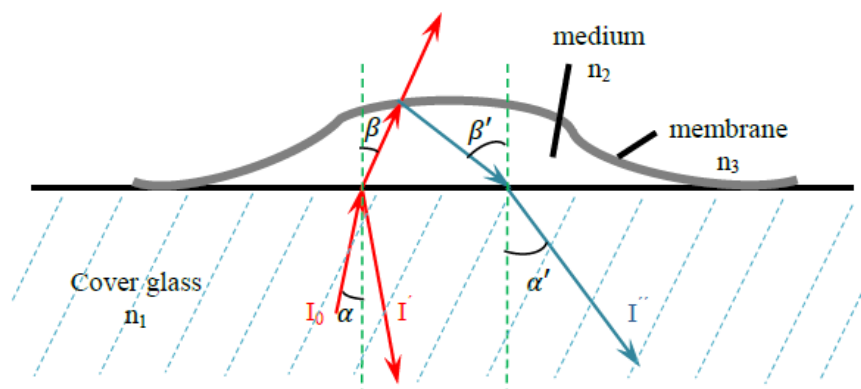

Fig.3.3. Schematic representation of reflection interference contrast microscopy of a cell. [83]

As sketched in Fig.3.3 the emitted light I_0 is partly reflected, transmitted at each interface, and refracts by during its pathway from one medium to another. The interference of the object beam and the reference beams results in an image with information on the height profile of the sample. However, the main technical problem is to separate RIC pattern from the very strong background caused by the reflection in the incident light at the objective and the stray light. For a normal incident light ($\alpha = 0$) the intensities of the object and the reference beams are: [83]

$$I' = I_0\,(1\text{-}R_1) \quad and \quad I'' = I_0\,(1\text{-}R_1)R_2 \tag{3.1}$$

Where

$$R_1 = ((n_1 - n_2)^2 / (n_1 + n_2)^2)^2 \quad and \quad R_2 = ((n_2 - n_3)^2 / (n_2 + n_3)^2)^2$$

are the reflectivities of the glass and the cell surfaces. The problem of very weak intensity of object beam in respect to reference beam is overcome by the Antiflex technique, in which the incident light is passes a polarizer, where it becomes linearly polarized. Then, a $\lambda/4$ plate in the objective change the light polarization from linear to circular. As a result of different interferences within the specimen the polarization direction if inverted, and while passing the $\lambda/4$ plate again, the polarization shifts back to linear. Consequently, a reflected beam of perpendicular polarization to incident beam goes through a second polarization filter that ensures the detection of light with correct polarization direction. [84] Hence, the stray light which has not passed the $\lambda/4$ plate will be filtered out.

3.3. Adhesion of Thrombocytes on Wild Type von Willebrand Factor under Stenotic Conditions

Studying the thrombotic behavior of blood platelets fails under static conditions. We have already discussed the complex flow patterns that arise in constricted vessels of bigger dimensions in chapter 2. Investigation of thrombotic activities in vessels of lower dimensions like arterioles and capillaries is also a very important and challenging task, duo to the complicated nature of mimicking the fluid dynamic condition of small vessels *in vivo* systems, and the complexity of blood streaming at these dimensions due to the *Fahraeus-Lindqvist effect*. Although, there have been many detailed studies on platelet adhesion under

hydrodynamic condition [7-40] conducted in whole blood streaming, duo to the advantage of similarities to physiological conditions; studying the specific interaction of thrombocytes with coagulation protein VWF and matrix proteins can be simplified by separation of blood platelets from the whole blood and re-suspension in blood plasma enables us conducting experiments under relevant hydrodynamic conditions, without making any vital compromise in the qualitative aspect of the measurements. Subsequently, the natural complexities of whole blood's fluid dynamic as explained in section 3.1 would be reduced, due to absence of erythrocytes.

Hence, we have isolated the thrombocytes from the whole blood, and have re-suspended them in the blood plasma. The product of the process is *Platelet Rich Plasma* (PRP). The PRP is a Newtonian fluid with a viscosity close to the value of the water. The concentration of blood platelets can be adjusted according to the experimental requirements. In this work unless stated otherwise, we have chosen a concentration of 200000 platelets per microliter of plasma, laying in physiologically valid values [1], [6].

In order to study the effect of hydrodynamics on the specific adhesion of platelets to the coagulation protein VWF, and the matrix protein collagen, we have infused the prepared PRP solution with the desired infusion rate through the stenotic duct. The duct geometry and hydrodynamic condition of the stenotic geometries can be reproduced in this manner. However, before infusion the channel should be biofunctionalized with the aforementioned proteins. Effective biofunctionalization methods are already well established [67].

3.3.1. Channel Biofunctionalization

The channels are coated with three different proteins. The first is the plasmatic von Willebrand Factor with a concentration of 500µg/ml (supplied by department of Haematology, Imperial College London, UK), the second one is Collagen Type I C7661 (Sigma Aldrich, Missouri, USA), and the third one is Bovine Serum Albumin (BSA) (Serva GmbH, Heidelberg, Germany). Collagen Type I and BSA can be considered respectively as control and negative control coatings for VWF.

Biofunctionalization of the channels with VWF succeeds by filling the channel with the VWF solution with the concentration of 500µg/ml and incubation of the channel for three hours at 37°C in a moisture rich environment, for example cell culture incubator. Since the channel's body is made of PDMS, and due to the ability of PDMS to absorb water and moisture, it is recommended that that the channels are kept in a moisture rich chamber 24 hours before

injection of the protein-solution. This may reduce the absorption of the protein-solution water adsorption by the channel, which may lead to dehydration of the protein during the biofunctionalization. A successful biofunctionalization of the channel with collagen succeeds by following the same protocol with a change of incubation time to a mimimum of one hour. The same process is applied for biofunctionalization of the channel with BSA, but the incubation times can be reduced to maximum of one hour.
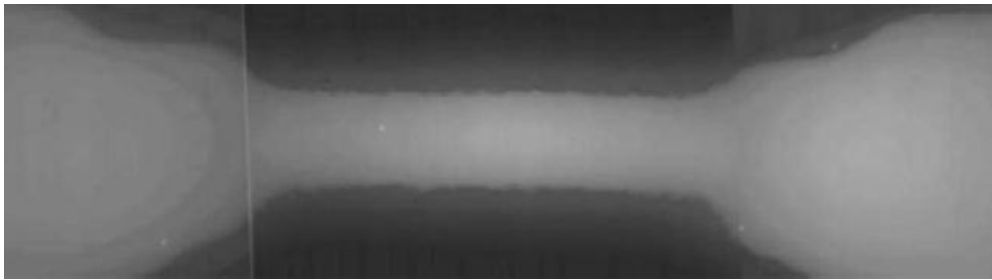
Fig.3.4. Stenotical channel biofunctionalized with fluorochrome (Alexa Fluor Protein Labeling Kit). The homogenous coating is captured by 5X objective of using a FITC filter.

Since VWF, collagen type I, and BSA in their nature are not observable under transmission or phase contrast microscopy; one has to employ staining techniques to check the quality and homogeneity of the biofunctionalization process. Another way is using fluorochromes for labeling the protein with a fluorescence dye and observing the dye distribution with a fluorescence microscope. We have employed the latter technique for visualization of the VWF coat on the channel substrate (Fig.3.4.). The VWF is labeled with Alexa Fluor Protein Labeling Kit 488 (Invitrogen), and then the channel is coated with the fluorescence labeled protein. The coating coherence can be visualized using a fluorescence microscope with a FITC filter.

3.3.2. An Insight into Fluid Dynamics of Experiments

By having the channels properly coated with the aforementioned protein, and calculation of the wall shear rate out of *Poiseuille's Law* (Eq.1.39) at the stenotic constriction in the channel, one can start infusing the PRP and subsequently observe and measure the adhesion of platelets on the glass footprint of the channel. However, visualization of the streaming lines in

the channel at different shear rates would be necessary for a better realization of the hydrodynamic conditions. Hence, the local fluid velocity in the middle of the duct's height (h=20µm) is measured by tracking polystyrene beads (Polysciences, Inc. Warrington, PA, USA) with a diameter of 10 µm which are suspended in water as the carrier fluid. The streaming lines for different shear rates are then visualized by overlapping the captured sequences using *Image J* program.
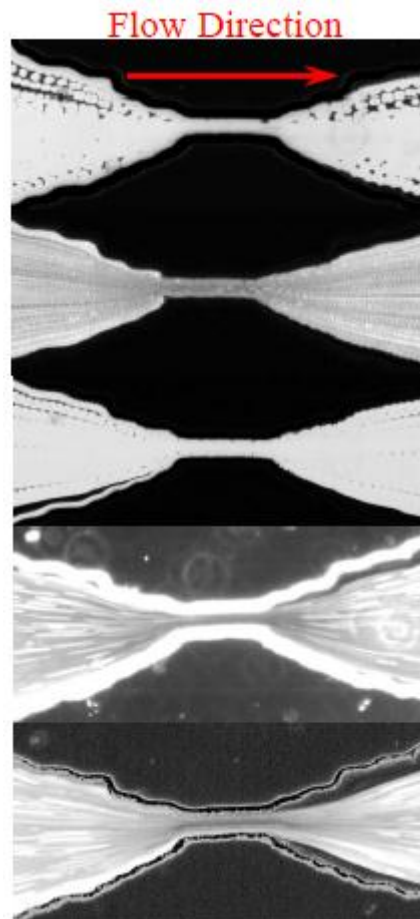
Fig.3.5. Flow streaming lines at the middle of the channel for wall shear rates 1000s^{-1}, 5000s^{-1}, 10000s-1, 20000s-1, and 40000s-1 inside the stenosis, respectively from above to bottom, captured with a 2.5X objective. Note the asymmetry at higher flow rates [60].

By infusion of PRP into channels biofuctionalized with the aforementioned proteins, one can investigate the specific interaction of thrombocytes with that specific immobilized protein. The infusion sequence that chosen after an explicit test phase is to start with the lowest stenotic wall shear rate (1000s^{-1}) and shifting up to the next higher shear rate. Measurements

are conducted for about 4 minutes at each shear rate, and experiments with stenotic wall shear rates of 1000 s^{-1}, 5000 s^{-1}, 10000 s^{-1}, 20000 s^{-1} and finally 40000 s^{-1} are conducted one after another. This shall provide us with data on the adhesive behavior of thrombocytes on each coating under a stepwise rise of shear rate.

$0.02\dot{\gamma} \qquad 0.03\,\dot{\gamma} \qquad 0.05\dot{\gamma} \qquad 0.16\dot{\gamma} \qquad 0.55\dot{\gamma} \qquad \dot{\gamma}$

$0.019\dot{\gamma}\,[s^{-1}]$	$0.385\dot{\gamma}\,[s^{-1}]$	$0.107\dot{\gamma}\,[s^{-1}]$	$0.355\dot{\gamma}\,[s^{-1}]$	$\dot{\gamma}\,[s^{-1}]$	
20 s^{-1}	38 s^{-1}	106 s^{-1}	350 s^{-1}	1000 s^{-1}	1
100 s^{-1}	192 s^{-1}	530 s^{-1}	1750 s^{-1}	5000 s^{-1}	2
225 s^{-1}	385 s^{-1}	1060 s^{-1}	3500 s^{-1}	10000 s^{-1}	3
450 s^{-1}	770 s^{-1}	2120 s^{-1}	7000 s^{-1}	20000 s^{-1}	4
900 s^{-1}	1540 s^{-1}	4240 s^{-1}	14000 s^{-1}	40000 s^{-1}	5
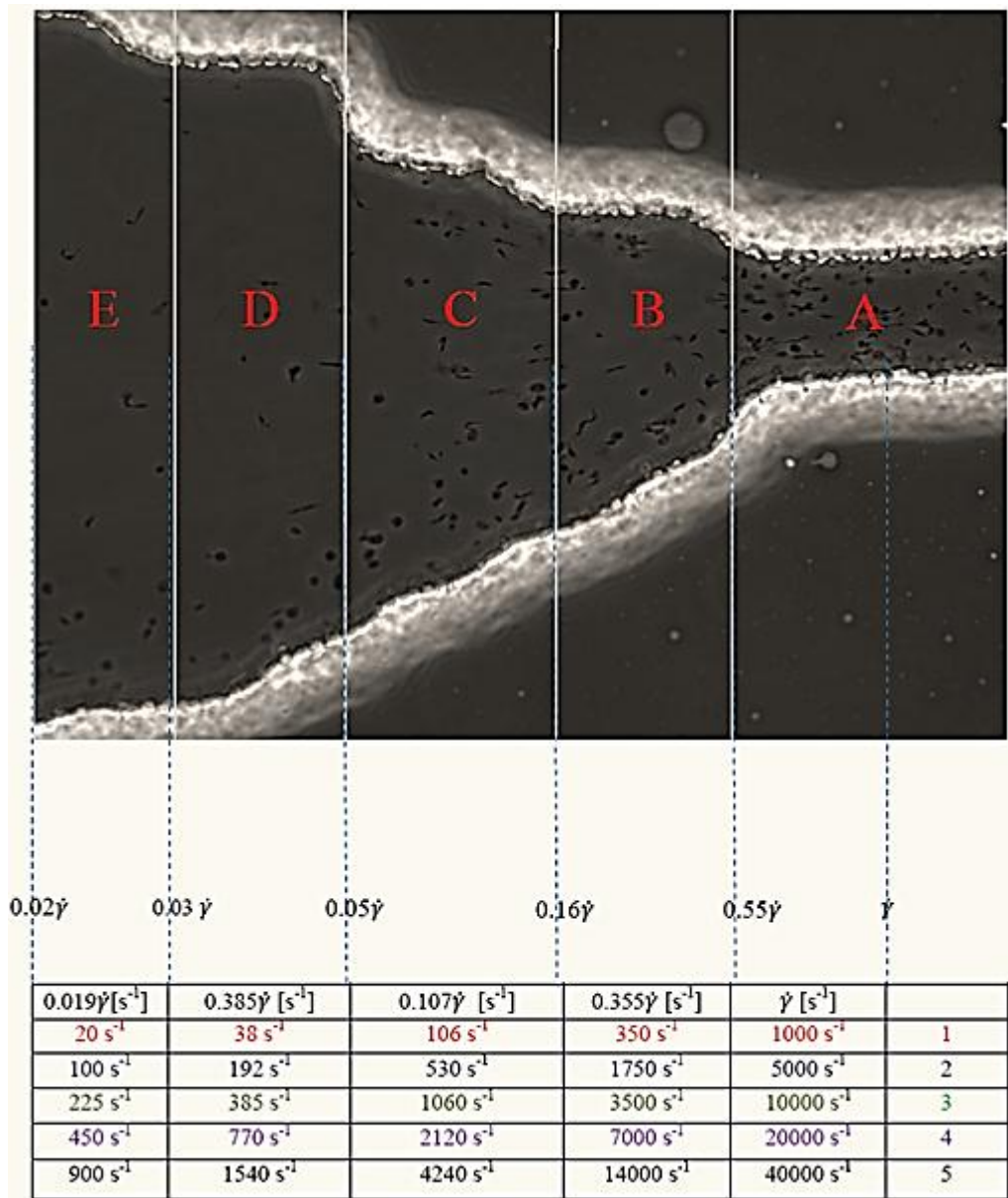
Fig.3.6. Depicts the stenosis and entry region before the stenosis. By setting the shear rate at the stenosis section (A), simultaneously subsequent shear rates arose in the other channel sections (B-E), and the resulting adhesion processes can be studied parallel to the stenosis.

As depicted in Fig.3.6. and the embedded table, another advantage of using a channel structure as the one used in this work is the possibility of studying the adhesion processes in different shear rates simultaneously, as they arise in different sections of the (A-E) channel, just by setting the desired hydrodynamics factor at one the regions, for example in section A

(Stenosis) in this work. As a result by studying the aforementioned 5 shear rates in stenotic section of the channel (1000 s^{-1}, 5000 s^{-1}, 10000 s^{-1}, 20000 s^{-1}, 40000 s^{-1}) one can calculate a wide range of shear rates in such an *in vivo* system, as shown in Fig.3.6. Hence, the adhesion of the thrombocytes on the plasmatic VWF has been investigated under the above mentioned conditions in a wide range of wall shear rates. The micro-channels with stenotic constrictions prove to be of high value for investigation of adhesion processes, as one would see in the results section 3.5.

3.4. Adhesion of Thrombocytes on Deglycosylated von Willebrand Factor in Stenosis

Surface of many cells contain short polysaccharide chains. These polysaccharides are linked to the cell surface by the reaction of an OH or an NH2 group of a protein with anomeric carbon of a cyclic sugar. Proteins bonded to polysaccharides are called *glycoproteins*. The percentage of carbohydrate is variable between 1% up to 80% of the proteins mass. Many different types of proteins are glycoproteins. For instance, structural proteins such as collagen, proteins like immunoglobulines, follicle stimulating hormone, and thyroid stimulating hormone are glycoproteins. Blood plasma proteins are also glycoproteins, among those the VWF [70]. The structures of these oligosaccharide chains on VWF are very diverse, although, their functional role remains unclear.

Oligosaccharide side chains make up approximately 20% of the mass of VWF [70]. One of the major determinants of plasma VWF antigen (VWF:Ag) levels is the ABO blood group of an individual, and it has been shown that ABH antigens are present within the oligosaccharide component of VWF [70]. VWF contains 12 N-linked and 10 O- linked oligosaccharide chains to specific residues of the mature VWF peptide [70-72]. At present, the structures of most of the N-linked oligosaccharides are known [70-72]. These contains blood group A, B, and H
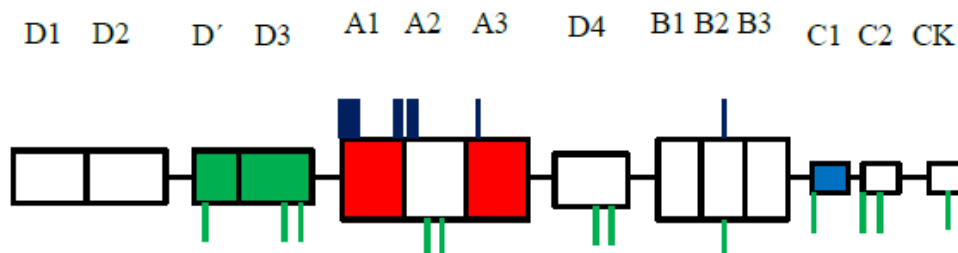

Fig. 3.7. Positions of the N- and O-linked oligosaccharide side chains on the VWF molecule. Green bars represent the N-linked side chains, and dark blue bars represent the O-linked side chains. [71]

antigenic structures; blood group antigens have not been demonstrated on O-linked. The distribution of N- and O- linked oligosaccharide side chains is sketched in Fig. 3.7.

By treating a glycoprotein with PNGase F (Peptide-N-glycosidase F) enzyme, the N-linked oligosaccharides can be detached from the main chain of the polymer. PNGase F is one of the most widely used enzymes for the deglycosylation of glycoproteins. Providing the necessary time and proper environment necessary for the enzyme activity, treatment can succeed without the pre-denaturation before treatment. The enzyme releases asparagine-linked oligosaccharides from glycoproteins and glycopeptides by hydrolyzing the amide of the asparagine (Asn) side chain. [49-55]

We have treated the plasmatic VWF with PNGaseF (Supplied by department of Hematology, Imperial College London, UK) in order to remove the N-glycans. The deglycosylated VWF have been labeled with *Alexa Fluor 488 Protein Labeling Kit* and has been employed for biofunctionalization of stenotic microchannels under the same condition explained before for the adhesion of thrombocytes on plasmatic VWF. Producing such a mutant and studying the role of degylcosylation on the specific interaction of thrombocytes with VWF is a fundamental question to answer.

3.5. Results
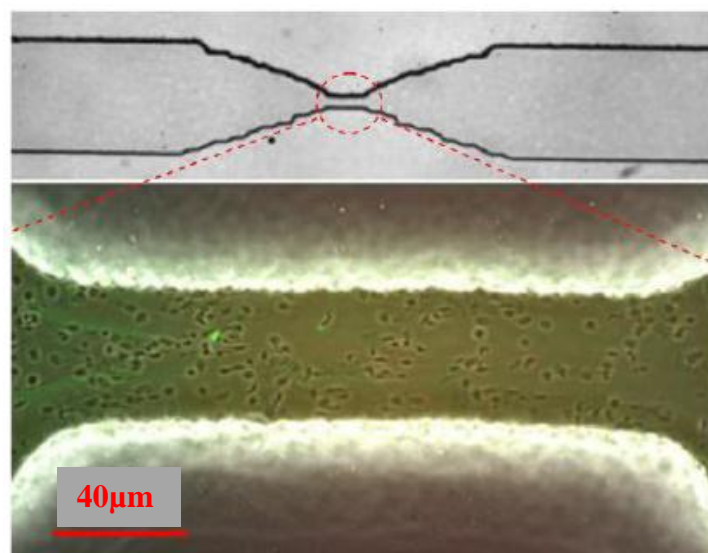
Fig. 3.8. Thrombocytes adhered to the VWF coating of the channel at $1000s^{-1}$ inside the stenosis. Multidimensional image is result of overlapping a FITC image and a phase contrast image using the 63X objective

It is expected that studying the specific adhesion of thrombocytes on plasmatic VWF under the fluid dynamics of constricted channels in PRP confirms the shear stress dependency of adhesion and thrombus formation seen before under the condition of non-Newtonian fluid. An interesting phenomenon observed while conducting experiments is that the interaction of blood platelets start from shear rates lower than $1000s^{-1}$ and increases with the rise of wall rate shear. The interaction is a combination of rolling, reversible adhesion, and irreversible adhesion of thrombocytes on the coated channel footprint. The reversible adhesion, and the rolling may lead to irreversible adhesion and spreading, as observed in other works conducted in whole blood environment [8-10], [13], [14]. However, the interaction of platelet with the biofunctionalized surface before occurrence of the irreversible adhesion looks like "dance steps" as demonstrated in Fig. 3.9.
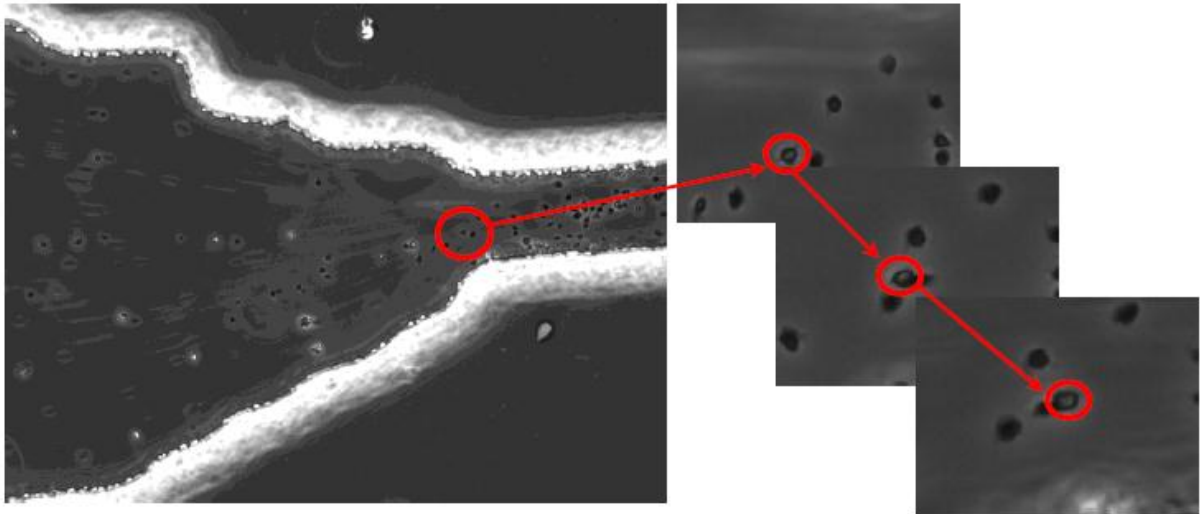
Fig. 3.9. The reversibly adhered platelets move with the direction of flow while interacting with VWF coat. The way that thrombocytes interact with VWF before formation of an irreversible bond to the VWF coat looks like "dance steps" as schematically demonstrated in this image cascade.

Fig.3.10 shows the quantitative adhesive behavior of the thrombocytes on the immobilized plasmatic VWF on the duct's footprint under different shear rates. The adhesion rate of the thrombocytes is positive with the rise of the wall shear rate up to the $5000s^{-1}$. The adhesion rate is continuously positive till $20000s^{-1}$ but with a lower slope. Over this shear rate value the adhesion rate goes negative, indicating that a number of already adhered platelets leave the adhesion site, without replacement happening.
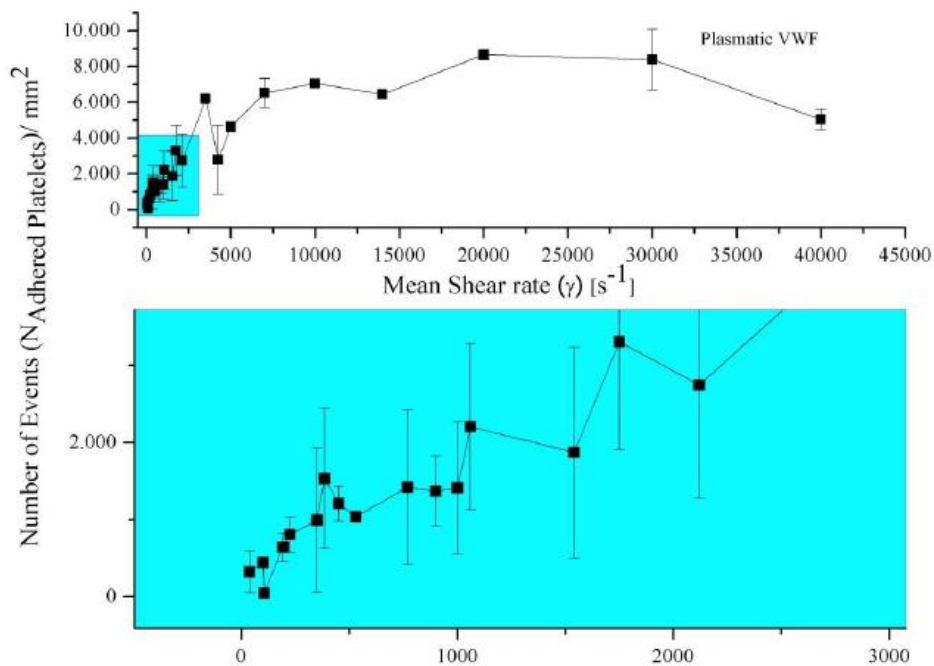
Fig.3.10. Adhesion of thrombocytes (per unit of the area) on the footprint of a channel biofunctionalized with plasmatic VWF.

As discussed before, the adhesion of in PRP suspended platelets on the VWF is matter of active interactions, including rolling, flipping, reversible, and finally irreversible adhesion. Live videos of experiments suggest that the portion of the fluctuations in adhesive behavior (rolling, flipping, and reversible adhesion) decreases with increase of shear rate, favoring the irreversible adhesion of platelets at higher shear rates. In order to verify the validity of this observation one has to perform a statistical investigation to find out the ratio of the number of adhered thrombocytes in short time intervals in respect to the mean number of adhered thrombocytes over the whole experimental period, for different shear rates.

As Fig.3.11 depicts, the variation in net number of adhered platelets in short time intervals   at higher shear rate shows more variations, that is typical of statistical phenomena with higher number occurring events. However, the ratio (relative adhesion fluctuations) of the fluctuations in short time intervals in comparison to mean number of events decreases at higher shear rates. This suggests that at higher shear rates the number of irreversibly adhered platelets increases in comparison to the number of all platelets in interaction with the biofunctionalized channel footprint. A very interesting but yet plausible effect that agrees with the shear depend shape conformation of VWF. This indicates that at higher shear rates (e.g. $20000s^{-1}$) due to full conformation of VWF's shape from globular to stretched, and development of VWF bundles and networks, the
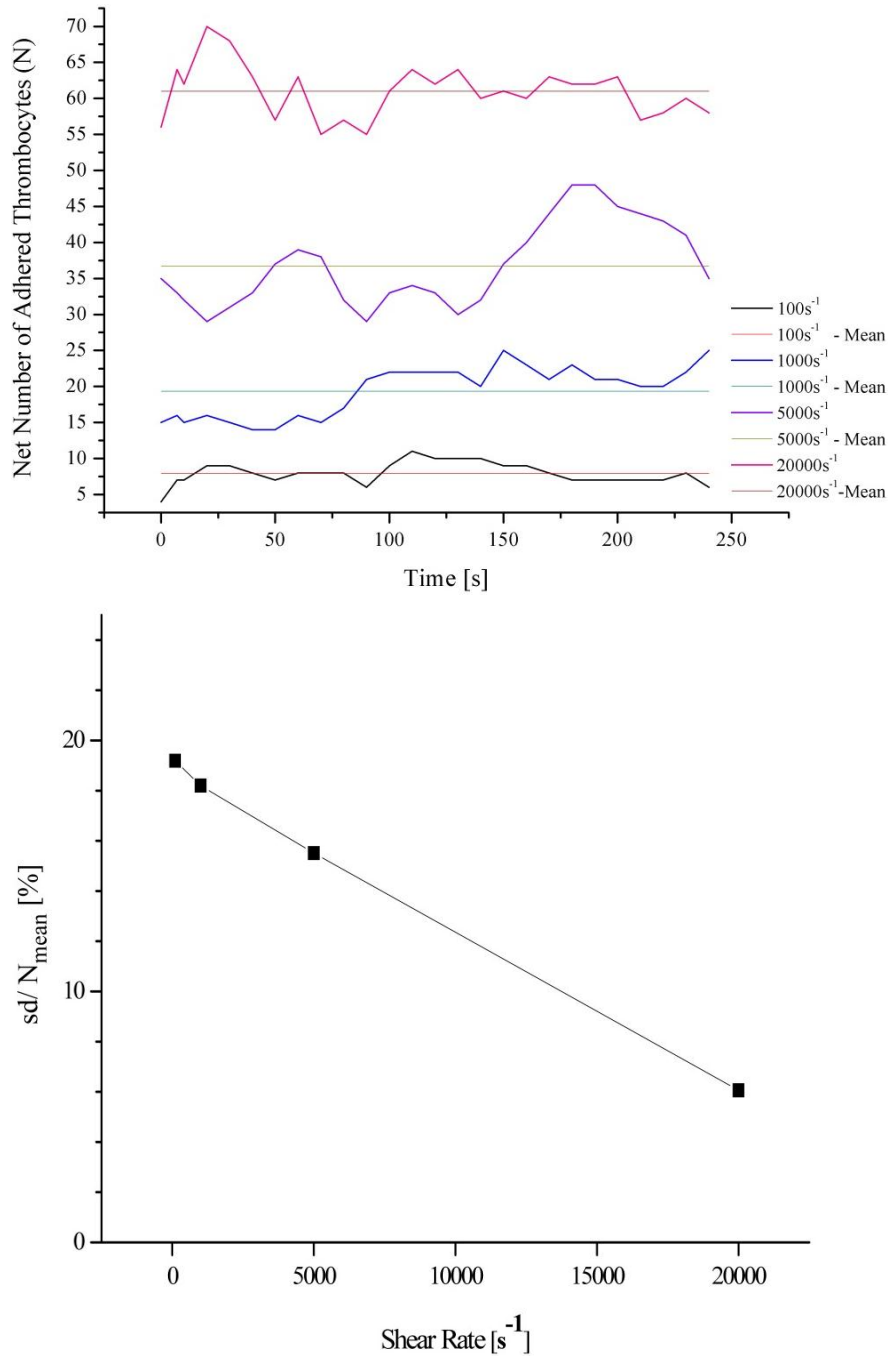
Fig.3.11. Above: The net number of adhered thrombocytes in short time intervals of 10s in a 4 minute long experiment, in comparison to the mean number of adhered thrombocytes over the whole 4 minutes of experimental time, for shear rates of $100s^{-1}$, $1000s^{-1}$, $5000s^{-1}$, and $20000s^{-1}$. Bottom: The ratio (relative adhesion fluctuations) of standard deviations of the adhered platelets in short time intervals of 10s to the mean number of adhered platelets over an experimental time of 4 minutes long. It shows a sharp reduction of the reversible adhesion (relative fluctuation) with increase of the wall shear rate.

necessary protein domains are completely exposed for platelet arrest. Hence, at higher shear rates it is mainly the VWF that regulates the platelet adhesion.

Studying the effect of VWF deglycosylation on the ability of the glycoprotein to arrest platelets and initiate thrombosis is of high importance due to the high oligosaccharides content of the VWF and the complicated role of oligosaccharides in biochemistry of VWF. The experimental methodology is remains exactly the same as for the plasmatic VWF and all the factors have been preserved in order to maintain the comparability between the adhesive behavior of the platelets on both the plasmatic VWF and its deglycosylated mutant.
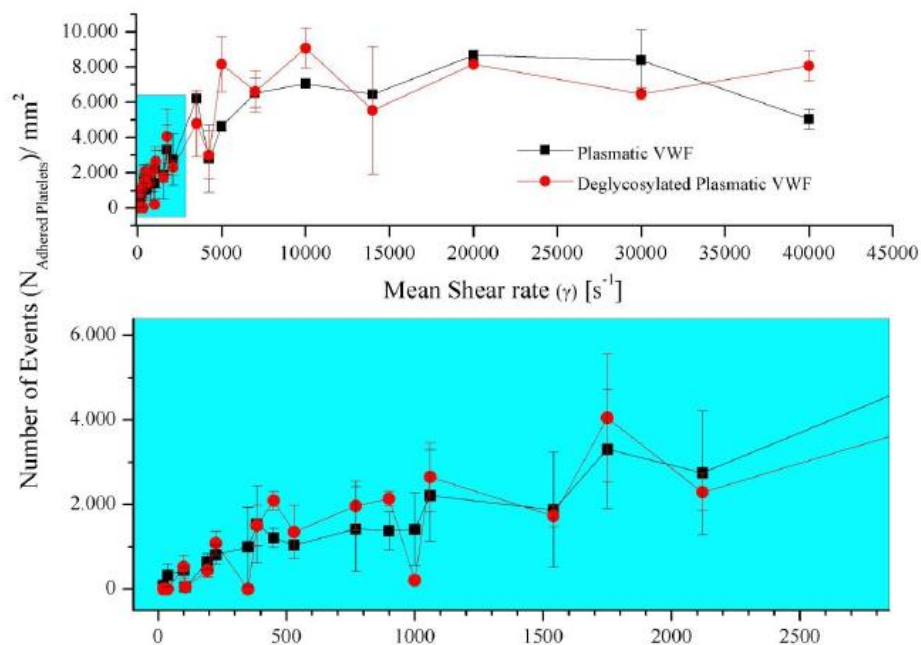
Fig.3.12. Adhesion of thrombocytes on unit of the area of the footprint of a channel biofunctionalized with deglycosylated VWF versus the adhesion of platelets on the footprint of channel coated with plasmatic VWF.

Counter-intuitively but interestingly as shown in Fig. 3.12 one finds out that except for a few measurement points, the adhesion of platelets on the deglycosylated VWF is quantitatively identical to the adhesion of platelets on the plasmatic VWF. Hence, removal of N-linked oligosaccharide side chains does not change the basic functionality of VWF for arresting blood platelets. Hence, deglycosylation may have slightly affected the structural response of the VWF at certain levels of hydrodynamic forces, but it does not disable the protein from doing its main function in thrombosis initiation.

The adhesion of blood platelets on the matrix protein collagen Type I has been found to be of extremely low magnitude, so that one can report the specific interaction of platelets and immobilized collagen to be close to zero, and it applies for all the shear rates studied, during the 4 minute long experimental time. The same phenomenon applies for the adhesive behavior of thrombocytes towards the BSA coated channel.

4. Rolling Aggregates

The VWF is essential for normal platelet adhesion and aggregation in vessels in which rapid blood flow results in elevated shear stress. In some segments of the vascular system e.g. small arterioles and arterial capillaries the wall shear rate estimates to be of the order of 1700 s^{-1} [32]. However, in diseased arteries in which obstructive processes, such as plaques, reduce the lumen diameter, shear rate can increase up to excess of 5000 s^{-1}, like the case of coronary arteries with a 50% stenotic occlusion [85]. Hence, the influence of shear-dependent phenomena may be even greater in such conditions than in the case of normal hemostasis. The VWF is essential to initiate platelet adhesion and thrombus formation at sites of vascular injury due to its ability to link components of the extracellular matrix with GpIbα on platelet membrane through bonds that form rapidly and, at least transiently, resist high tensile stress. Hence, the specific role of VWF in formation of platelet aggregates have to be studied thoroughly [24]. Progress in understanding the structure and function of VWF and the mechanisms that underlie its interactions with platelets has led to important insight into the differentiation between normal hemostasis and pathological arterial thrombosis. The conventional view of signaling-induced platelet aggregation had been extended to include activation-independent aggregation [29]. Pathological arterial blood flow generates fluid shear stresses that directly cause platelets to aggregate. At shear rates lower or equal to 1000 s^{-1}, initial adhesion to a reactive substance and subsequent aggregation follow the generally accepted pattern of progressive accumulation of single platelets. Nevertheless, at higher shear rates, activation independent platelet adhesion mediated by VWF facilitates adhesion and proceeds stable aggregation. Thus, one can conclude that VWF, in addition to being essential for the initial adhesion, is also crucial for transiently linking platelets to one another until platelet activation stabilizes the linkage [45].

Platelets interact with surfaces that present immobilized VWF, initiating a prompt response in which two receptors, GpIbα and the integrin $\alpha_{IIb}\beta_3$ are known to be required for formation of stable platelet-surface and platelet-platelet contacts [24]. Since, the platelet interaction with immobilized VWF is studied thoroughly in chapter 3; this chapter is concentrated on the subject of platelet-platelet interactions in presence of VWF. In spite of that, it is noteworthy to remember that platelet thrombus formation is thought to occur in successive stages [29]. First, individual platelets adhere to altered vascular surfaces and are activated. Afterward, the integrin $\alpha_{IIb}\beta_3$ can bind plasma proteins, notably fibrinogen, VWF and fibronectin. This

prepares an adhesive substrate immobilized on the membrane surface recruiting additional platelets, resulting in aggregation and thrombus growth [24], [33]. In detail, the initial binding of GpIbα to the A1 domain of the VWF causes platelet tethering to the vessel wall. Progressive tethering and recruitment of further platelets leads to formation of aggregates, anchored to the vessel wall. Cleavage of the anchored aggregates leads to the platelet aggregates roll on vessel wall and translocate in the flow direction, a phenomenon studied in the following section.

4.1. Rolling Thrombocytes Aggregates Formation

4.1.1. Experimental Set-up

Studying the formation of rolling aggregates succeeds by mimicking the whole blood flow condition employing "BioFlux 200" experimental set-up (South San Francisco, California, USA), together with a Zeiss Axio Observer Z.1 microscope (Carl Zeiss AG, Oberkochen, Germany) capable of performing phase contrast-, fluorescence-, and reflection interference contrast- microscopy. Especially for experiments conducted in whole blood RICM method is beneficial. The BioFlux system is a bench top instrument which allows up to 24 hour temperature-controlled flow cell assays in parallel. The BioFlux pressure interface connects a highly precise and accurate electro pneumatic pump to the well plates to initiate controlled
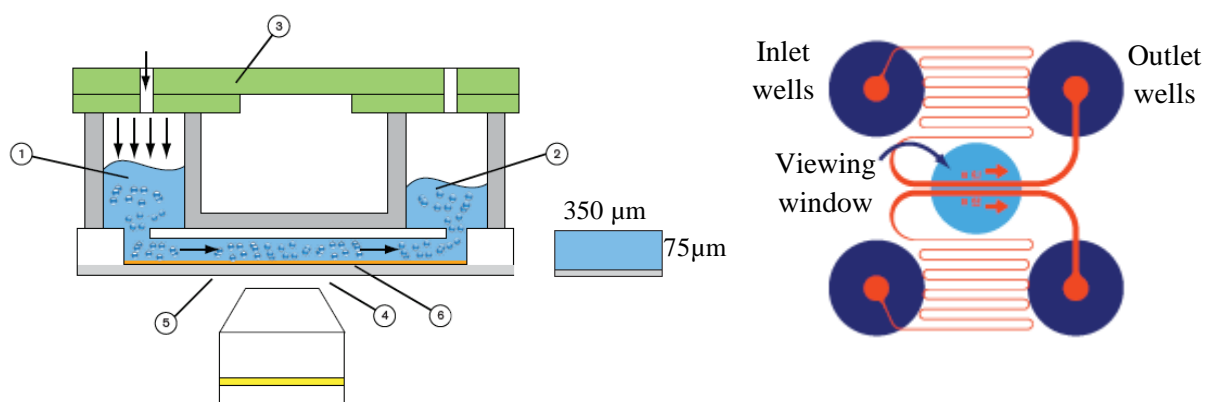
Fig.4.1. Left: The schematic sketch of Bioflux set-up, 1) and the 2) respectively correspond to the input well and output well; 3) is the pressure interface of the instrument, the 4) represents the microscope objective; 5) and 6) are respectively the glass footprint of the system, and the cell layer or the channel coating. Right: The well-channel geometry, and the viewing window of the BioFlux system.

shear flow. The System works with the existing inverted microscope and is compatible with fluorescence, bright field, phase and confocal imaging.

4.1.2. Methods and Preparation

For these experiments the channel is biofunctionalized two consecutive times with recombinant VWF with a concentration of $\approx 50\mu g/ml$, according to the protocol explained in section 3.3.1. The whole blood is centrifuged in order to separate the blood plasma from the whole blood. In fact, the *platelet free plasma* is isolated from the whole blood and the other blood components remain intact. It is important to mention that the platelets remain present in whole blood. Then, the plasma is replaced with fluorescent labeled recombinant VWF (Baxter, Vienna, Austria) in PBS solution in order to bring the concentration of VWF in whole blood to $50\mu g/ml$. This not only facilitates a relatively exact regulation of the VWF content of whole blood, but also facilitates the visualization of the circulating VWF interactions with the immobilized VWF channel coating and the platelets.

Experiments are conducted by infusion of the whole blood containing the labeled recombinant VWF, into the channel biofunctionalized with recombinant VWF, at different flow velocities and resulting wall shear rates. It is important to mention that by feeding the BioFlux set-up with information on the type of circulating medium and the desirable wall shear rate, the set-up calculates and sets the proper corresponding flow velocity automatically. Platelet adhesion and aggregation under wall shear rates of 1000 s^{-1}, 1500 s^{-1}, 2000 s^{-1}, 2500 s^{-1}, and 5000 s^{-1} have been qualitatively investigated in BioFlux system.

4.2. Rolling Beads Aggregates Formation

Investigation of platelet adhesion and aggregation has been done thoroughly before and the interactions of VWF and blood platelets have been studied in many earlier works. The interaction processes have been described for normal and arterial hemostasis [13], [14], [16], [18], [20], [24], [29], [33], [36]. However, the complexity of the biological factors involved in the thrombotic processes and the complex fluid dynamics conditions arising in the

microcirculatory system call for a more specific study of single components of thrombotic elements. In order to concentrate more on the specific physical role of VWF in platelet aggregation a simplified physical model of blood platelets should replace the thrombocytes. In fact, the blood platelets have to be replaced with particles of the same size and physical shape. This provides us with information on VWF interactions with entities of the same size of thrombocytes under the physiologically relevant flow conditions. However, since the two receptors, GpIbα and the integrin $\alpha_{IIb}\beta_3$ on the platelet surface are known to interact with VWF and initiate stable platelet-VWF and platelet-platelet adhesion; replacing the blood platelets with spheres of the thrombocytes size alone would not provide us with a relevant comparison. Thus, the spheres have to be passively functionalized in order to interact with the VWF. Interactions of such "sticky beads" with the VWF may clarify the specific role of VWF in hemostasis even further.

4.2.1. Methods and Preparation

The experimental set-up in this section remains identical to that of section 4.1.1. However, the preparation method for these experiments goes under a few important changes. As before, for these experiments the channel is biofunctionalized two consecutive times with recombinant VWF with a concentration of $\approx 50\mu g/ml$, according to the protocol explained in section 3.3.1. The whole blood is centrifuged in order to separate the *platelet rich plasma* (PRP). It is important to mention that unlike section 4.1.2 at this stage platelets together with plasma are separated from the whole blood. An effective separation of the platelets is absolutely vital, since presence of platelets and their VWF binding sites may interfere with the interactions VWF and the spheres which have to replace the platelets in whole blood. Other blood components remain intact. As before the plasma is also replaced with fluorescent labeled recombinant VWF (Baxter, Vienna, Austria) in PBS solution in order to bring the VWF concentration in whole blood to 50µg/ml.

The blood platelets are replaced with biofunctionalized borosilicate glass spheres (Duke Scientific, Palo Alto, CA) with a diameter of 2 µm. The beads are biofunctionalized by linkage of Polyclonal Rabbit Anti-Human von Willebrand Factor (DakoCytomation, Denmark). The Antibody linkage to glass beads succeeds by a multistep process that succeeds by linkage of the VWF antibody to the base treated microspheres via mal-PEG-NHS ($\alpha -$

Maleinimido − ω − carboxy succinimidyl ester polyethylene glycol, Iris Biotech GmbH, Germany). This complex PEGlycation process has been developed by Evan Evans group and is explained thoroughly elsewhere [86-89].

The experiments are conducted under identical condition to section 4.1.2.

4.3. Results

The investigation of thrombocyte adhesion and aggregation reveals that at a wall shear rate of 1000 s^{-1} progressive adhesion and rolling of single platelets on the footprint of the biofunctionalized channel take place. This is in agreement with works published before [29], [33].
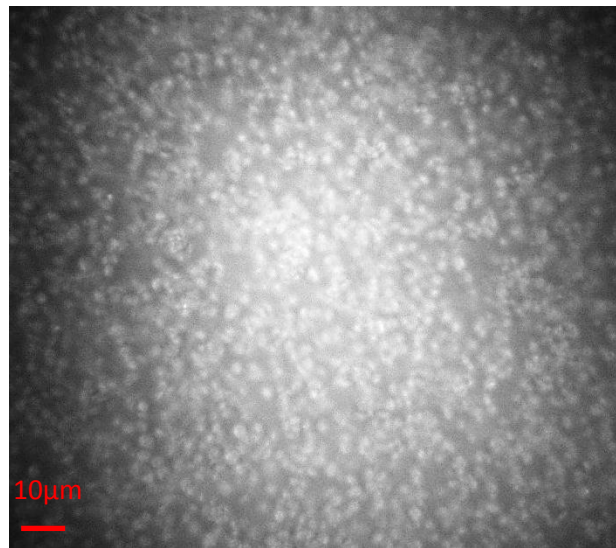
Fig.4.2. An RICM image of the blood platelets progressively rolling and adhering on the footprint of the biofunctionalized channel at shear rate of 1000 s^{-1}. The platelets form a relatively homogenous layer of platelets on the surface of channel with time. A fraction of platelets translocate in the flow direction.

As depicted in Fig.4.2 the single thrombocytes progressive rolling and adhesion on the biofunctionalized channel surface leads to formation of a layer of platelets in active interaction with the channel surface. The platelets roll, reversibly adhere and translocate on the surface of the channel. This results in irreversible adhesion of a fraction of platelets on the

surface of the channel under above mentioned flow condition. The portion of the irreversibly adhered fraction increases with time.
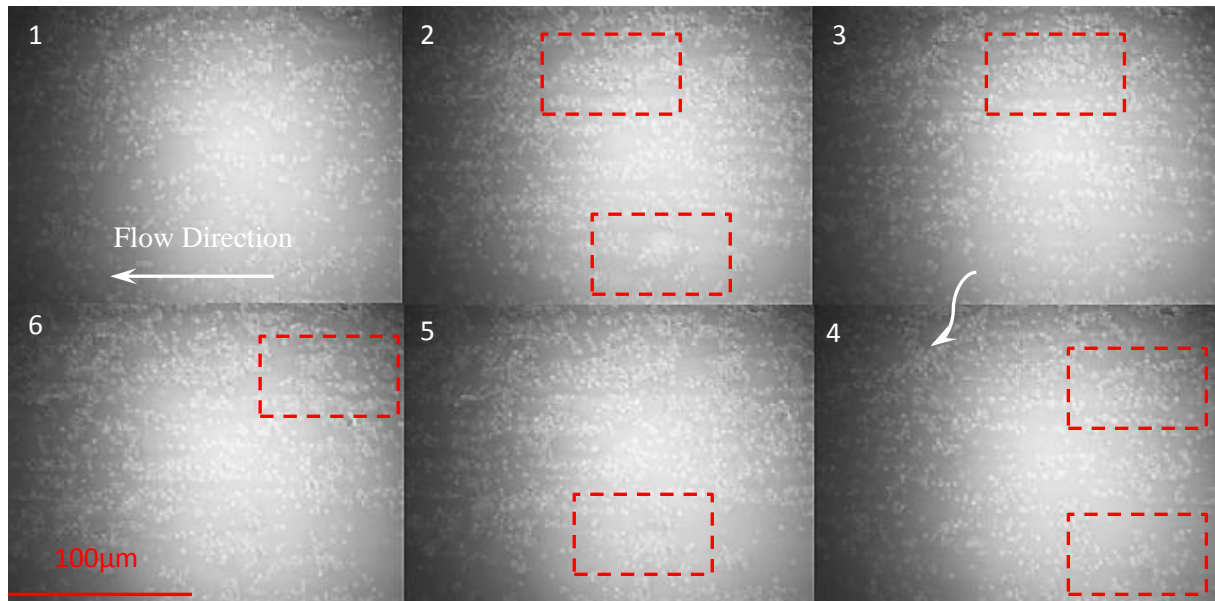
Fig.4.3. The RICM image sequence depicts the formation of long thrombocyte tethers anchored to the channel footprint biofunctionalized with recombinant VWF at 1500 s^{-1}. The dashed rectangulars mark exemplarily the positions where small aggregates have started to assemble, or in a few cases started to roll. A comparison between different image tiles reveals the displacement of single platelets and small aggregates. Images are captured by employing a 63X objective.

Increasing the wall shear rate from 1000 s^{-1} to 1500 s^{-1} changes the form of the accumulated platelet layer from homogenous to long tethers assembled in the flow direction as shown Fig.4.3. The assembly of long tethers happens due to cleavage of a fraction of rolling/adhered single platelets from the surface and their translocation in flow direction, together with simultaneous adhesion of further platelets at both already existing and new adhesion sites. The progressive adhesion of platelets leads to assembly of platelet aggregates. Nevertheless, the blood flow cleaves some of the aggregates. This leads to formation of small platelet aggregates which sometimes fly away with the flow to areas out of the sight of the microscope objective, and in other cases start rolling on the biofunctionalized channel footprint within the sight of the microscope's objective.

It is noteworthy to state that, by increasing the wall shear rate to 2000 s^{-1}, the size of the assembled aggregates progressively increases with time and they start rolling on the channel footprint. In this case, the giant formed aggregates, normally sweep the other already adhered single platelets and platelet aggregates away with themselves from the sight of the observer. However, just after such events, further adhesion of platelets takes place and the whole process of rolling, adhesion, formation of the platelet layer over the biofunctionalized surface repeats itself. Hence, the progressive process of platelet adhesion, aggregate assembly, aggregate disassembly, and aggregate reassembly reproduces itself actively.
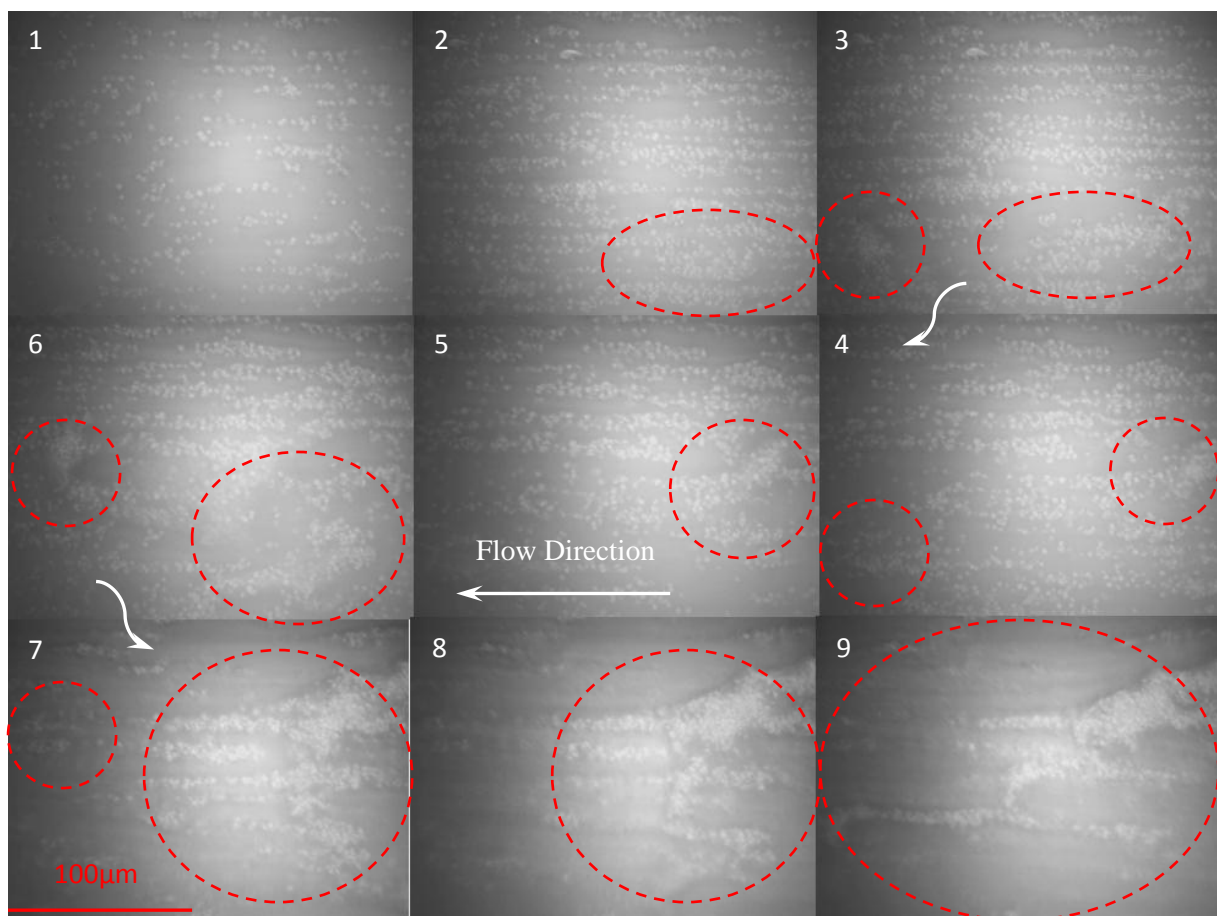

Fig.4.4. The image sequence (tiles No.1-4) depicts the formation of long thrombocyte tethers anchored to the channel footprint biofunctionalized with recombinant VWF at 2000 s^{-1}. As shown in tiles No.5-9, further recruitment of blood platelets leads to growth of platelet aggregates, which in turn leads to formation of huge rolling aggregates sweeping the platelets of the channel footprint. However, after a part of adhered platelets are swept away by a huge rolling aggregate, a new adhesion and assembly process starts. It is noteworthy to state that process reproduces itself each time the surface is swept by a giant rolling aggregate. So the figure sequence is observable during the experimental time. Images are captured with a 63X objective, using RICM method.
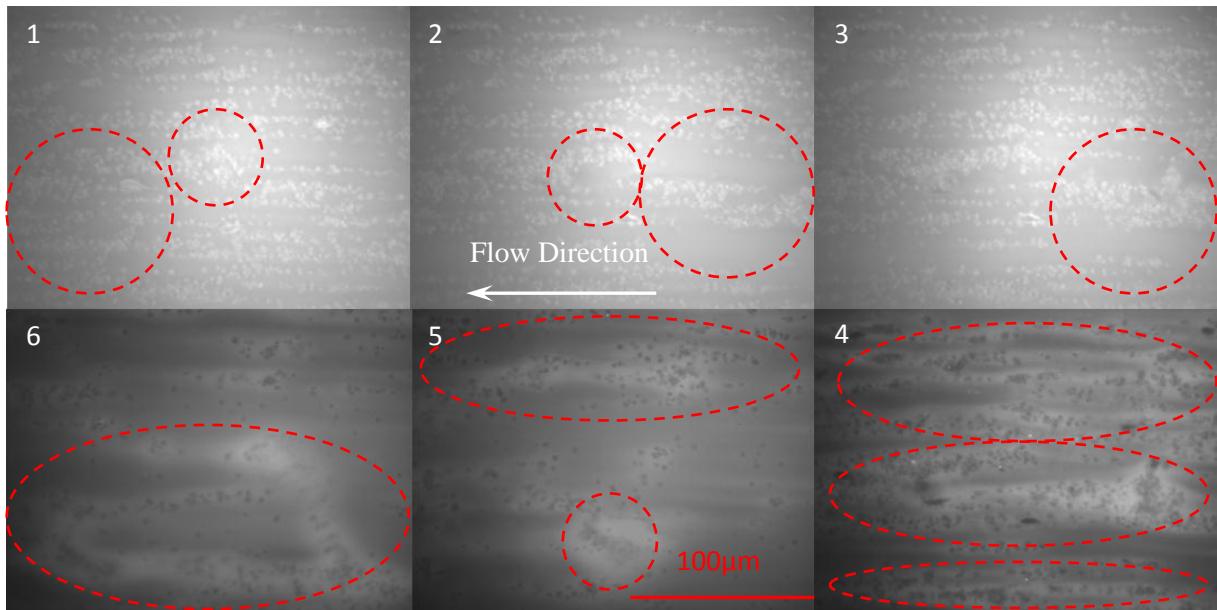
Fig.4.5. The image cascade depicts the assembly, disassembly and reassembly of platelet rolling aggregates on the channel footprint biofunctionalized with recombinant VWF at 2500 s^{-1}. The tiles No.1-3 are captured using RICM method. The tiles No.4-6 are captured using a FITC filter; hence one can observe the presence of the fluorescent labeled circulating VWF binding the platelets together and to the surface (brightness in the areas where the aggregates exist).
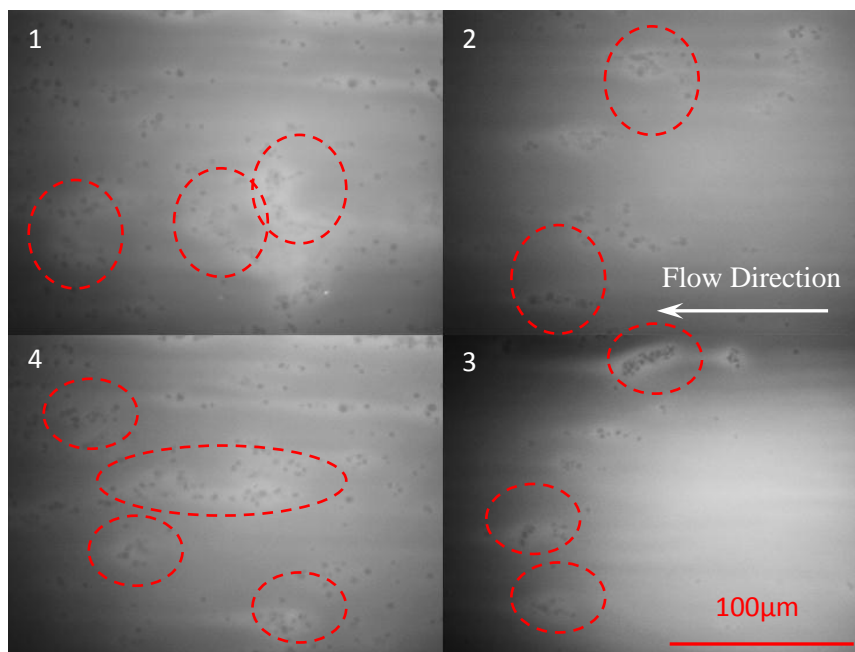
Fig.4.6. The image cascade depicts the assembly, disassembly, and reassembly of platelet rolling aggregates on the channel footprint biofunctionalized with recombinant VWF at 5000 s^{-1}. The images are captured using a FITC filter; hence one can observe the presence of the fluorescent labeled circulating VWF binding the platelets together and to the surface (brightness in the areas where the aggregates exist).

Increasing the wall shear rate to 2500 s^{-1} does not change the nature of the adhesion-aggregation behavior. However, the assembly, disassembly, and reassembly events take place at a higher pace. A schematic image cascade of events is shown in Fig.4.5.

Even under a wall shear rate of 5000 s^{-1} the nature of aggregation behavior remains as for lower shear rates. However, the kinetic of events undergoes a change. The assembly, disassembly and reassembly take place at a much higher pace and the number of visualized giant aggregates reduces dramatically. Despite that, this can be due to high thrombotic activity of the system under such shear rates. At such flow condition formation of giant irreversibly adhered thrombus has been observed on different parts of the channel. Formation of giant thrombus at the entrance of the BioFlux channel system (Fig.4.1) might play a direct role in shortage of platelet-VWF supply to binding sites free at the viewing window of the Bioflux system, where the measurement takes place.

Investigation of adhesion and aggregation of "sticky beads" to the biofunctionalized surface under flow follows a protocol identical to the platelet adhesion and aggregation of thrombocytes. The experiments start at a wall shear rate of 1000 s^{-1} at which the platelet adhesion on a substrate biofunctionalized with VWF tends to begin [14], [24]. Under such a flow condition single functionalized beads adhere to the channel footprint. The adhesion is
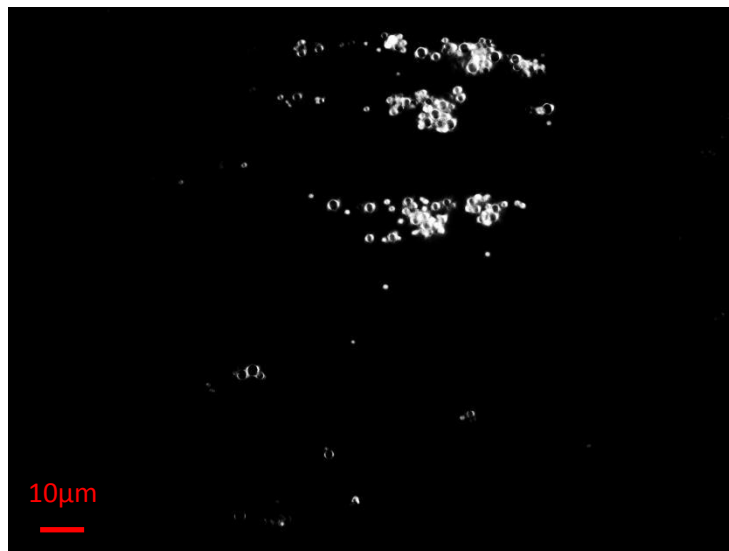
Fig.4.7. An RICM image of the rolling, reversibly-, and irreversibly adhered sticky beads on the channel footprint biofunctionalized with recombinant VWF. The adhesion behavior is progressive. Although few small aggregates/conglomerates form on the surface, they don't show any active rolling behavior. The image is captured with a 63X objective.

progressive and the beads roll, adhere reversibly, and irreversibly on the channel footprint the nature of the adhesive behavior is the same as what has been observed for thrombocytes before. However, the number of beads in active interaction with the substrate is lower in comparison to the number of platelets in similar experiments with platelets. Since the concentration of biofunctionalized beads is 250000 per µl of blood, which corresponds to physiologically relevant concentration, the difference in absolute number of entities interacting with the biofunctionalized surface shall not be due to low number of beads. The difference may be due to the difference in number of the available VWF binding sites between the beads and the thrombocytes, or the homogeneity of binding sites distribution on beads. In spite of that, the fact that the "sticky beads" show a similar behavior to platelets is of extreme scientific importance, since it implies that regardless of the type of VWF receptors available on an arbitrary sphere, the adhesion and aggregation processes are regulated and by VWF.
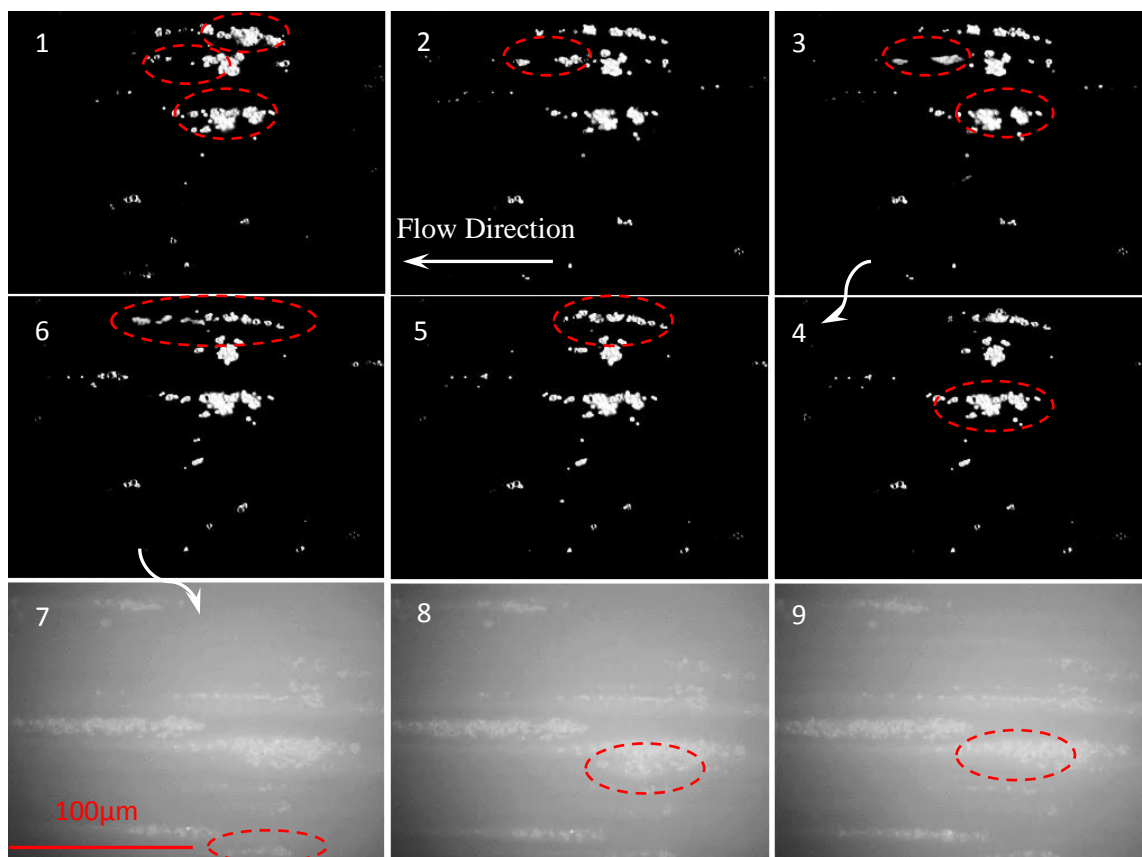
Fig.4.8. These images show the sticky beads adhesion and aggregation process at a wall shear rate of 1500 s^{-1}. The image tiles 1-6 are captured using RICM method. Rolling, reversible-, and irreversible platelet adhesion is observed. Small aggregates assemble on the footprint of the channel. The image tiles 7-9 are captured using a FITC filter. Here, the brighter parts of the image correspond to beads aggregates linked together by circulating fluorescent labeled VWF.
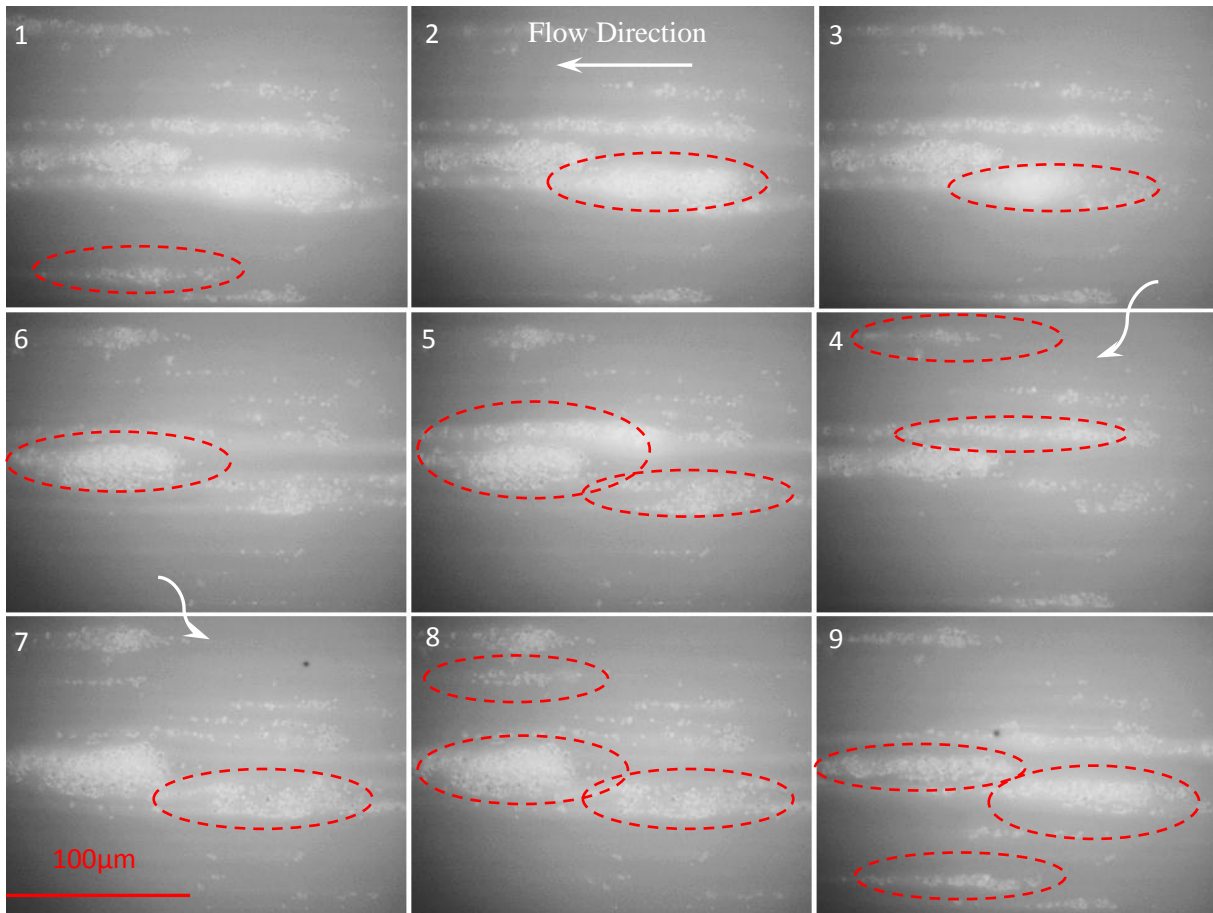
Fig.4.9. The image sequence shows the sticky beads adhesion and aggregation process at a wall shear rate of 2000 s^{-1}.The images are captured by fluorescence microscopy using a FITC filter. Rolling, reversible-, and irreversible platelet adhesion is observed. Big aggregates form on the footprint of the channel. Here, brighter parts of the image correspond to beads aggregates linked together by circulating fluorescent labeled VWF. By following the order of images one can observe assembly of the beads aggregates, their cleavage and translocation on the channel footprint.

Fig.4.7 depicts the rolling, adhesion and formation of small beads aggregates on the channel surface. As depicted in Fig.4.9 an increase of wall shear rate to 2000 s^{-1}, triggers the formation of bigger beads aggregates. By cleavage of the aggregates from the sites of assembly rolling beads aggregates come to existence. Astonishingly, an identical effect has been observed for blood platelets under such flow conditions. The size of rolling aggregates has been increased dramatically in comparison to size of the beads rolling aggregates at 1500 s^{-1}. A similar phenomenon has been observed for blood platelets too. This again highlights the major role of the VWF in platelet-VWF adhesion and platelet-platelet aggregation. The same trend has been observed for aggregation formation and rolling at wall shear rate of 2500 s^{-1}. Figure 4.10 depicts the assembly, reassembly, and disassembly of the beads aggregates on a channel footprint biofunctionalized with the recombinant von Willebrand Factor at 2500 s^{-1}.

This confirms the domination of VWF's role in aggregation regulation at various shear rates, even at absence of platelet GpIbα and the integrin $\alpha_{IIb}\beta_3$ which play an important role in platelet aggregation.
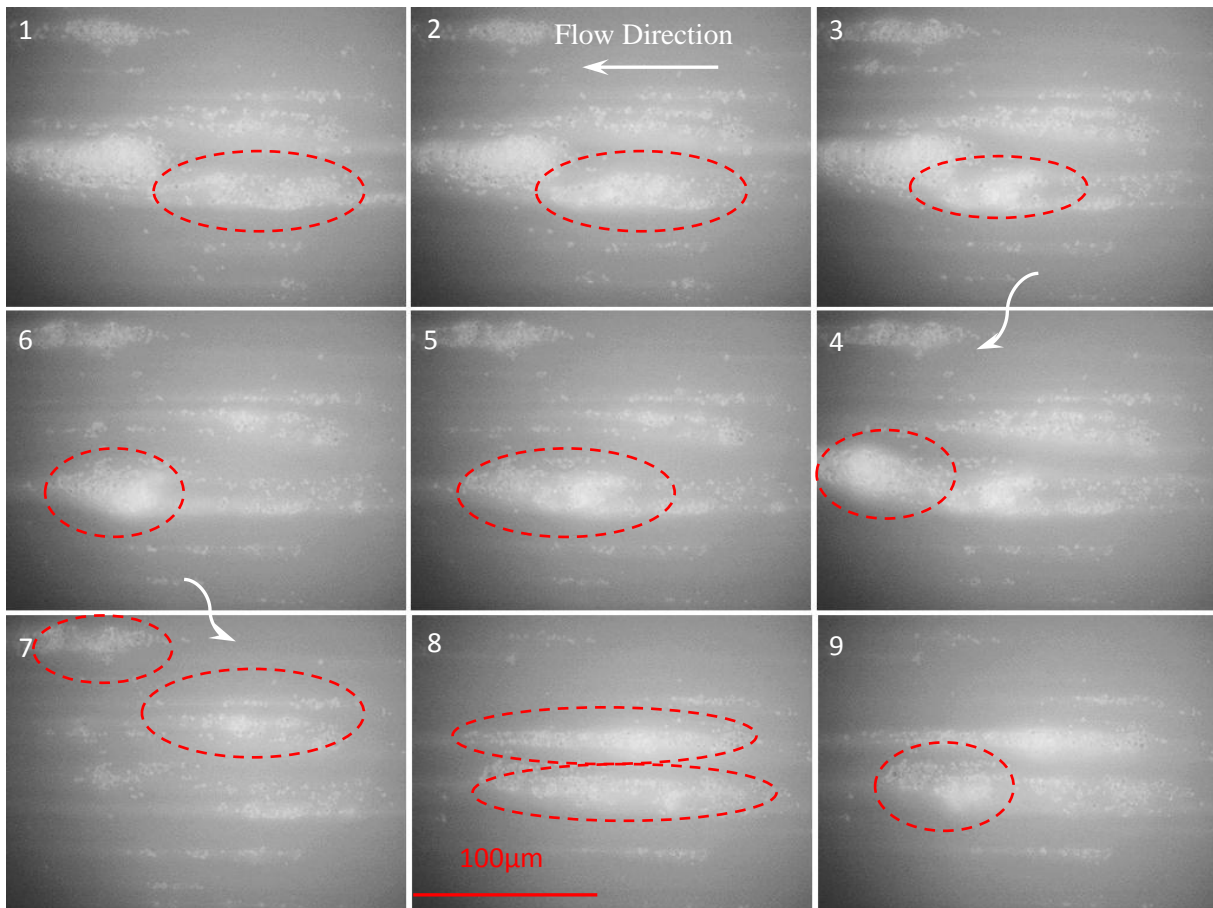
Fig.4.10. This image sequence shows the sticky beads adhesion and aggregation process at a wall shear rate of 2500 s^{-1}.The images are captured by fluorescence microscopy using a FITC filter. Rolling, reversible-, and irreversible platelet adhesion is observed. Big aggregates form on the footprint of the channel. The Here, brighter parts of the image correspond to beads aggregates linked together by circulating fluorescent labeled VWF. By following the order of images one can observe assembly of the beads aggregates, their cleavage and translocation on the channel footprint.

Increasing the wall shear rate to 5000 s^{-1} does not affect the nature of events. The assembly, disassembly, and reassembly still take place. However, the number of giant aggregates shrinks, and the pace of the processes increases. One can still observe the rolling beads aggregates rolling and coming into existence. The immobilized beads remain adhered on the biofunctionalized footprint of the channel for longer. Reduction in size of the rolling aggregates is nearly close to what we have observed for blood platelets. This is another similarity between the platelet aggregates and the bead aggregates that again indicates the

dominant role of the VWF in such processes. The very important fact observed for both platelets and the beads is that, the formation of aggregates at each shear rate is reversible and reproducible. This means, by changing the wall shear rate during the experiments the size and formation factors of aggregation change, but by switching the shear rate to the former value, within a short time the whole process returns to how it was before. The time lag for beads is somehow longer in comparison to the blood platelets themselves. Hence, the force dependency of the process is completely reproducible.
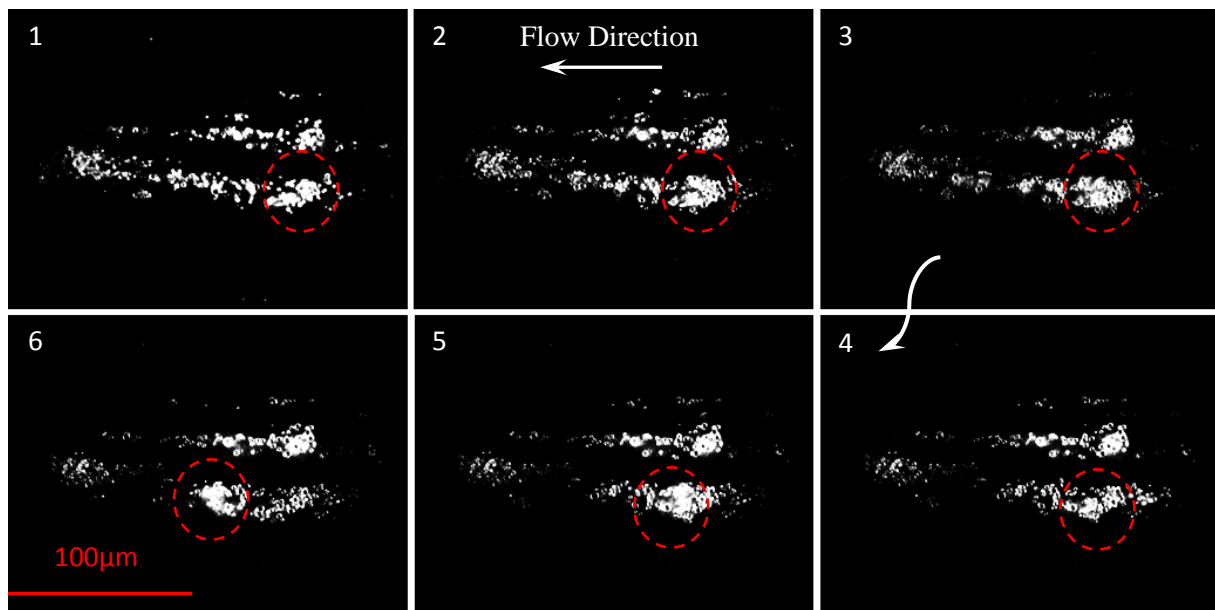
Fig.4.11. This image cascade shows the sticky beads adhesion and aggregation process at a wall shear rate of 5000 s^{-1}.The images are captured by RICM using a 63X Objective. Rolling, reversible-, and irreversible platelet adhesion is observed. Giant aggregates are rarely seen. However, normal aggregates form, adhere, cleave, and roll. Single sticky beads seem to adhere firmly on the channel surface. The dashed circles show the position of beads aggregates translocation along the flow direction. Image block 1-3 shows assembly/growth of an aggregate, and the image block 4-6 shows its rolling/translocation in flow direction.

5. Cancer Cell (Melanoma) Adhesion

5.1. Melanoma Cell Adhesion at Low Shear Rates

The increasing evidence that cancer cell spreading is accompanied by an activation of the coagulatory machinery and may have possible commonalities with thrombotic events, calls for thorough examination of tumor cell adhesion under defined shear flow conditions [29], [90-93]. Despite the key role of VWF among the coagulation proteins in initiating the cellular hemostasis by binding platelets even under high shear flow conditions and the well described relation between VWF and blood platelet immobilization [24-40], VWF and its interactions with melanoma cells under flow conditions remain almost entirely unclear. Since investigation of adhesion behavior of melanoma cells on VWF and coagulation factors fails under static condition, novel microfluidics experimental set-ups in have been developed and employed in order to mimic the melanoma cell adhesion in in-vitro condition.

5.1.1. Melanoma Cell Adhesion in Surface Acoustic Wave Driven Flow and the Bifurcated Geometry

5.1.1.1. Introduction

Accurately mimicking the complexity of microvascular systems calls for a technology which can accommodate particularly small sample volumes while retaining a large degree of freedom in channel geometry and keeping the price considerably low to allow for high throughput experiments. Here, the application of surface acoustic wave driven microfluidics systems for studying of the interrelation between melanoma cell adhesion , the matrix protein collagen type I, the blood clotting protein von Willebrand factor, and microfluidic channel geometry is successfully demonstrated. The versatility of the tool presented enables us to examine cell adhesion under different flow conditions in straight and bifurcated microfluidic channels in the presence of different protein coatings. [44]

Surface acoustic wave (SAW) driven microfluidics are used to examine the regime of low Reynolds numbers (Re), characterizing the flow conditions of our human vascular system. Indeed, generating flow at low Re conditions has been demonstrated to be a challenging task

and many innovative microfluidic solutions for cellomics and proteomics, known as micrototal analysis systems (µTAS), have been designed to overcome this problem. As fluids in such systems are usually driven by external means such as pneumatic pressure or syringe pumps, handling obstacles and the possibility of contamination are common drawbacks of such systems [94]. Even internal pumping methods like electro-osmotic flow or valve-type micropumps which operate based on piezoelectric actuations exhibit some deficiencies which are detailed elsewhere [95], [96]. Driven by the requirements mentioned, a novel method for pumping fluids at low Re has been employed in this work. The method meets the expectations for flexible design which can be used to mimic various two- and three-dimensional geometries encountered in our microcirculatory system, and can handle extremely small volumes of liquid (nl-pl). The technique, which has been successfully employed in multiple research areas within our laboratories [97-100] is based on the interaction of SAWs with a liquid at the surface at which the waves propagate. The planar arrangement not only allows for controlled microfluidic flow (10µl) in complex geometries, such as bifurcations and stenotic conditions, but enormously facilitates surface biofunctionalization with proteins or even confluent cell layers in these small volumes. The hydrodynamic conditions are characterized by combining experimental measurements of the flow field using tracer beads with lattice Boltzmann computer simulations. The latter allows us to calculate the equivalent wall shear rate necessary when estimating the forces acting during cell adhesion. Finally, the biocompatible system is relatively low priced, easy to handle, and can be mounted on any typical microscope. [44]

5.1.1.2. The Acoustic Nano Pump

The general design of our microfluidic flow chamber on a chip is depicted in Figs.5.1. The heart of the channel, the nano pump, is based on acoustically driven flow (Fig.5.1) in which
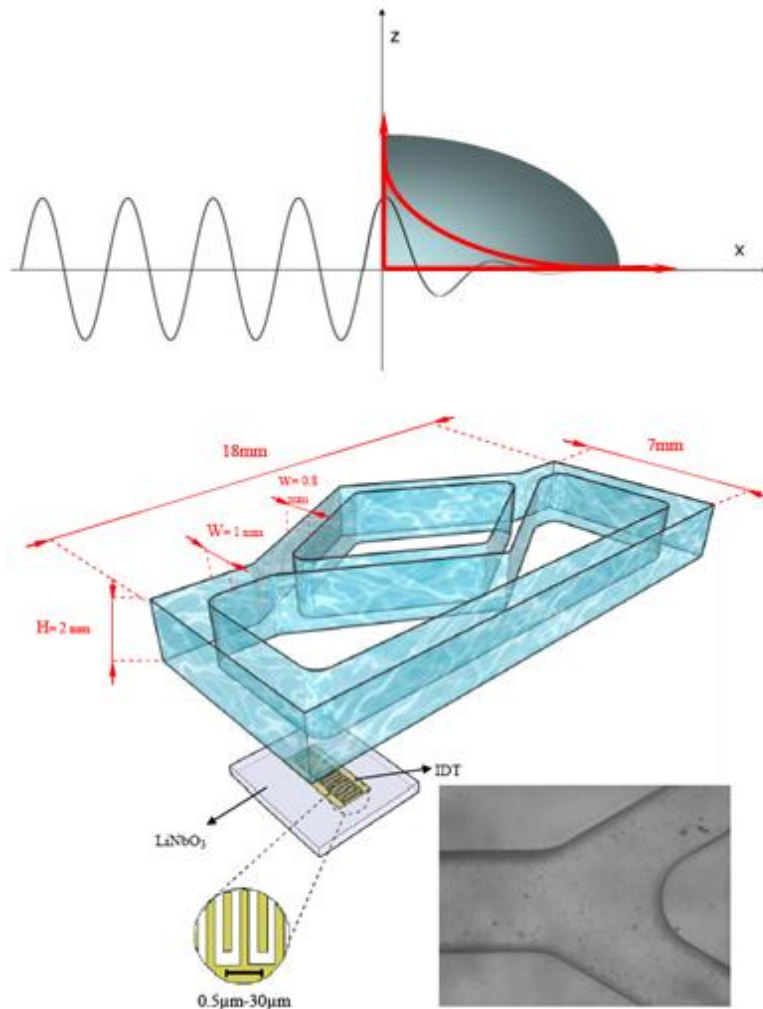
Fig.5.1. Above: Schematic representation of the surface acoustic streaming. The SAW is generated on a piezoelectric material (LiNbO$_3$) employing Interdigitated Transducers (IDTs) and propagates on the solid-air interface. When the wave reaches the solid-liquid interface, acoustic energy is transmitted into the fluid, creating a pressure gradient (shown in red). This pressure gradient drives a continuous flow along the channel. Bottom: Sketch of the bifurcated channel geometry. An IDT is placed to the lower left corner of the bifurcated channel. The IDT is fabricated by the deposition of gold electrodes on the piezoelectric substrate (LiNbO3) and is operated at f =164 MHz. In order to avoid uncontrolled reflections of the SAWs, only 1/2 of the chip is integrated inside the channel. [44]

SAW technology is applied to create surface acoustic streaming [96-102]. In brief, a SAW is essentially a sound wave of about 1nm amplitude and wavelength of typically a few micrometers traveling along a solid-air interface. Due to the poor impedance coupling between substrate and air (large difference in sound velocities in the mediums), only very little energy is dissipated for this "pure mode." However, when a SAW encounters a solid-liquid interface, the impedance coupling changes drastically, causing a large dissipation of acoustic energy into the fluid. The "Acoustically Driven Flow in Capped Microchannels" is thoroughly explained in Appendix No.2.

Dissipation causes an exponential decay of the SAW amplitude within a characteristic length scale of a few wavelengths, which in turn causes an acoustic pressure gradient driving the liquid to flow; an effect called acoustic streaming (Fig.5.1). Considering a typical channel length of a couple of centimeters and a decay length of $\sim$100 μm, the pump essentially acts as a point like pressure source driving the liquid to flow according to conservation of mass [44].

For generation of SAWs interdigitated metal electrodes are deposited on top of the substrate using standard lithography and fed with an input signal of high frequency to generate the SAW. Each individual electrode consists of a set of interdigitated fingers (interdigitated transducers (IDTs)). Due to the high sound velocity (C_{SAW}) of the SAWs ($\sim$4000 m/s), and a typical finger distance (λ) of 10 μm, the matching condition

$$f = C_{SAW}/\lambda \tag{5.1}$$

requires an input signal of high frequency (100 Mhz − 1 GHz), which is generated using a voltage controlled oscillator ("ZX95-200-S," Mini Circuits, USA, Brooklyn). To enable standard protocols for further surface functionalization, the entire surface, including the IDTs, is covered by 50 nm SiOx using standard sputtering methods. It has already shown that this additional layer does not significantly affect the capability of acoustic streaming [100]. Due to the optical transparency of the piezoelectric material employed; we are able to mount the microfluidic chip onto an inverted microscope (Zeiss Axiovert 200, Zeiss, Göttingen, Germany) to study the dynamics of protein stretching and recoiling under different shear conditions [28].

5.1.1.3. Design of the Microfluidic Channel

Bifurcated geometries are very common in our microcirculatory system; nevertheless, their abundance is not the only reason of their investigation. Combining acoustic streaming with bifurcated structures gives us the possibility to benefit from different fluid velocities in a single microchannel and a single experiment. By changing the cross section of the channel before and after bifurcation one can screen for the impact of different flow velocities on the adhesion of cells. The channel footprint and volume are A≈56 mm^2 and V≈112 mm^3, respectively (Fig.5.1) [44]. The geometrical structure of the channel is sketched using AUTOCAD software. The pattern can be transferred to a mold by photolithography or milling techniques. In the present case, the latter technique is applied. The mold has the negative pattern of the microchannel and is filled with polydimethylsiloxane (PDMS) (Dow Corning GmbH, Wiesbaden, Germany), a biocompatible transparent polymer, to obtain the desirable channel structure. The channels produced by this method can be either capped or uncapped. Here, the closed channels design has been chosen to facilitate the application of Lattice Boltzmann computer simulations. The PDMS channel is sealed to the glass slide, which in turn is coupled directly to the chip. The use of a separate glass slide easily enables us to perform cell culture directly on the bottom of the microfluidic channel. [44]

5.1.1.4. Theoretical Study of the Hydrodynamics by Lattice Boltzmann Method

Different velocities imply different shear rates at the boundaries, which are calculated by feeding the computer simulation with experimental data. The hydrodynamic flow profile and the equivalent shear stress of the fluid in the bifurcation

$$\sigma_{eq} = \sqrt{\frac{1}{2}\sum_{\alpha\beta}\sigma_{\alpha\beta}\sigma_{\alpha\beta}} \tag{5.2}$$

can be numerically computed in Lattice Boltzmann computer simulations. It is noteworthy to mention that shear rate or shear stress tensor is a full 3×3 tensor, but in the literature, shear rates are usually reported as scalars, the expected one for the simple shear flow [60]. For this

reason, we have to compute a representative scalar from the tensor. The common approach is to compute the von Mises stress (magnitude) of the tensor, as defined in Eq.5.2. This choice ensures that the effective shear rate extracted from the tensor is exactly the expected one for simple shear flow. The effective shear rate is the shear stress divided by the dynamic viscosity of the fluid,

$$\dot{\gamma}_{eq} = \sigma_{eq}/\mu \tag{5.3}$$

Simulations with boundary conditions corresponding to the described bifurcation geometry have been performed. The only free simulation parameter apart from the fluid density and viscosity is the central inlet velocity. A value of v = 1.4 mm/s was measured in our experiments. The total volume flux through the channel is found to be slightly larger than φ = 1.4 mm^3/s. A computational grid of $400 \times 286 \times 102$ lattice nodes has been used for the simulations. The visualizations of the flow profiles have been created using *PARAVIEW** [44].

Running Lattice Boltzmann simulations for the bifurcated geometry shown in Fig.5.1 provides us with a precise evaluation of wall shear rate, and flow velocity in different parts of the channel. Table 5.1 presents us the overview of hydrodynamic conditions in which the experiments are conducted. The more detailed graphs are available in section 5.3.

Table.5.1. Maximum values of equivalent shear rate and velocity magnitude before and behind the bifurcation, 10µm above the bottom wall. The results have been extracted from the Lattice Boltzmann simulations. [44]

Variable	Before Bifurcation	After Bifurcation
Maximum Shear Rate	4.42/s	3.17/s
Maximum Velocity	0.045 mm/s	0.032 mm/s

5.1.1.5. Biofunctionalization of the Microchannels

5.1.1.5.1. Biofunctionalization with Collagen

Biofunctionalization for different µ-fluidic patterns is usually a complex process. In the present case of capped geometry, however, this becomes an easy task for even complex channel geometries. For our studies, in which we examine VWF's shear dependent hemostatic potency, the main coating of the track is collagen, which is known to present a VWF binding site [108], [109]. The inside of the channel is coated with collagen type I (C7661, Sigma Aldrich, St. Louis, USA) in a concentration of $c \approx 10$ µg/cm^2 as previously published [108].

5.1.1.5.2. Biofunctionalization with Collagen and VWF

After the collagen coating was deposited as described above, a layer of plasmatic VWF (Baxter, Vienna, Austria) in PBS buffer solution with a concentration of $c \approx 70$ µg/l was added. In order to achieve an effective coating, we allowed the VWF in the solution to precipitate over a few hours onto the collagen layer before beginning adhesion experiments.

5.1.1.6. Cells and Cell Culture

Melanoma cells of the amelanotic subclone A7, with maximized migration activity resulting from transfection with actin binding protein, were used for all of the experiments. Cells were cultured in a cell culture medium consisting of Eagle's MEM media (PAA, Leipzig, Germany) supplemented with 10% fetal calf serum (Biochrom, Berlin, Germany) and 1% penicillin/streptomycin (PAA, Leipzig, Germany). Cells were grown to confluence, removed with trypsin and resuspended in the cell culture medium, before being injected into the microchannels.

5.1.2. Melanoma Cell Adhesion in Continuous and Pulsatile Surface Acoustic Wave Driven Flow

Investigation of melanoma cell adhesion at shear rates slightly higher than those studied in section 5.1.1 is necessary to enlighten us more concerning the nature of the adhesive behavior of cancer cells, especially melanoma cells, toward the endothelial matrix protein collagen, and the coagulation protein VWF. Considering the advantages of the surface acoustic driven flow discussed before, the basics of the experimental set up remain the same as in section 5.1.1, except for the bifurcated geometry that is replaced with a simpler geometry, sketched in Fig.5.2. Besides that, the biofunctionalization of the channel is done identically to what has been described in section 5.1.1, with an exception of using recombinant VWF from the same supplier (Baxter, Vienna, Austria) instead of the plasmatic VWF. This happens due to the plasmatic VWF availability issues.

Another matter studied in this section is the effect of continuous and pulsatile flow on the adhesion of melanoma cells to the biofunctionalized substrate, for which the acoustic streaming is the excellent method of choice due to the high level of programmability that this method provides.

Measurement area is set to be far from the IDT
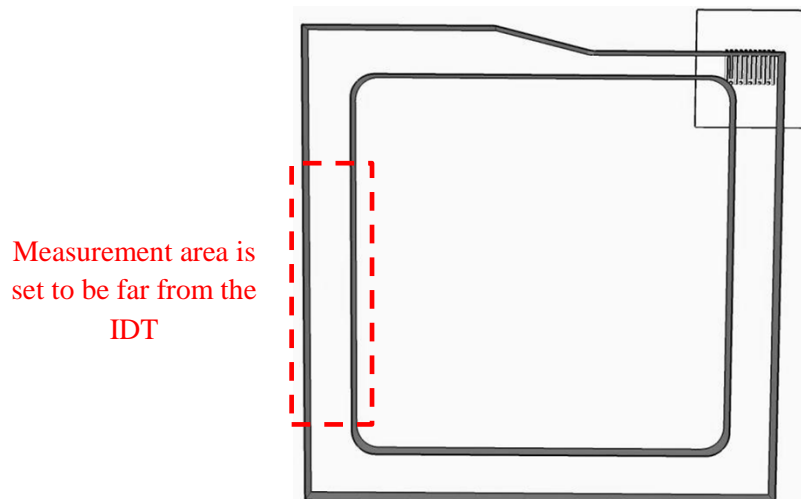
Fig.5.2. A representative sketch of the channel used for studying the adhesion of melanoma cells under flow condition at a wall shear rate of $10s^{-1}$. The length of channel at each side is equal to 1cm. The height of the channel reads 0.5mm. The width of the channel reads 1mm at the measurement point and 0.5mm at point of coupling with the IDT. The positive effect of narrowing the channel at the coupling point on the streaming velocity has been discussed thoroughly in Appendix No.2.

For adhesion experiments conducted under continuous flow conditions the same experimental set up as described in section 5.1.1 is employed. However, for generation of pulsatile flow the voltage controlled oscillator is adjusted in order to trigger a signal with a frequency of 1Hz. The maximal flow velocity at the center of the channel reads $\approx$ 2.5mm/s, and creates a wall shear rate of $\approx$ 10s^{-1}. The measured maximal flow velocity and wall shear rate is equal for the continuous flow and the pulsatile flow at the time intervals in which streaming takes place. The maximal flow velocity is measured by calculation of the time of travel for tracing beads (10μm in diameter) at the channel center.

5.2. Melanoma Cell Adhesion at Higher Shear Rates

Investigation of melanoma cell adhesion at wall shear rates higher than 10 s^{-1} completes the understanding of the adhesive behavior of melanoma cells to the endothelial matrix protein collagen, and the coagulation protein VWF, under physiological conditions where higher vessel wall shear rates rule. However, for such investigations at higher shear rates, application of conventional microfluidics are better established and more practiced. Hence, the set-up that has been successfully employed in the experiments described in chapter 3 (Fig.3.1) has been adopted for investigation of melanoma cell adhesion in this section. A relatively wide range of vessel wall shear rates has been studied using the stenotic channel. Using th ethe aforementioned set-up, melanoma cell adhesion on biofunctionalized channel footprint under wall shear rates 50s^{-1}, 100s^{-1}, 250s^{-1}, 500s^{-1}, and 1000s^{-1} is studied. Biofunctionalization protocols and cell preparations methods identical to those explained in section 5.1.

5.3. Results

It has previously been shown that freely circulating melanoma cells can firmly bind to the extracellular matrix of the blood vessel possibly initiated by integrins [110], [111]. In a first step toward understanding the fundamental principles of VWF-melanoma cell interactions, the study of melanoma cell adhesion under low shear rate condition ($\sim$2s^{-1} – $\sim$5s^{-1}) in bifurcation has been performed, before tackling the scenario of higher shear rates. Prior to the

actual adhesion experiments, the flow profiles were thoroughly analyzed and characterized in a manner combining theory and experiment. From the analytical solutions of the channel flow, one obtains the equivalent shear rate and velocity near the footprint of the channel, cf. Table.5.1. The entire cross section of the equivalent shear rate at h=10 μm above the bottom wall is shown in Fig.5.3. This distance approximately corresponds to the radius of the melanoma cells. The maximum near-bottom velocities and shear rates 10 μm above the footprint of the channel are v = 0.045mm/s and $\dot{\gamma}$ = 4.4/s in front of the bifurcation and v = 0.032 mm/s and $\dot{\gamma}$ = 3.2/s behind the bifurcation, respectively, and the values in front of the bifurcation are 1.4 times larger than those behind. [44]
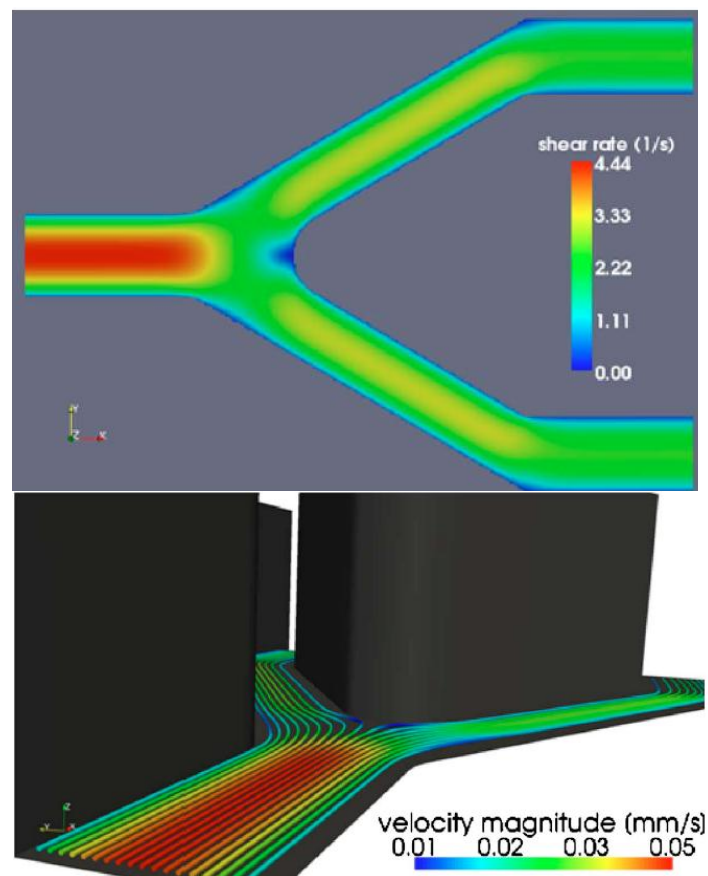
Fig.5.3. Above: The simulated profile of the equivalent shear rate, 10 μm above the bottom wall of the channel. Using the experimentally extracted velocity profile, the shear rates can be quantitatively calculated and the maximum shear rate is $\dot{\gamma}$ = 4.4/s in front of and $\dot{\gamma}$ = 3.2/s behind the bifurcation. Bottom: Streamlines of tracer particles near the footprint. The initial distance to the wall is 10 μm and remains almost constant during the entire travel through the bifurcation. [44]

Streamlines for tracer particles near the bottom wall are shown in Fig. 5.3. The simulations show that particles initially moving in x-direction remain roughly at the same distance of the bottom wall. This is because the vertical component of the velocity is very small as compared with those components parallel to the bottom wall. As a consequence, particles near the center of the channel inlet will never come close to the bottom. However, this is only true for dilute suspensions, where the overall velocity profile is not significantly influenced by the presence of particles. In the present study, this is well justified and important as it ensures that only a small number of cells will be able to collide and bind to the surface. It points out that the laminarity of the flow conditions in such channels will keep 95% of the cells off the wall. This must be taken into consideration when calculating binding constants or substrate affinity.Numbers assuming simple bulk/surface equilibrium, i.e., taking all immersed cells into account, will be off by up to a factor of 100, indicating a major underestimation of binding constants. [44] From a mechanical point of view the bifurcated channel resembles physiological flow conditions in our microvascular system and from an experimental point of view it allows to screen for the impact of fluid dynamics of a complicated geometry on the melanoma cell adhesion. The channel geometry shown in Fig.5.4 for example features both straight as well as bifurcated flow conditions.
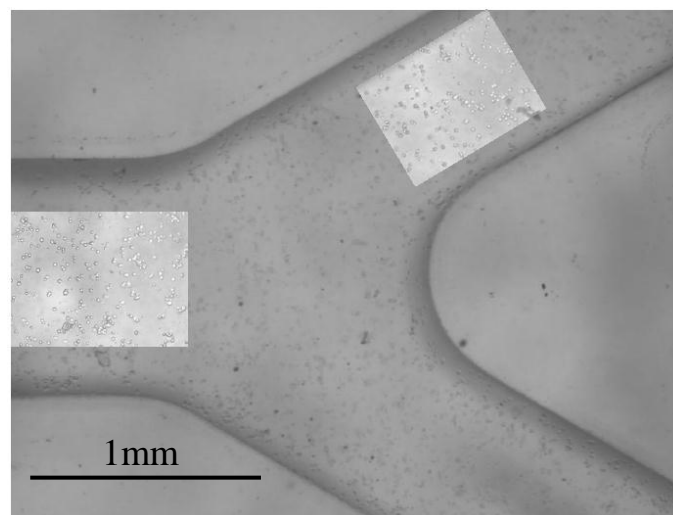
Fig.5.4. A schematic representation of living melanoma cells under flow inside a biofunctionalized μ-channel. The bifurcation region is captured through a 2.5X objective. A zoom-in view (highlighted boxes) of the regions before and after bifurcation is shown and indicates where measurements have taken place. [44]
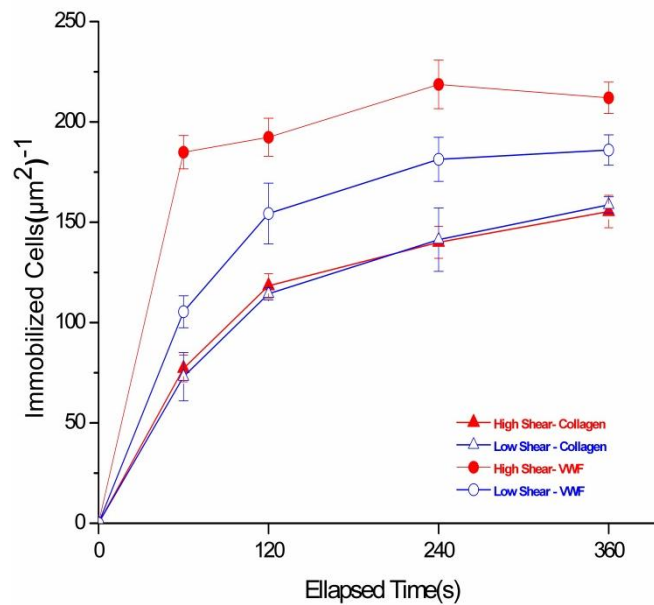
Fig.5.5. Cancer cell immobilization under flow condition for different biofunctionalized surfaces and hydrodynamic conditions. Collagen and collagen + VWF coats have been tested. The melanoma cell adhesion on the collagen coated μ-channel (filled and open triangles) does not show shear rate dependent behavior. This is in contrast to the melanoma cell immobilization in the VWF coated channel (filled and hollow circles), where an increase in shear leads to an increase in adhesion under otherwise identical hydrodynamic condition. [44]

The number of immobilized cells at the bifurcated channel bottom was monitored over time at two different positions as depicted in Fig.5.4. Adhesion in the elongated and bifurcated channel parts has been analyzed. For the two different biofunctionalizations which have been tested; collagen, and VWF coated on a thick collagen layer, a clear increase for collagen to VWF by a factor of 2 has been found. Initially, the number of immobilized cells increases until the curve begins to saturate at around $t = 120s$ (Fig.5.5). The zero point of the y-axis is defined by subtracting the number of cells already adhered at the beginning of each experiment ($t = 0$ s) from the total number of adhered cells at the end of each $\Delta t =120$ s measurement period. This provides a plot of the increase in adhered cells per area and time.

On the channel biofunctionalized with collagen the absolute number of adhered living cells is nearly identical in both regions of before and after bifurcation, demonstrating that the underlying adhesion mechanism does not depend significantly on applied shear. However, introduction of immobilized VWF to the coating causes an increase of factor 2 in the number of adhered cells. Surprisingly, the increase in adhesion due to VWF is more pronounced close to the bifurcation, which reveals the importance of hydrodynamic effects for cell adhesion.

78

Until now, we do not have any obvious explanation, but would like to hypothesize that VWF and its shear stress activation is even more pronounced in the presence of bifurcation. It is important to note that given the relatively high area to volume ratio, the total number of "free" cells inside the channel cannot be considered to be constant in closed microfluidic systems. From the average number of cells adhered to the bottom of the channel, we calculate a decrease of 22% − 36% in the number of flowing cells in lower laminas of flux after 120 s. The rate of decrease is dependent on the shear rate and coating of the channel. Another important property of such a microfluidic system is its laminar character. The simulation reveals that beads of one plane show only very little exchange with the adjacent laminar layers (Fig.5.3), implying that only very few cells are actually candidates for collisions with the bottom of the μ-fluidic channel. This renders our data somewhat insensitive to fluctuations in the total cell concentration as a fluctuation ΔN of cells in a certain volume corresponds to layer fluctuations of only $l\Delta N^{2/3}$, where $l = \Delta l/L_0$ is the relative thickness of the layer (Δl) compared with the entire channel height L_0. A total decrease in bulk concentration by $\Delta C/C_0 = 10\%$ therefore corresponds to a decrease in layer concentration of less than 5% and remains therefore within our error bars. On the flip side, it becomes clear that calculating the binding affinity based on the ratio of free-to-bound cells proves challenging and requires a careful hydrodynamic and thermodynamic analysis. This is due to the fundamental problem of defining the system under such conditions, and is not specific to our setup. [44]
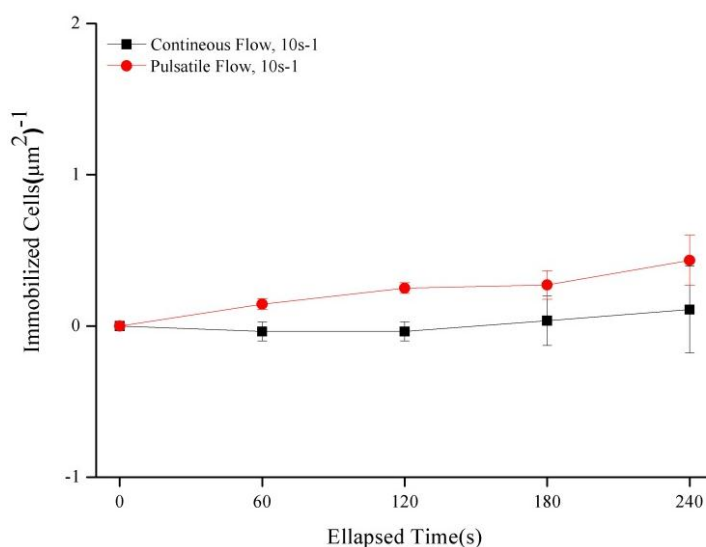
Fig.5.6. The adhesion of melanoma cells under continuous (filled black squares) and under 1 Hz pulsatile flow (filled red circles) on a channel biofunctionalized with collagen+VWF. The adhesion is nearly zero at both flow regimes at $10s^{-1}$.

The adhesion of melanoma cells on the channel bifurcated with VWF doesn't show a clear shear force dependency in the investigated shear rate range. Thus, a wider shear rate range has to be investigated. Hence, the adhesion behavior of melanoma cell at a shear rate of ~10s^{-1} has been studied. This has been performed in the simple microchannel geometry sketched in Fig.5.2. The microchannel has been built using the same procedure explained before. The biofunctionalization process is also identical to the one described in section 5.1.1.5.2, with one exception. Due to availability issues the plasmatic VWF is replaced with recombinant VWF of the same concentration and from the same provider (Baxter, Austria). The data analysis and evaluation process is identical to the process performed for bifurcated channel. However, for this shear rate, the investigations are not only done in a continuous flow with a velocity of 2.5 mm/s, but also with a pulsatile flow with a frequency of 1 Hz and an identical flow velocity. Surprisingly, the adhesion rate drops dramatically with the increase of shear rate from < 5 s^{-1} in bifurcated geometry to ~ 10 s^{-1} in the simple capped channel. However, adhesion rate of 0 shown in Fig.5.6 does not indicate that there is absolutely no cells adhered on the channel footprint. But, the zero point of the y-axis is defined by subtracting the number
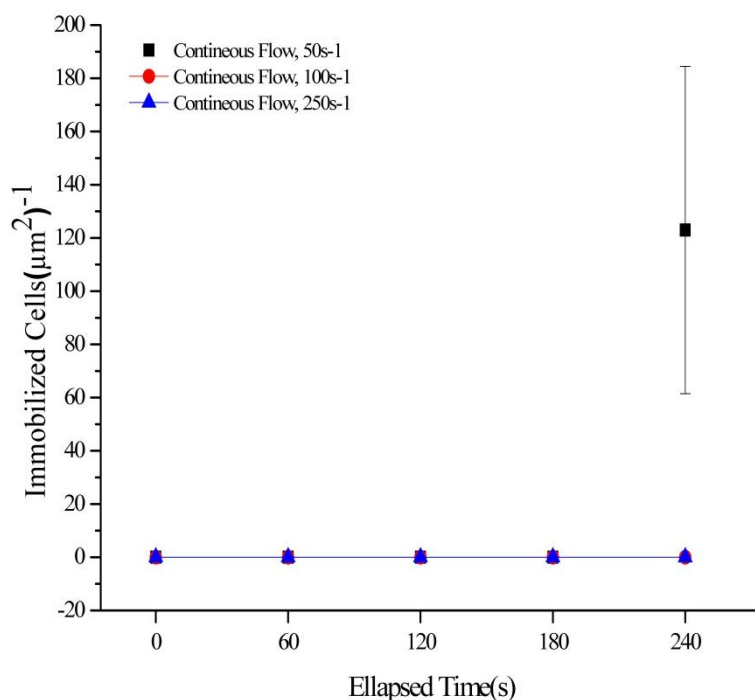
Fig.5.7. Adhesion rate of the melanoma cells on collagen+VWF coat at shear rates of 50 s^{-1}(filled black squares), 100 s^{-1}(filled red circles), and 250 s^{-1}(filled blue triangles), is sketched for experimental periods of Δt = 60 s, during 4 minute long experimental times.

of cells already adhered at the beginning of each experiment ($t = 0$s) from the total number of adhered cell at the end of each $\Delta t = 60$ s measurement period. However, the rate of adhesion is extremely low under continuous flow condition. Another outcome of these experiments is that the adhesive behavior of the melanoma cells on the footprint of the channel coated with VWF under pulsatile flow is identical to the continuous flow, as sketched in Fig.5.6. The results of melanoma cell adhesion at $10s^{-1}$, and the sharp decrease in adhesion from < 5 s^{-1} in bifurcated geometry to ~ 10 s^{-1} makes the obligation to investigate the shear rate dependency of the melanoma cell adhesion at other higher shear rates obvious. Hence, the adhesion behavior is studied at range of higher shear rates. For these investigations, the stenotic microchannel that has been used in chapter 3 for studying the adhesion of the thrombocytes on VWF is employed (Fig.3.1). According to the findings mentioned above, adhesion of melanoma cells under the flow conditions of higher shear rates remains literary close to zero, as shown in Fig.5.7.

The data for melanoma cell adhesion at $500s^{-1}$, and $1000s^{-1}$ has not been shown in Fig.5.7. Tough, the adhesion rate of melanoma cells at these shear rates is absolute zero. However, as discussed before in chapter 3, a strong advantage of application of stenotic µ-channels is the simultaneous existence of different flow velocities and as a result varying wall shear rates at
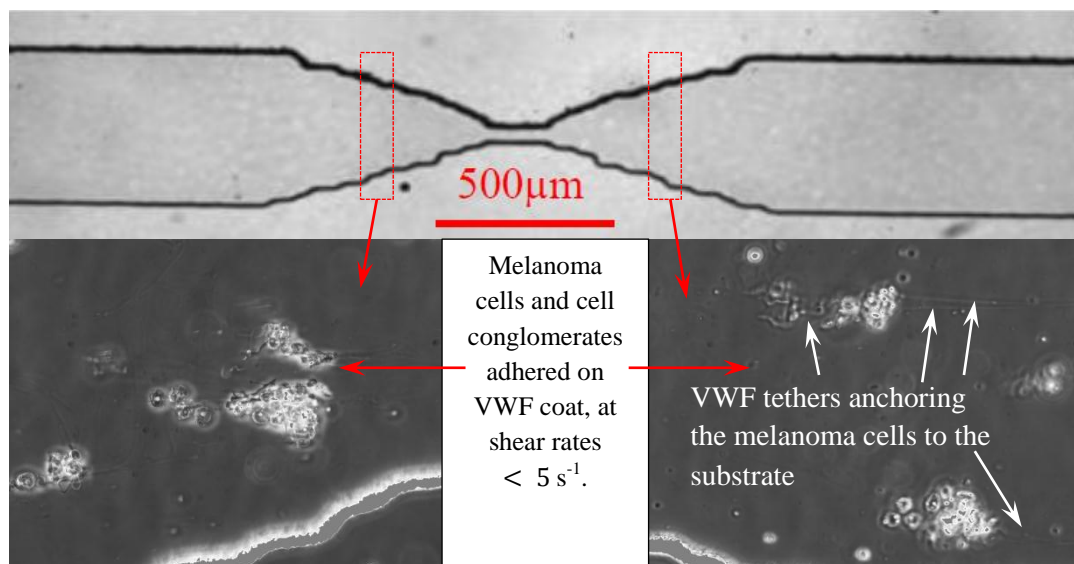
Fig. 5.8. Schematic representation of adhesion of melanoma cells on the collagen+VWF coated channel, at the sections with shear rates smaller than 5 s^{-1}. The images are captured by the 20X objective of a phase contrast microscope. Adhesion at this low flow condition confirms the results of the adhesion behavior of melanoma cells in bifurcated geometry studied before.

different sections of the channel. Here, as the wall shear rate inside the constriction has been set to a value of $250s^{-1}$, the shear rate in wider sections of the channel would be in the order of $< 5\,s^{-1}$, as shown in Fig.3.6. This is nearly the fluid dynamic condition in which the experiments in bifurcated experiments have been conducted. As expected, by investigation of melanoma cell at those sections of the channel under lower shear rate regime ($< 5\,s^{-1}$) shown in Fig.5.8, one can observe higher cell adhesion close to values observed in bifurcated geometry before. This again confirms the effect of complex fluid dynamic condition on melanoma cell adhesion, and the ability of both the acoustically driven and the pressure driven setups (syringe pump) in mimicking the necessary fluid dynamic condition for cell adhesion.

Another important fact observed during these experiments is that the melanoma cell adhesion on VWF succeeds just when the channel has already been biofunctionalized with a layer of matrix protein collagen prior to further biofunctionalization with VWF. However, this doesn't necessarily mean that adhesion is just dependent on presence of collagen and its binding sites, since at shear rates $\geq 10s^{-1}$, no adhesion of melanoma cells to a standing alone collagen coating has been observed. Not mentioning that the bigger melanoma cell conglomerates are mostly anchored to channel's biofunctionalized footprint by long tethers swinging in the direction of flow. This type adhesive behavior has been solely observed in our various experiments with VWF, and does not seem to be typical of collagen.

6. Conclusion

In this work platelet and melanoma cell adhesion under complex flow conditions arising in microvascular system have been studied. Rise of complex fluid dynamic effects under physiologically valid flow conditions adds to the complexity of the biological processes taking place in the microcirculation system. Various geometries have been developed to mimic a variety of flow conditions at which adhesion processes in vessels take place. Novel microfluidics techniques, as for example acoustically driven flow have been successfully utilized and further developed for performing the experiments. The biofuntionalization methods have been developed by following the works of other renown researchers and further development of the already available methods in our labs. These together with maintaining an exactly defined experimental plan have led to various findings which shed light into our understanding of cell adhesion, coagulation and matrix proteins under flow condition.

The experimental and theoretical investigation of flow condition in constricted geometries has revealed a rise of asymmetrical streaming profiles at inlet and outlet of the constriction at Reynolds numbers in the order of 100, together with a disproportionate increase of effective von Mises stress σ_{vM} with rise of Reynolds number. The latter is a phenomenon of extreme importance since some adhesion processes are force sensitive, especially when it comes to adhesion of cells that interact specifically with VWF.

After thoroughly studying the fluid dynamics in constricted channels, the adhesion and adhesion fluctuations of blood platelets in microchannels have been investigated. The development of stenotical microchannels, their successful biofunctionalization with coagulation protein VWF and matrix protein collagen made the investigation of the specific adhesion of thrombocytes on these important hemostasis factors under stenosis flow condition possible. It has become clear that the adhesion of thrombocytes suspended in blood plasma (Platelet Rich Plasma) on immobilized VWF is progressively shear force dependent, even in absence of hematocrit. The compressive forces that drive the thrombocytes towards the vessel wall (Fahraeus-Lindqvist effect) where the platelet activation and adhesion take place, vanish in absence of hematocrit. Hence, the progressive shear dependent adhesion of platelets observed here is to a lesser degree dependent of hematocrit and tissue factor activation of platelets, and more specific of VWF and thrombocytes.

It was expected that with increase of wall shear rate the VWF takes a more dominant role in platelet adhesion; while due to its shear dependent shape conformation it reaches its fully stretched form at higher shear rates. Thus, the necessary domains for thrombocytes adhesion are very well exposed. The results of the adhesion fluctuation experiments are in complete accordance with these expectations, as the relative fluctuations in platelet adhesion (sd/N_{mean}) reduce dramatically with increase in wall shear rate.

The adhesive behavior of thrombocytes toward the immobilized deglycosylated plasmatic VWF has also found to be close to those of plasmatic VWF. Counter intuitively, this implies that the N-linked oligosaccharides do not affect the thrombotic behavior of the plasmatic VWF drastically. Since the experiments have covered a very wide range of the physiological fluid dynamic condition, these results are of extreme importance for shedding light into the very complicated topic of the role of the oligosaccharides in functionality of von Willebrand Factor. However, studying the effect of removing the O-linked oligosaccharides would also be a matter of importance.

While the adhesion of individual platelets on VWF coating has been discussed in chapter 3, we have proceeded to study the collective behavior of platelet-VWF assemblies, based on VWF-platelet and platelet-platelet interactions. Studying the formation of rolling aggregates is a vital part of understanding the adhesion processes involved in thrombotic activities taking place under dynamic conditions in microcirculatory system. Although, the formation of platelet aggregates under complex flow conditions has been studied thoroughly from a biomedical view, understanding the physical role of VWF has not been performed before. To clarify the role of the key players (platelet and VWF) the blood platelets have been replaced by "passive" but "sticky" biofunctionalized borosilicate glass spheres 2 µm in size. We clearly demonstrate that VWF and not the blood platelets is the pivotal ingredient for the observed reversible rolling aggregates. It is successfully demonstrated that not only VWF is able to bind to functionalized glass beads, but also it maintains its function in formation of rolling aggregates under similar fluid dynamic conditions in which the platelet rolling aggregates assemble. In fact, the VWF is the factor which initiates and maintains the formation of rolling aggregates in absence of blood platelets and their GpIbα and the integrin $\alpha_{IIb}\beta_3$ receptors.

Cell adhesion is not only a crucial step in blood clotting as investigated in chapter.3, but is also believed to play an important role in cancer metastasis. Investigation of melanoma cell adhesion under different flow conditions has clarified the nature of melanoma cell adhesion

on VWF, and the matrix protein collagen type I. It is clear now that the adhesion of melanoma cells on an immobilized VWF coat over a deposited collagen layer, takes place at shear rates $\leq 5\,s^{-1}$. Presence of the VWF coat on the top of a collagen coat increases the adhesion rate by a factor two at this flow condition. Surprisingly, even at such low shear rates we were able to detect a shear dependent adhesion rate for the collagen+ VWF coat, which is absent with collagen only coat. Given the relatively minor increase in wall shear rate, this was unexpected. We hypothesize it is due to the rather complex fluid dynamic of bifurcated geometries. A Change in adhesion rate due to complexity of flow conditions arising in bifurcated geometries has been observed under this flow condition. Regardless of the fluidic set up employed for experiments adhesion of melanoma cells at shear rates $\leq 5\,s^{-1}$ has been observed when a VWF coat is deposited on the top of a collagen coat. However, a standing alone VWF coat did not initiate melanoma cell adhesion.

Surprisingly, with increasing the wall shear rate to $10\,s^{-1}$ the adhesion rate drops close to zero, regardless of the continuous or pulsatile flow regime. Further increase of shear rate also does not change this behavior. Hence, adhesion of melanoma cells to VWF does not follow the same mechanisms as the shear induces thrombus adhesion. The observation of increased melanoma cell adhesion on endothelial cell–VWF interface under whole blood condition (private communication with the research group of Prof. Dr. S. W. Schneider) remains unclear. We hypothesize that the endothelial cells-VWF interface presents conditions which can not be mimicked by a "simple" protein coat.

The presented results clearly demonstrate the role of hydrodynamic for microvascular function. Channel geometry, flow rates and biological key players for adhesion process blood platelets have been carefully investigated in various microfluidic systems (SAW driven flow, syringe pump driven flow, PDMS channels, etc…). Our data not only represent a technological milestone for further investigation of other various physiological factors, including the role of ADAMTS13 and the O-linked oligosaccharides in platelet adhesion, but also lay out some key results on how macroscopic platelet aggregates arise, how the shear rates influence the cancer cell adhesion, and the role of glycosylation in platelet adhesion.

References:

[1] George A. Trusky, Fan Yuan, David F. Katz, *Transport Phenomena in Biological Systems*, Second Edition, Pearson Education Inc., publishing as Prentice Hall, 2010, ISBN-13: 978-0-13-513154-1.

[2] S. Whitaker, *Introduction to fluid mechanics*, 1968, Malabar, FL: Krieger Publishing Company.

[3] F. White, *Fluid Mechanics*. 1986, New York: McGraw-Hill Book Company.

[4] R. Fahraeus, T. Lindquist, Am. J. Physiol. 96:562, 1931.

[5] E. W. Merrill, E. R. Gilliand, G. Cokelet, H. Shin, A. Britten, and R. E. Wells, *Rheology of blood and flow in the microcirculation*. J. Appl. Physiol. 18(2): 255-260., 1963.

[6] Anthony S. Fauci, Eugene Braunwald, Dennis L. Kasper, Dennis L. Kasper, Stephen L. Hauser, Dan L. Longo, J. Larry Jameson, Joseph Loscalzo, *Harrison´s Principles of Internal Medicine,*Publisher: McGraw-Hill Professional; 17 edition (March 6, 2008) (ISBN-10: 0071466339, ISBN-13: 978-0071466332).

[7] E. Tolouei, C. J. Butler, A. Fouras, K. Ryan, G. J. Sheard, J. Carberry, *Effect of Hemodynamic Forces on Platelet Aggregation Geometry,* Annals of Biomedical Engineering, Vol. 39, No. 5, May 2011 pp. 1403–1413.

[8] T. Colace, E. Falls, X. L. Zheng, S. L. Diamond, *Analysis of Morphology of Platelet Aggregates Formed on Collagen Under Laminar Blood Flow,* Annals of Biomedical Engineering, Vol. 39, No. 2, February 2011 pp. 922–929.

[9] K. Jurk **,** B.E. Kehrel, *Pathophysiologie und Biochemie der Thrombozyten,* Internist 2010 · 51:1086–1094 DOI 10.1007/s00108-010-2595-4, Online publiziert: 12. August 2010 © Springer-Verlag 2010.

[10] N. A. Mody, M. R. King, *Platelet Adhesive Dynamics. Part II: High Shear-Induced Transient Aggregation via GPIba-vWF-GPIba Bridging,* Biophysical Journal Volume 95 September 2008 2556–2574.

[11] M. Takeyama, S. Kasuda,Y. Sakurai, M. Shima,T. Takeda, S. Omura, H. Naka, A.Yoshioka, *Factor VIII–Mediated Global Hemostasis in the Absence of von Willebrand Factor,* International Journal of Hematology, 2007.

[12] A. M. Müller, C. Skrzynski, G. Skipka, K.M. Müller, *Expression of von Willebrand Factor by Human Pulmonary Endothelial Cells in vivo*, Respiration 2002;69:526–533 DOI: 10.1159/000066471.

[13] Z. M. Ruggeri, *Platelet and von Willebrand factor interactions at the vessel wall*, © 2004 Schattauer GmbH.

[14] Z. M. Ruggeri, *The role of von Willebrand factor in thrombus formation*, Thromb Res. 2007; 120(Suppl 1): S5–S9. doi:10.1016/j.thromres.2007.03.011.

[15] H. Cheng, R. Yan, S. Li, Y. Yuan, J. Liu, C. Ruan, K. Dai ,*Shear-induced interaction of platelets with von Willebrand factor results in glycoprotein Ib a shedding, Am J Physiol Heart Circ Physiol* 297:H2128-H2135, 2009. First published 9 October 2009, doi:10.1152/ajpheart.00107.2009.

[16] R. Moroose, L. W. Hoyer, *VON WILLEBRAND FACTOR AND PLATELET FUNCTION*, Ann. Rev. Med. 1986.37: 157-63.

[17] P. M. Mannucci, *von Willebrand Factor : A Marker of Endothelial Damage*, Arterioscler Thromb Vasc Biol 1998;18;1359-1362.

[18] E. Hanson, K. Jood, S. Karlsonn, S. Nilsson, C. Blomstrand, C. Jern, *Plasma levels of von Willebrand factor in the etiologic subtypes of ischemic stroke. Journal of Thrombosis and Haemostasis*, (2011) 9: 275–281.

[19] G.L. Mendolicchio, Z. M. Ruggeri,*New perspectives on von Willebrand factor functions in hemostasis and thrombosis.*,Semin Hematol. 2005 Jan;42(1):5-14.

[20] P. André, P. Hainaud, C. B. dit Sollier, L. I. Garfinkel, J. P. Caen, L. O. Drouet, *Relative Involvement of GPIb/IX-vWF Axis and GPIIb/IIIa in Thrombus Growth at High Shear Rates in the Guinea Pig, Arteriosclerosis*, Thrombosis, and Vascular Biology. 1997;17:919-924.

[21] J. Evan Sadler, *Biochemistry and Genetics of Von Willebrand Factor*, Annu. Rev. Biochem. 1998. 67:395-424.

[22] S. A. Santoro, 1981, Thromb. Res. 21:689-91.

[23] L. G. Morton, B Griffin, DS Pepper, MJ. Barnes, 1983, Thromb. Res. 32:545-56.

[24] Z. M. Ruggeri, *Structure of von Willebrand factor and its function in platelet adhesion and thrombus formation*, Best Practice & Research Clinical Haematology, Vol.14, No.2, pp. 257-279,2001.

[25] H. Ohtani, N. Sasano, *Characterization of Microvasculature in the Stroma of Human Colorectal Carcinoma: An Immunoelectron Microscopic Study on Factor VIII/von Willebrand Factor*, J . Electron Microsc, Vol. 36, No. 4, 204-212, 1987.

[26] I. Singh, E. Themistou , L. Porcar, S. Neelamegham, *Fluid shear induces conformation change in human blood protein von Willebrand factor in solution.*,Biophys J. 2009 Mar 18;96(6):2313-20.

[27] A. Alexander Katz, M.F. Schneider, S.W. Schneider, A. Wixforth, R.R. Netz, *Shear-Flow-Induced Unfolding of Polymeric Globules*, PRL 97, 138101 (2006)

[28] S. W. Schneider, S. Nuschele, A. Wixforth, C. Gorzelanny, A. Alexander-Katz, R. R. Netz, and M. F. Schneider, Proc.Natl. Acad. Sci. U.S.A. **104**, 7899 (2007).

[29] Z. M. Ruggeri, J.N. Orje, R. Habermann, A. B. Federici, A. J. Reninger, *Activation-independent platelet adhesion and aggregation under elevated shear stress*, Blood First Edition Paper, June 13, 2006; DOI 10.1182/blood-2006-04-011551.

[30] R. Donadelli, J. N. Orje, C. Capoferri, G. Remuzzi, Z. M. Ruggeri, *Size regulation of von Willebrand factor-mediated platelet thrombi by ADAMTS-13 in flowing blood*, Blood, Nov 2005.

[31] W.E. Fauler, L. J. Fretto, *Electron microscopy of von Willebrand factor . In T.S. Zimmerman & Z.M. Ruggeri(eds) Coagulation and Bleeding Disorder.The Role of Factor VIII and von WIllebrand Factor,* pp 181-193. New York: Marcel Dekker, 1989.

[32] G. J. Tangelder, D. W. Slaaf,, T. Arts et. al. *Wall shear rate in arterioles in vivo: least estimates from platelet velocity profiles.* American Journal of Physiology 1988; 254: H1059-H1064.

[33] Z. M. Ruggeri, *Platelets in artherothrombosis,* Nat Med. 2002;8:1227-1234.

[34] B. Savage, F. Almus-Jacubs, Z. M. Ruggeri, *Specific synergy of multiple substrate-receptor interactions in platelet thrombus formation under flow.* Cell, 1998;94:657-666.

[35] K. S. Sakariassen, P. A. Bolhuis, J. J. Sigma, *Human blood platelet adhesion to artery subendothelium is mediated by factorVIII/von Willebrand factor bound to endothelium,* Nature, 1979;279:636-638.

[36] W.A. Hassenpflug, D. Angerhaus, U. Budde, T. Obser1, R. Schneppenheim, *Thrombotisch-thrombozytopenische Purpura im Kindesalter*, © 2004 Schattauer GmbH.

[37] P.J. Lenting and G. Rastegarlari, ADAMTS-13: double trouble for von Willebrand factor. Journal of Thrombosis and Haemostasis (2010), 8: 2775–2777.

[38] J. Rayes, M. J. Hollestelle, P. Legendre, I. Marx, P. G. de Groot, O. D. Christophe, P. J. Lenting, C. V. Denis, *Mutation and ADAMTS13-dependent modulation of disease severity in a mouse model for von Willebrand disease type 2B*, March 3, 2010, doi: 10.1182/blood-2009-11-254193.

[39] R. A. Claus, C. L. Bockmeyer, M. Sossdorf, W. Losche, *The Balance between von-Willebrand Factor and its Cleaving Protease ADAMTS13: Biomarker in Systemic Inflammation and Development of Organ Failure*, Current Molecular Medicine, Volume 10, Number 2, March 2010 , pp. 236-248(13).

[40] S. L. Haberichter, *VWF and FVIII: the origins of a great friendship*, Blood. 2009 March 26; 113(13): 2873–2874.

[41] D. G. Menter, L. Fitzgerald, J. T. Patton, L. V. McIntire, and G. L. Nicolson, Immunol. Cell Biol. **73**, 575 (1995).

[42] J. Pilch, R. Habermann, and B. Felding-Habermann, J. Biol. Chem. **277**, 21930 (2002)

[43] V. Terraube, R. Pendu, D.Baruch, M. F. B. G. Gebbink, D. Meyer, P. J. Lenting, C. V. Denis, *Increased metastatic potential of tumor cells in von Willebrand factor-deficient mice*, Journal of Thrombosis and Haemostasis, 4:519-526 (2005).

[44] M. A. Fallah, V. M. Myles, T. Krüger, K. Sritharan, A. Wixforth, F. Varnik, S. W. Schneider, M. F. Schneider, *Acoustic driven flow and lattice Boltzmann simulation to study cell adhesion in biofunctionalized µ-channels of with complex geometry,* BIOMICROFLUIDICS **4**, 024106 (2010).

[45] Z. M. Ruggerie, *The role of von Willebrand factor in thrombus formation*, Thromb Res. 2007; 120(Suppl 1): S5-S9. Doi:10.1016/j.thromres.2007.03.011.

[46] A. K. Chauhan, Janka Kisicka, Colin B. Lamb, W. Bergmeier, D. D. Wagner, *von Willebrand factor and factor VIII are independently required to form stable occlusive thrombi in injured veins*, Blood 2007 109: 2424-2429.

[47] A. Bernardo, C. Ball, N. Nolasco, H. Choi, J.L. Moake, J. F. Dong, *Platelets adhered to endothelial cell-bound ultra-large von Willebrand factor strings support leukocyte tethering and rolling under high shear stress*. J Throm Hemost 2005; 3: 562-70.

[48] José A. López, *Sticky business: von Willebrand factor in inflammation*, Blood 2006 108: 3627-doi: 10.1182/blood-2006-09-046474.

[49] P. Libby, Current Concepts of the Pathogenesis of the Acute Coronary Syndromes, Circulation 104 (3) (2001) 365–372.

[50] A. Jeremias, B. Sylvia, J. Bridges, A. J. Kirtane, B. Bigelow, D. S. Pinto, K. K. L. Ho, D. J. Cohen, L. A. Garcia, D. E. Cutlip, J. P. Carrozza, Stent Thrombosis After Successful Sirolimus-Eluting Stent Implantation, Circulation 109 (16) (2004) 1930–1932.

[51] S. Chien, Shear Dependence of Effective Cell Volume as a Determinant of Blood Viscosity, Science 168 (3934) (1970) 977–979.

[52] W. Hort, H. Lichti, H. Kalbfleisch, F. Köhler, H. Frenzel, U. Milzner-Schwarz, The size of human coronary arteries depending on the physiological and pathological growth of the heart, the age, the size of the supplying areas and the degree of coronary sclerosis, Virchows Archiv 397 (1) (1982) 37–59.

[53] H. Hikita, A. Sato, T. Nozato, T. Kawashima, Y. Takahashi, T. Kuwahara, A. Takahashi, Low coronary flow velocity and shear stress predict restenosis after sirolimus-eluting stent implantation, Scand. Cardiovasc. J. 43 (5) (2009) 298–303.

[54] F. Zernike, (1935): Das Phasenkontrastverfahren bei der mikroskopischen Beobachtung. Z. techn. Physik 16, 454-457.

[55] S. Chen, G. D. Doolen, *Lattice Boltzmann Method for Fluid Flows, Annu. Rev. Fluid Mech*. 30 (1998) 329–364.

[56] S. Succi, *The Lattice Boltzmann Equation for Fluid Dynamics and Beyond, Oxford University Press*, ISBN 978-0198503989, 2001.

[57] D. Raabe, *Overview of the lattice Boltzmann method for nano- and microscale fluid dynamics in materials science and engineering*, Modelling Simul. Mater Sci. Eng. 12 (2004) R13-R46.

[58] S. Chen, G. Doolen, K. G. Eggert, *Lattice-Boltzmann a versatile tool for multiphase Fluid Dynamics and other complicated flows*, Los Alamos Science, No.22, 1994.

[59] J. Latt, B. Chopard, O. Malaspinas, M. Deville, A. Michler, Straight Velocity Boundaries in the Lattice Boltzmann Method, Phys. Rev. E 77 (5) (2008) 056703–16.

[60] T. Krüger, M. A. Fallah, F. Varnik, M. F. Schneider, D. Raabe, A. Wixforth, *Inertia effects and stress accumulation in a constricted duct: A combined experimental and lattice Boltzmann study*, submitted to Phys. Rev. E. (2010).

[61] A.R. Pries, T.W. Secomb, H. Jacobs, M. Sperandio, K. Osterloh, P. Gaetgens, *Microvascular blood flow resistance: role of endothelial surface layer*, Am. J. Physiol., 1997. 273: pp. H2272-H2279.

[62] W. Reinke, P.C. Johnson, P. Gaetgens, *Effect of shear rate variation on apparent viscosity of human blood in tubes of 29 to 94 microns diameter*, Circ. Res. 1986;59;124-132.

[63] J.M. Ross, L.V. McIntire, J.L. Maoke, J.H. Rand, *Platelet adhesion and aggregation on human type VI collagen surfaces under physiological flow conditions*, Blood, 1995 85: 1826-1835.

[64] T.C. Nichols, D.A. Bellinger, T.A. Johnson, M.A. Lamb, T.R. Griggs, *Von Willebrand's disease prevents occlusive thrombosis in stenosed and injured porcine coronary arteries*, Circ. Res. 1986;59;15-26.

[65] F.S. Wouters, *The physics and biology of fluorescence microscopy in the life sciences*, Contemporary Physics, 47: 5, 239- 255(2006).

[66] K.R. Spring, *Fluorescence Microscopy*, Marcel Dekker Inc, NY(2003).

[67] Ya-Ping Wu; Hans H.F.I. van Breugel; Hanneke Lankhof; Robert J. Wise; Robert I. Handin; Philip G. de Groot; Jan J. Sixma,Platelet Adhesion to Multimeric and Dimeric VWF,Arteriosclerosis, Thrombosis, and Vascular Biology. 1996;16:611-620.

[68] Paula Yurkanis Bruice, *Organic Chemistry,*3rd edition, by Prentice-hall Inc., Pearson Education (2001), ISBN 0-13-017858-6.

[69] A.J. Vlot, S.J. Koppelman, B.N. Bourna, J.J. Sixma, *Factor VIII and von Willebrand factor,* Thromb Haemost 1998; 79:456-65.

[70] T. Matsui, K. Titani, T. Mizouchi, *Structures of the asparagine-linked oligosaccharidechains of human von Willebrand factor, Occurance of blood group A, B, and H(O) structures,* J Biol Chem 1992;267:8723-31.

[71] J.M. Sodetz, J.C. Paulson, P.A. McKee,*Carbohydrate composition and identification of blood groupA,B, and oligosaccharidestructures on human factor VIII/ von Willebrandfactor. J Biol Chem 1979; 254: 10754-60.*

[72] C. M. Millar , S.A. Brown, *Oligosaccharide structure of von WIllebrand factor and their potential role in von Willebrand desease*, Blood Reviews (2006) 20, 83-92.

[73] K. Titani, S. Kumar, K. Takio et al. *Amino acid sequence of human von WIllebrand factor,* Biochemistry (Mosc) 1986; 25:3171-84.

[74] A. L. Tarentino, and T.H. Plummer, Meth.Enzymology, **230**, 44-57 (1994).

[75] J. Q. Fan, and Y.C. Lee, J.Biol.Chem., 272, 27058 (1977).

[76] A. L.Tarentino et al., Biochemistry, **24**, 4665-4671(1985).

[77] J. H. Elder, and S. Alexander, Proc. Natl. Acad. Sci., USA, **79**, 4540-4544 (1982).

[78] E. M. Taga et al., Biochemistry, **23**, 815-822, (1984).

[79] R. B. Trimble, A.L. Tarentino, J. Biochem., 266, 1646-1651 (1991).

[80] E. A. Bayer et al., Appl. Biochem. Biotech., **53**, 1-9 (1995).

[81] F. Pera, I. Piper, Blut 41 (1980) 377.

[82] K. Beck, J. Bereitner- Hahn, Microscopica Acta 84 (1981) 153.

[83] A. Zickler, H. Engelhardt, E. Sackmann, *Dynamic reflection interference contrast (RIC-) microscopy: a new method to study surface excitations of cells and to measure membrane bending elastic moduli,* J. Physique 48 (1987) 2139-2151.

[84] W. I. Patzelt, Leitz-Mitt. Wiss. Tech. 7 (1979) 141.

[85] C. H. Back, J. R. Radbill, D.W. Crawford, *Analysis of pulsatile viscous blood flow through diseased coronary arteries of man*, Journal of Biomechanics 1977; 10: 339-353.

[86] E. Evans, K. Ritchie, R. Merkel, *Sensitive Force Technique to Probe Molecular Adhesion and Structural Linkages at Biological Interfaces*, Biophysical Journal, Volume 68, June 1995, 2580-2587.

[87] R. Merkel, P. Nassoy, A. Leung, K. Ritchie, E. Evans, *Energy landscapes of receptor±ligand bonds explored with dynamic force spectroscopy*, Nature, Vol 397, 7 January, 1999.

[88] E. Evans, V. Heinrich, A. Leung, K. Kinoshita , *Nano- to Microscale Dynamics of P-Selectin Detachment from Leukocyte Interfaces. I. Membrane Separation from the Cytoskeleton*, Biophysical Journal, Volume 88, March 2005, 2288–2298.

[89] K. Kinoshita, A. Leung, S. Simon, E. Evans*, Long-Lived, High-Strength States of ICAM-1 Bonds to b2 Integrin, II:Lifetimes of LFA-1 Bonds Under Force in Leukocyte Signaling,* Biophysical Journal, Volume 98, April 2010, 1467–1475.

[90] H. Al-Mondhiry, Am. J. Hematol. 16, 193 (1984).

[91] A. Lazo-Langner, G. D. Goss, J. N. Spaans, and M. A. Rodger, J. Thromb. Haemostasis **5**, 729 (2007).

[92] C. P. W. Klerk, S. M. Smorenburg, H.-M. Otten, A. W. A. Lensing, M. H. Prins, F. Piovella, P. Prandoni, M. M. E. M. Bos, D. J. Richel, G. van Tienhoven, and H. R. Büller, J. Clin. Oncol. 23, 2130 (2005).

[93] P. Prandoni, A. Falanga, and A. Piccioli, Lancet Oncol. **6**, 401(2005).

[94] N. Lion, T. C. Rohner, L. Dayon, I. L. Arnaud, E. Damoc, N. Youhnovski, W. Zhi-Yong, C. Roussel, J. Josserand, H. Jensen, J. S. Rossier, M. Przybylski, and H. H. Girault, Electrophoresis **24**, 3533 (2003).

[95] E. M. Purcell, Am. J. Phys. **45**, 3 (1977).

[96] A. van den Berg, *Lab-on-Chips for Cellomics, Micro and Nanotechnologies for Life Science,* Springer, New York, (2005).

[97] A. Wixforth, C. Strobl, C. Gauer, A. Toegl, J. Scriba, and Z. Guttenberg, Anal. Bioanal. Chem. **379**, 982 (2004).

[98] Z. Guttenberg, H. Muller, H. Habermuller, A. Geisbauer, J. Pipper, J. Felbel, M. Kielpinski, J. Scriba, and A. Wixforth, Lab Chip **5**, 308(2005).

[99] Z. Guttenberg, A. Rathgeber, S. Keller, J. O. Radler, A. Wixforth, M. Kostur, M. Schindler, and P. Talkner, Phys. Rev. E **70**, 056311 (2004).

[100] K. Sritharan, C. J. Strobl, M. F. Schneider, A. Wixforth, and Z. Guttenberg, Appl. Phys. Lett. **88**, 054102 (2006).

[101] W. Nyborg, *Acoustic Streaming* _Academic, New York, (1965).

[102] M. F. Schneider, Z. Guttenberg, S. W. Schneider, K. Sritharan, V. M. Myles, U. Pamukci, and A. Wixforth, ChemPhysChem **9**, 641 (2009).

[103] A. Wixforth, J. Assoc. Lab. Autom. **11**, 399 (2006).

[104] L. Y. Yeo and J. R. Friend, Biomicrofluidics **3**, 012002 (2009).

[105] P. Brunet, M. Baudoin, O. Bou Matar, and F. Zoueshtiagh, Droplets Displacement and Oscillations Induced by Ultrasonic Surface Acoustic Waves: A Quantitative Study, 3 November 2009.

[106] S. Girardo, M. Cecchini, F. Beltram, R. Cingolani, and D. Pisignano, Lab Chip **8**, 1557 (2008).

[107] M. Cecchini, S. Girardo, D. Pisignano, R. Cingolani, and F. Beltram, Appl. Phys. Lett. **92**, 104103 (2008).

[108] A. Barg, R. Ossig, T. Goerge, M. F. Schneider, H. Schillers, H. Oberleithner, and S. W. Schneider, "Soluble plasmaderived von Willebrand factor assembles to a hemostatically active filamentous network," Thromb. Haemostasis 97, 514(2007).

[109] T. Goerge, F. Kleineruschkamp, A. Barg, E. M. Schnaeker, V. Huck, M. F. Schneider, M. Steinhoff, and S. W. Schneider, Thromb. Haemostasis **98**, 283 (2007).

[110] D. G. Menter, L. Fitzgerald, J. T. Patton, L. V. McIntire, and G. L. Nicolson, Immunol. Cell Biol. 73, 575 (1995).

[111] J. Pilch, R. Habermann, and B. Felding-Habermann, J. Biol. Chem. 277, 21930 (2002).

Acknowledgment

Here, I would like to express my sincere gratitude to all who helped me with completion of this work. Especially, my colleagues and friends at chair for Experimental Physics I, at Augsburg University; and at Prof. S. W. Schneider's Experimental Dermatology section of University of Heidelberg at Mannheim, without whom this work could have not been accomplished.

I would like to especially thank those who have directly helped me during the scientific studies performed for this dissertation:

Prof. Dr. Achim Wixforth

For providing me the possibility of working in his lovely group during both my Master's and Ph.D studies; during which he has supported me generously and provided me with the best supervision one can ever wish. Not to mention his never ending blessings during the both professional and private hard times.

Prof. Dr. Matthias F. Schneider

Not only for giving me the chance to work in his biological physics group, and giving me enough freedom to develop in a field in which i was a stranger before, but also for his extraordinary scientific supervision, and his unconditional support and patience during the hard times.

Univ. Prof. Dr. Stefan W. Schneider

Not only for giving to a unique opportunity to work in his group during my Ph.D studies, and his valuable support, but also for supervision and evaluation of my work. The time that i spent in his group has been one of the bests i have ever had.

Prof. Dr. B. Stritzker

For kindly accepting to be a member of the examination board.

Priv.-Doz. I. Goychuk

For kindly accepting to be a member of the examination board.

Dr. Volker Huck

For the very fruitful discussions and experiments we have performed in Mannheim. For the valuable medical knowledge i learnt from him, and for the friendship that has developed during this time.

Dr. Verena Niemeyer

For the extremely fruitful cooperation and for making Mannheim feel like a second home for me.

Andreas Hartmann, Christoph Westerhausen, Jennifer Angerer

For their always friendly attitude during many discussions and studies we have performed together, and for helping me with correction of this dissertation.

Dr. Stefan Nuschele

For many extremely pleasant discussions and the friendship i am really proud of.

Dr. Andreas Hörner

For his numerous friendly advices during the years i have been working at the chair for experimental physics I.

My Family

Banu and Javad, showing appreciation and gratitude here at the end of this work is the only thing i can do for all the things you have done for me and all the love you have given me. Thanks a lot. Arash, i would like to thank you for the great brother you are for me, not to mention the wisdom that you have deep within.

Inertia effects and stress accumulation in a constricted duct: A combined experimental and lattice Boltzmann study

T. Krüger, M. A. Fallah, F. Varnik, M. F. Schneider, D. Raabe, A. Wixforth

Abstract

We experimentally and numerically investigate the flow of a Newtonian fluid through a constricted geometry for Reynolds numbers in the range $[0.1 - 100]$. The major aim is to study the non-linear inertia effects at larger Reynolds numbers on the shear stress evolution in the fluid. This is of particular importance for blood flow since some biophysical processes in blood are sensitive to shear stress, e.g., the initialization of blood clotting. We employ the lattice Boltzmann method for the computer simulations. The result of the simulations is that the peak value of shear stress in the constriction grows disproportionally fast with the Reynolds number which leads to a non-linear shear stress accumulation. As a consequence, the combination of constricted blood vessel geometries and large Reynolds numbers may increase the risk of undesired blood clotting.

1. Introduction

There is growing evidence that blood clotting is a dynamic process in which fluid shear stress plays an important role [1]. The protein von Willebrand factor (VWF) shows a conformation change when the ambient shear rate reached values of about $5000\,\mathrm{s}^{-1}$. It is also known that arterial plaque and stents favor the emergence of blood clots [2, 3]. Besides such biochemical reasons, one possible physical cause for clotting may be the detrimental influence of large local shear stresses in the vicinity of constrictions. Physically, the flow boundary conditions are modified by the presence of obstacles. Depending on the Reynolds number, obstacles can have a significant impact on the flow properties, even beyond the location of the obstacle. A prominent example is the Kármán vortex street which is a repeating pattern of swirling vortices occuring in the laminar flow regime behind a bluff obstacle.

The motivation for this article is to study inertia effects on the shear stress in fluid flows perturbed by a simple obstacle and their basic implications for hemorheology. In our present investigation, we numerically model and experimentally measure the flow of a Newtonian fluid through a duct with a simple constriction at different Reynolds numbers in the laminar regime. We emphasize that the direct comparison of experiments and simulations is essential. Although the accuracy and applicability of the employed lattice Boltzmann method (LBM) has been proven various times [4–7], the numerical results should be supported and verified by experiments.

One of the simplest symmetric, yet non-trivial, flow geometries is a duct with a bottleneck-like constriction as sketched in Fig. 1. Using this obstacle, we study fundamental properties of the fluid flow at different Reynolds numbers between 0.1 and 100. The particular design of the constriction has been chosen for convenience since this geometry is easily produced by milling techniques in the experiments.

Since we are interested in the basic physical effects of inertia in a constricted geometry, we simplify the problem as much as possible. In particular, the fluid is assumed to be steady, and we use a Newtonian fluid (water in the experiments). For this reason, the Womersley number is zero, and the Reynolds number is the only relevant physical parameter. The assumption of a Newtonian fluid limits the validity of the simulations and experiments to larger blood vessels because at those scales the individual motion of the red blood cells can be neglected and the viscosity is virtually independent of the shear rate [8]. However, this is no severe restriction since we are mainly interested in the blood flow in human coronary arteries with average diameters of 3–4 mm [9] which is 1000 times the radius of a red blood cell. Typical Reynolds numbers in coronary arteries are of order 100 [10].

Due to the non-linear character of the Navier-Stokes equations, at large Reynolds numbers, abrupt changes in cross-section may lead to spatial variations of velocity and shear stress which cannot be fully understood from dimensional considerations or the Stokes equations. For this reason, we study the impact of a bottleneck-like constriction on the local properties of the fluid as a function of the Reynols number. We are particularly interested in the spatial asymmetry and the magnitude of the shear stress. In order to emphasize the nonlinear effects arising at high Reynolds numbers, we vary the Reynolds number over three order of magnitude, $[0.1 - 100]$, thus covering both the fully viscous and inertial regimes. At large Reynolds numbers, the spatial flow velocity and shear stress fields are asymmetric, even in a symmetric geometry. The cause is the convective term in the Navier-Stokes equations. This asymmetry introduces a distinction of the pre- and post-constriction regions. Moreover, one can observe that the peak values of the shear stress close to the constriction increase faster than linearly with the Reynolds number, showing the significance of the inertia effects.

The article is organized as follows. The basic hydrodynamic concepts are presented in Sec. 2, followed by a detailed description of the experimental and numerical setup in Sec. 3. The observations and results are presented and discussed in Sec. 4. Finally, the conclusions are pointed out in Sec. 5.

2. Theory

The full Navier-Stokes equations in the absence of a body force density read

$$\rho \left(\frac{\partial \boldsymbol{u}}{\partial t} + \boldsymbol{u} \cdot \nabla \boldsymbol{u} \right) = -\nabla p + \eta \Delta \boldsymbol{u} \tag{1}$$

where $\boldsymbol{u}$ denotes the velocity, ρ the density, p the pressure, and η the viscosity of the fluid. Introducing the deviatoric shear stress tensor with components

$$\sigma_{\alpha\beta} = \eta \left(\partial_\alpha u_\beta + \partial_\beta u_\alpha \right), \tag{2}$$

2
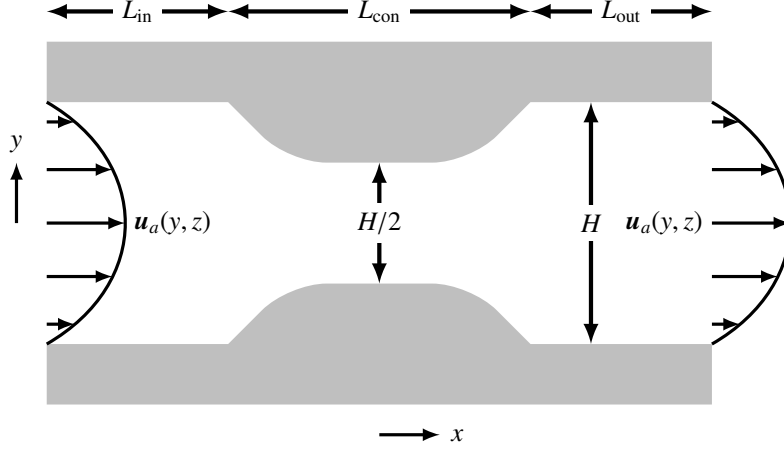
Figure 1: A 2D projection of the constriction geometry used both in the experiments and simulations. The fluid enters the geometry from the left. Numerically, the inlet and outlet velocities $\boldsymbol{u}_a(y,z)$ are taken from the analytic solution of the steady duct flow problem. The origin of the coordinate system is at the center of the constriction. The initial width (along y-axis) and height (along z-axis) are H, and the constricted width is $H/2$. The total length of the constriction is $L_{\text{con}} = 5H/4$, and the initial inclination of the constriction walls is $45°$. The rounded corners with radius $r = H/4$ are due to the milling technique used for fabricating the duct. The numerical values of the inlet and outlet duct lengths L_{in} and L_{out} are chosen in such a way that the flow can fully develop.

the viscous term in Eq. (1) can be written in the form $\eta \Delta \boldsymbol{u} = \nabla \cdot \boldsymbol{\sigma}$. The deviatoric shear stress tensor $\boldsymbol{\sigma}$ (from now on only called shear stress) is part of the total momentum flux tensor of the fluid,

$$M_{\alpha\beta} = p\,\delta_{\alpha\beta} + \rho\,u_\alpha u_\beta - \sigma_{\alpha\beta}. \tag{3}$$

Eq. (1) can then be written in the compact form $\rho\,\partial_t u_\alpha = -\partial_\beta M_{\alpha\beta}$. The first term on the right-hand-side of Eq. (3) is the isotropic pressure contribution, the second term denotes momentum transport due to convection (mass transport) which is only important at large Reynolds numbers.

The shear stress $\boldsymbol{\sigma}$ describes the momentum diffusion related to the viscosity of the fluid which is the central quantity when it comes to mechanically triggered blood clotting [1]. It is a second order tensor with six independent components (in this case only five because it is traceless due to the incompressibility of the fluid). Since the tensor is symmetric, it has always three real eigenvalues $\sigma_3 \leq \sigma_2 \leq \sigma_1$. For an incompressible fluid, the eigenvalues obey $\text{Tr}\,\boldsymbol{\sigma} = \sigma_1 + \sigma_2 + \sigma_3 = 0$. In the literature about applications of sheared fluids, usually an equivalent shear stress scalar σ_{eff} is provided, and the tensor properties are lost. Assuming that the dynamics of VWF is not sensitive to the tensor components $\sigma_{\alpha\beta}$ but only to an effective scalar value, it arises the need for an appropriate definition. There are different possibilities to construct an effective scalar from the full tensor. The von Mises stress is

$$\sigma_{\text{vM}} := \sqrt{\frac{1}{2} \sum_{\alpha,\beta} \sigma_{\alpha\beta}\sigma_{\alpha\beta}} = \sqrt{\frac{1}{2}\left(\sigma_1^2 + \sigma_2^2 + \sigma_3^2\right)} = \sqrt{\sigma_1^2 + \sigma_3^2 + \sigma_1\sigma_3}. \tag{4}$$

3

The last identity in Eq. (4) is valid if the fluid is incompressible, $\text{Tr}\,\boldsymbol{\sigma} = 0$. The von Mises stress plays an important role in the analysis of material failure in material sciences, but it can also be applied to fluids. Given the shear stress tensor at a specific point, one can also ask in which direction $\boldsymbol{n}$ the maximum shear component σ_{max} of the tensor can be found. From a Mohr analysis one finds

$$\sigma_{\text{max}} := \frac{\sigma_1 - \sigma_3}{2}. \tag{5}$$

The definitions in Eqs. (4) and (5) and further comments can be found in monographs about elasticity, e.g., in [11]. For an incompressible fluid, in general $\sigma_{\text{vM}} \geq \sigma_{\text{max}}$ holds, but one can show that if the eigenvalue σ_2 vanishes, $\sigma_{\text{vM}} = \sigma_{\text{max}} = \sigma_1$ since then $\sigma_3 = -\sigma_1$. One can further show that the maximum deviation between both shear stress scalars is about 15%. For this reason, we drop a separate discussion of σ_{vM} and σ_{max} and restrict ourselves to the von Mises stress. As a compact notation for the shear stress magnitude, we define

$$\sigma = \|\boldsymbol{\sigma}\| := \sigma_{\text{vM}}, \tag{6}$$

cf. Eq. (4). We emphasize that the concept of shear stress is applicable to material sciences and hydrodynamics, i.e., to solids and fluids. The definition for the velocity magnitude is the usual one,

$$u = \|\boldsymbol{u}\| := \sqrt{\sum_{\alpha} u_{\alpha} u_{\alpha}}. \tag{7}$$

In the present article, the duct Reynolds number is defined as

$$\text{Re} = \frac{\rho H \bar{u}}{\eta}. \tag{8}$$

H is the height and the width of the square duct, cf. Fig. 1. The velocity scale $\bar{u}$ will be formally introduced in Eq. (12). It is the average velocity on the inlet cross-section with area $A = H^2$ and can easily be obtained in experiments by $\dot{V} = A\bar{u}$ if the volume flux $\dot{V}$ of the fluid is known.

In the limit of small Reynolds numbers and a stationary situation, the left-hand-side of Eq. (1) is negligible, and one can write the Stokes equation

$$0 = -\nabla p + \eta \Delta \boldsymbol{u}. \tag{9}$$

Note that Eq. (9) is invariant under the transformation ($\boldsymbol{u} \to -\boldsymbol{u}, \nabla p \to -\nabla p$), whereas Eq. (1) is not. As a consequence, the stationary velocity field for $\text{Re} = 0$ looks the same (up to its sign), when the flow of the fluid through a fixed geometry is reversed (also the signs of possible velocity boundary conditions have to be reversed). In case of a point-symmetric geometry (invariant under the transformation $\boldsymbol{x} \to -\boldsymbol{x}$), as we use it here, cf. Fig. 1, it is easy to see that $\boldsymbol{u}(\boldsymbol{x}) = \boldsymbol{u}(-\boldsymbol{x})$ must hold if $\text{Re} = 0$. The shear stress obeys $\boldsymbol{\sigma}(\boldsymbol{x}) = -\boldsymbol{\sigma}(-\boldsymbol{x})$ since the spatial derivative enters its definition, Eq. (2), and leads to an additional minus sign. For a finite Reynolds number, the presence of the convective term $\boldsymbol{u} \cdot \nabla \boldsymbol{u}$ breaks the symmetry, and the direction of the flow can

be recognized by its inertia effects and the shape of the streamlines. The Kármán vortex street is a demonstrative example for this statement: The vortexes appear only downstream.

In this article, we study the asymmetry introduced by finite inertia as a function of the Reynolds number. Additionally, the effects of inertia on the shear stress distribution is analyzed. For this reason, we introduce an index of distortion for the velocity and the shear stress. Knowing the analytic solutions $\boldsymbol{u}_a(y, z)$ and $\boldsymbol{\sigma}_a(y, z)$ for a fully developed flow in the duct [12–14] and taking the actual velocity $\boldsymbol{u}_d(y, z)$ and shear stress $\boldsymbol{\sigma}_d(y, z)$ at a given cross-section at axial distance d from the constriction, we define

$$I_u(d) = \frac{1}{A\bar{u}} \sum_{y,z} \|\boldsymbol{u}_a(y, z) - \boldsymbol{u}_d(y, z)\|, \tag{10}$$

$$I_\sigma(d) = \frac{1}{A\bar{\sigma}} \sum_{y,z} \|\boldsymbol{\sigma}_a(y, z) - \boldsymbol{\sigma}_d(y, z)\| \tag{11}$$

where the norm $\|\cdot\|$ for the shear stress and the velocity has been defined in Eqs. (6) and (7). The quantities

$$\bar{u} = \frac{1}{A} \sum_{y,z} \|\boldsymbol{u}_a(y, z)\|, \tag{12}$$

$$\bar{\sigma} = \frac{1}{A} \sum_{y,z} \|\boldsymbol{\sigma}_a(y, z)\| \tag{13}$$

are the velocity and shear stress scales, defined as the averages on the inlet cross-section. They obey $\bar{u} \propto \mathrm{Re}$ and $\bar{\sigma} \propto \mathrm{Re}$ and are control quantities which the numerical results will be related to.

In Stokes flow, $\mathrm{Re} = 0$, the fluid velocity and shear stress distributions look the same before and behind the constriction (up to signs). For this reason, Eqs. (10) and (11) are invariant if the coordinate system is transformed according to $\boldsymbol{x} \to -\boldsymbol{x}$. Thus, the indexes of distortion I_u and I_σ do not change when the coordinate system is transformed. At finite Reynolds number, however, the symmetry is broken, and inlet and outlet flow profiles differ. Thus, we expect that $I_u(d) \neq I_u(-d)$ and $I_\sigma(d) \neq I_\sigma(-d)$ when $\mathrm{Re} \neq 0$. As we will show in Section 4, the slopes of $I_u(d)$ and $I_\sigma(d)$ are well captured by a simple decaying exponential. For this reason, it is natural to define a range of decay λ for each exponential. It is given by the distance from the constriction after which the exponential decays to $\exp(-1)$ of its initial value. In order to distinguish the ranges of decay for the velocity and the shear stress, we denote both quantities λ_u and λ_σ, respectively. This way, the indexes of distortion can be approximated by

$$I_u(d) = I_u(0) \exp(-d/\lambda_u), \tag{14}$$
$$I_\sigma(d) = I_\sigma(0) \exp(-d/\lambda_\sigma). \tag{15}$$

Related to the definition of λ_u is the problem of the flow development length L_D in a 2D channel or a 3D pipe. It has been thoroughly discussed in the literature analytically, numerically, and experimentally due to its important implications in engineering [15–17]. The common approach is to impose a constant velocity profile at the inlet of a

5

Re	L_D/H
0.1	0.6
1	0.6
10	0.9
20	1.4
45	2.7
100	5.8

Table 1: Development lengths L_D for given Reynolds numbers according to Eq. (16) with $D = H$. The Reynolds numbers are those taken for the simulations. In the experiments, the Reynolds numbers 0.1, 1, 10, and 100 have been investigated.

pipe with circular cross-section and diameter D and find the axial distance L_D from the inlet at which the central velocity has reached 99% of its fully developed value. The parameter L_D/D is a function of the Reynolds number. Durst et al. [17] have proposed the relation

$$\frac{L_D}{D} = \left(0.619^{1.6} + (0.0567\,\text{Re})^{1.6}\right)^{1/1.6} \tag{16}$$

for a Newtonian fluid in a pipe and $\text{Re} = \rho D \bar{u}/\eta$. This equation is valid for all Reynolds numbers as long as the flow is laminar, and the numerical error is reported to be $< 3\%$. In the present simulations, there is a slightly different situation: The geometry is a duct with quadratic cross-section, and the velocity profile at the constriction is not constant. However, it has turned out that Eq. (16) is a sufficient approximation for the presented problem. The development lengths obtained from Eq. (16) and using H instead of D are shown in Tab. 1. Those values act as a guideline for the experiments and simulations to assure the duct before and behind the constriction is sufficiently long.

3. Setup

The employed geometry is a square duct (width = height = H) in the yz-plane. A 2D projection is shown in Fig. 1. The flow enters at the inlet in x-direction. A constriction of total length $L_{\text{con}} = 5H/4$ is located halfway between the inlet and the outlet. In the constriction, the width of the duct (along the y-axis) is decreased, but the height (along the z-axis) is not changed. The constricted width is $H/2$, leading to an average flux velocity two times larger than in the main duct. Due to the milling technique employed for the experiments, the inner edges of the constriction are rounded with radius $r = H/4$. The origin of the coordinate system is always located at the center of the constriction.

3.1. Experiments

The experimental setup consists of the duct, cf. Fig. 1, a syringe pump and tubes for connecting the pump to the duct. The height of the duct is $H = 2\,\text{mm}$. The flux is driven at a desired rate by application of a syringe pump (NE-1000, New Era Pump Systems, Inc., NY, USA). Connection between the pump and the duct succeeds over tubes connecting the syringe needle to the inlet. The duct itself consists of two parts.

Re	$\bar{u}\,[\mathrm{mm\,s^{-1}}]$	$\dot{V}\,[\mathrm{ml\,min^{-1}}]$
0.1	0.05	0.012
1	0.5	0.12
10	5	1.2
100	50	12

Table 2: Experimental volumetric flow rates $\dot{V}$ for achieving the desired Reynolds numbers and the average inlet velocities $\bar{u}$. The length scale is $H = 2\,\mathrm{mm}$, and the fluid properties are $\rho = 1000\,\mathrm{kg\,m^{-3}}$ and $\eta = 10^{-3}\,\mathrm{Pa\,s}$.

Re	τ	$\hat{u}$	$L_{\mathrm{in}}, L_{\mathrm{out}}$
0.1	0.9	0.000349	100
1	0.9	0.00349	100
10	0.8	0.0262	160
20	0.7	0.0349	160
45	0.6	0.0393	240
100	0.54	0.0349	480

Table 3: Collection of the relevant simulation parameters. The diameter of the unconstricted duct in all the simulations is $H = 80$ lattice nodes. $\hat{u}$ is the lattice velocity at the center of the inlet and outlet cross-sections. It can be shown that for the current geometry the average velocity is $\bar{u} \approx 0.48\hat{u}$ [14]. τ is the relaxation time used for the BGK lattice Boltzmann method. L_{in} and L_{out} are the numerical values for the duct inlet and outlet lengths.

The upper part is made of polydimethylsiloxane (PDMS), casted into a mould produced by milling. This part is then converted to a completely closed duct by being attached to a microscope glass slide which plays the role of the lower deck of the duct. Inlet and outlet are punched into the duct before attachment of the PDMS to the glass slide. Attachment occurs by plasma oxidation of the PDMS and the glass slide.

The local fluid velocity in the duct is measured by tracking polystyrene beads (Polysciences, Inc., Warrington, PA, USA) with a diameter of $10\,\mu\mathrm{m}$ which are suspended in the carrier fluid (water, density $\rho = 1000\,\mathrm{kg\,m^{-3}}$ and viscosity $\eta = 10^{-3}\,\mathrm{Pa\,s}$ at 20°C).

The experiments are conducted on a Zeiss Axiovert 200 inverted microscope typically using a 2.5x objective. The velocities of the beads are observed at a height of 1 mm over the bottom deck of the duct (i.e., in the middle between bottom and top). For each Reynolds number, a video of the flux inside the duct is made using an ultrafast camera (Fastcam, Photron, CA, USA). The videos are analyzed by the software 'Image J' afterwards.

Since the fluid properties and the spatial scale H are fixed, the Reynolds number, Eq. (8), can only be changed by choosing a mean velocity of the fluid. Four different Reynolds numbers have been investigated experimentally. The corresponding volume rates are shown in Tab. 2.

3.2. Simulations

We have employed the lattice Boltzmann method (LBM) for the numerical investigation of the problem. In particular, a D3Q19 BGK model has been used [18]. There

exist excellent introductory articles [19–21], monographs [5, 6] and reviews [4, 22] about the LBM.

In order to capture the physical boundary conditions of both the constriction-fluid surface (no slip) and the inlet and outlet cross-sections of the simulation box (fully developed flow), we employ the standard LBM bounce-back boundary condition [21] for the former and velocity boundary conditions for the latter case. At the inlet and outlet of the computational box, a fully developed velocity profile $\boldsymbol{u}_a(y, z)$ is imposed. The velocity boundary condition used has been proposed by Latt et al. [13]. We have chosen this approach due to its simple and straightforward implementation in three-dimensional LBM simulations. The analytic form of the stationary, fully developed flow profile for a rectangular duct is discussed in [12–14].

We compute the pressure p, velocity vector $\boldsymbol{u}$, and the full shear stress tensor $\boldsymbol{\sigma}$ in the entire numerical grid. From this data, we can calculate the effects of inertia on the spatial velocity and shear stress distributions. We trace the maximum values of velocity and shear stress. Furthermore, we compute the indexes of distortion I_u and I_σ, Eqs. (10) and (11), as function of the axial distance d from the constriction, both before and behind the constriction.

In the simulations, H corresponds to 80 lattice nodes to ensure a sufficiently high spatial resolution. The simulations are terminated when the relative change of velocity

$$\frac{\delta u}{\bar{u}} = \frac{1}{N\bar{u}} \sqrt{\sum_{x,y,z} (\boldsymbol{u}_{\text{new}}(x, y, z) - \boldsymbol{u}_{\text{old}}(x, y, z))^2} \tag{17}$$

becomes smaller than 10^{-10} between two successive time steps where N is the total number of lattice nodes. This condition guarantees that the flow is stationary. In order to take into account the development length L_D of a non-developed flow, Eq. (16), we allow the flow to relax towards inlet and outlet by extending the duct geometry correspondingly. If the inlet or outlet is too short, unphysical hydrodynamic interactions with the boundaries, such as reflections, arise. For convenience, the numerical inlet and outlet lengths are always identical, $L_{\text{in}} = L_{\text{out}}$. The relavant simulation parameters are given in Tab. 3.

4. Results
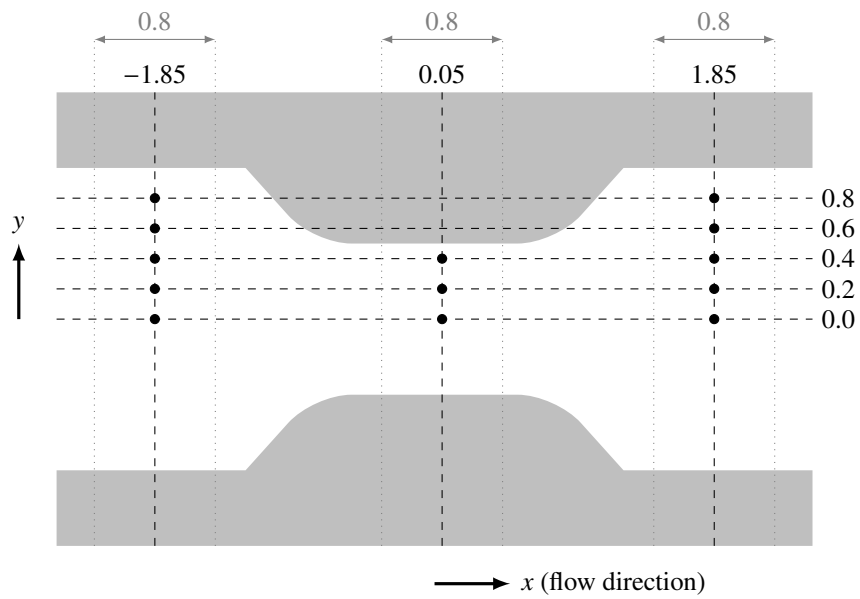
Figure 2: Locations of the velocity measurements in the experiments (black dots). All positions and distances are given in units of mm. The origin is located at the center of the constriction. The flow enters from the left. The velocities have been measured at three positions along the x-axis ($x = -1.85$ mm, 0.05 mm, and 1.85 mm) and five positions along the y-axis ($y = 0$ to 0.8 mm in steps of 0.2 mm). In the constriction, only three data points have been taken ($y = 0$, 0.2 mm, and 0.4 mm). In order to compute the velocities, the times of travel of the tracer particles between the dotted lines have been measured ($\Delta x = 0.8$ mm and $\Delta y = 0$, respectively). The velocity data is shown in Tab. 4.

| position		Re = 0.1			Re = 1			Re = 10			Re = 100		
x[mm]	y[mm]	exp	sim	dev	exp	sim	dev	exp	sim	dev	exp	sim	dev
−1.85	0.0	0.092	0.109	16%	1.2	1.08	11%	9.8	10.6	8%	87	106	18%
−1.85	0.2	0.088	0.104	15%	1.1	1.03	7%	9.4	10.2	8%	85	101	16%
−1.85	0.4	0.076	0.0894	15%	0.98	0.891	10%	8.9	8.85	1%	76	88.7	14%
−1.85	0.6	0.054	0.0669	19%	0.81	0.669	21%	6.0	6.69	10%	63	67.1	6%
−1.85	0.8	0.038	0.0370	3%	0.50	0.371	35%	4.1	3.70	11%	43	35.8	20%
0.05	0.0	0.17	0.199	15%	1.9	1.99	5%	27	19.4	39%	151	161	6%
0.05	0.2	0.14	0.165	15%	1.5	1.65	9%	25	16.1	55%	144	150	4%
0.05	0.4	0.049	0.0662	26%	0.93	0.662	40%	9.2	6.55	40%	103	71.1	45%
1.85	0.0	0.085	0.109	22%	1.0	1.10	9%	14	12.8	9%	144	155	7%
1.85	0.2	0.072	0.104	31%	0.92	1.05	12%	10	11.9	16%	140	140	0%
1.85	0.4	0.071	0.0894	21%	0.42	0.897	53%	6.2	9.58	35%	103	95.2	8%
1.85	0.6	0.065	0.0669	3%	0.33	0.669	51%	5.8	6.57	12%	32	42.8	25%
1.85	0.8	0.045	0.0370	22%	0.22	0.369	40%	4.8	3.35	43%	21	8.46	148%

Table 4: Measured and simulated velocities in the constriction at selected positions (x, y) midway between the bottom and top walls, cf. Fig. 2. All velocities are given in units of $\mathrm{mm\,s^{-1}}$. The deviations $|u_{\mathrm{exp}} - u_{\mathrm{sim}}|/u_{\mathrm{sim}}$ are also shown.

Re	λ_u/H		λ_σ/H	
	inlet	outlet	inlet	outlet
0.1	0.18	0.19	0.20	0.20
1	0.18	0.19	0.19	0.21
10	0.16	0.29	0.18	0.30
20	0.16	0.45	0.16	0.45
45	0.16	0.80	0.18	0.79
100	0.18	1.39	0.18	1.36

Table 5: Ranges of decay λ_u/H and λ_σ/H towards the inlet and outlet extracted from the simulation data. The ranges are defined as the distances from the constriction at which the indexes of distortion I_u and I_σ drop to $\exp(-1)$ of their value directly at the constriction. The outlet data is also illustrated in Fig. 6.

In Fig. 2, the locations of the velocity measurements in the experiments are presented. The velocities have been estimated by measuring the time of travel of representative tracer particles (cf. Sec. 3.1) between two positions along the x-axis ($\Delta x \approx 0.8$ mm and $\Delta y \approx 0$). The resultant velocity is assumed to be the velocity midway between the two points. The experimental data is shown together with the corresponding velocities from the simulations and the relative deviations $|u_{\text{exp}} - u_{\text{sim}}|/u_{\text{sim}}$ in Tab. 4. Some streamlines found in the experiments and simulations are visualized in Figs. 3 and 4. The experimental and simulated results at Reynolds numbers 1 and 100 are shown in Fig. 3. In Fig. 4, the simulated flow fields for the Reynolds numbers 0.1 and 100 are directly compared.

The experiments have been carried out with great care. However, as can be seen from Tab. 4, the quantitative comparison of the experimental and simulation velocity data reveals some deviations. The major reason is that the velocities cannot be measured locally in the experiments. Instead, the motion of the tracer beads is followed over a finite distance of $0.4H$ (0.8 mm), and the velocity at the middle of this line is assumed to be the average velocity, cf. Fig. 2. This approach can only be accurate if the length over which the particles are observed is small compared to the typical length for the change of the velocity field. This characteristic length is of order $H/4$ which is half the width of the duct inside the constriction. Consequently, there is an intrinsic uncertainty in the velocity measurement. The particles do not always move on straight lines which can be recognized from the shape of the streamlines, cf. Fig. 3. This makes it hard to achieve a good estimate for the local velocities even when the time resolution of the measurements is high. Especially close to the walls ($y = 0.8$ mm before and behind and $y = 0.4$ mm inside the constriction), the deviations are expected to be larger. The reason is that the velocity gradient is maximum in the vicinity of the walls. If the position of the tracer beads is slightly shifted along the y-axis, this will lead to a large uncertainty in the velocity measurement. This trend can clearly be recognized in Tab. 4. An additional, yet minor, reason for the deviations is that the tracer particles do not necessarily move exactly in the plane midway between the bottom and top walls ($z = 0$). However, it is encouraging to see that the qualitative shape of the experimental streamlines are excellently recovered by the computer simulations. Especially the shape of the vortexes at Re = 100, cf. Fig. 3(b), is correctly reproduced. Taking
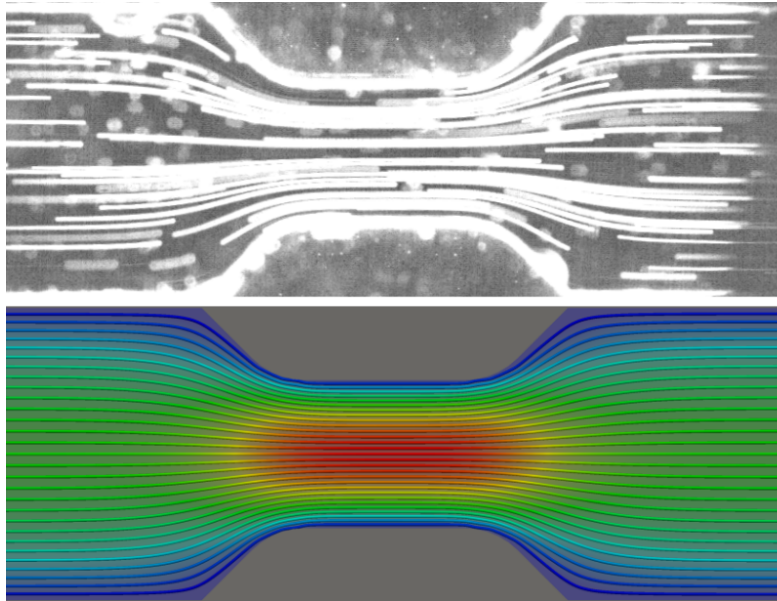
(a) Re = 1
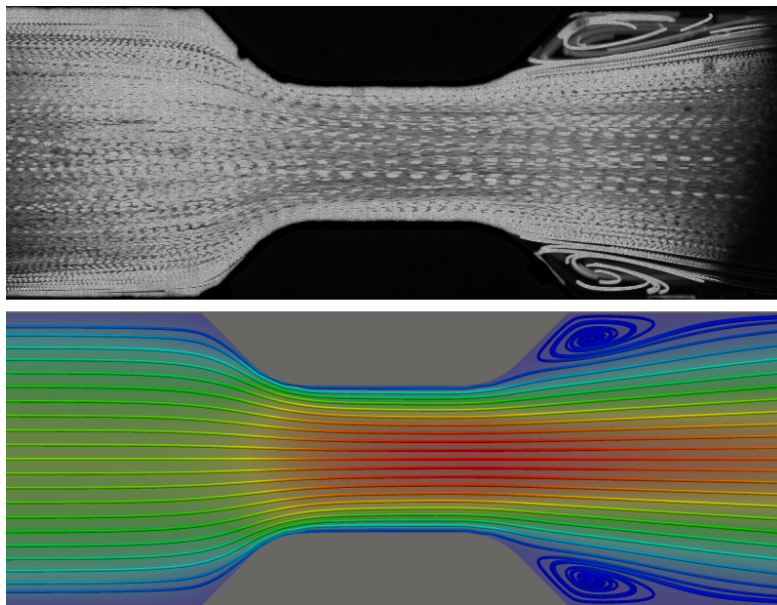
(b) Re = 100

Figure 3: The streamlines at (a) Re = 1 and (b) Re = 100 seen in the experiments (top) and in the simulations (bottom) at $z = 0$ (midway between bottom and top walls), respectively. The fluid enters from the left. The colors in the simulation figures correspond to the velocity magnitudes, cf. Fig. 4.

(a) streamlines and velocity magnitude


(b) shear stress magnitude
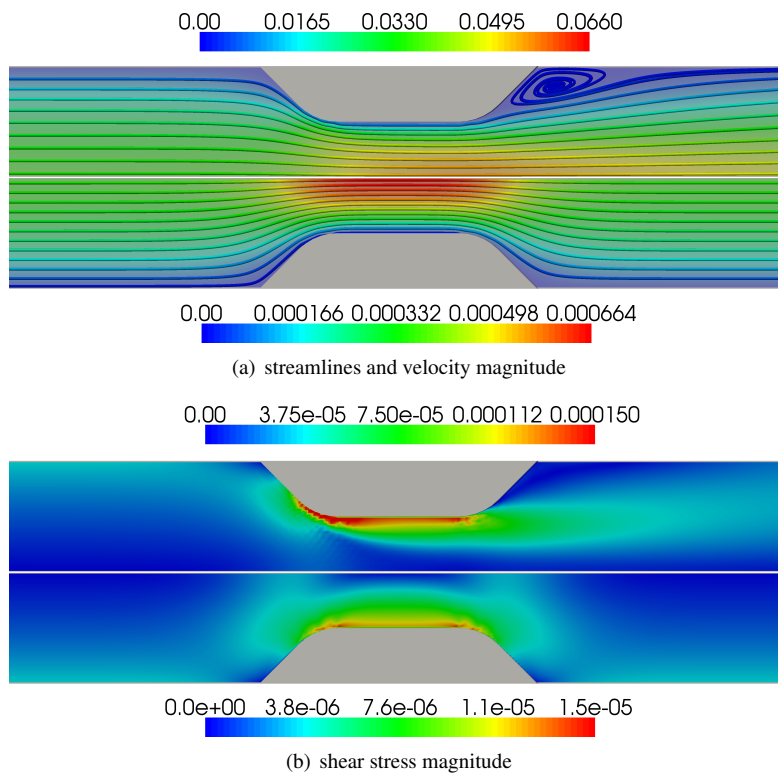
Figure 4: Direct comparison of the simulation results: (a) the streamlines and velocity magnitudes and (b) the shear stress magnitudes at $z = 0$ (midway between bottom and top walls) for Re = 0.1 (bottom) and Re = 100 (top), respectively. The fluid enters from the left. For convenience, the colors for the magnitudes have been chosen in such a way that equal values of $u/\bar{u}$ or $\sigma/\bar{\sigma}$ have the same color. Numbers are lattice values.

13
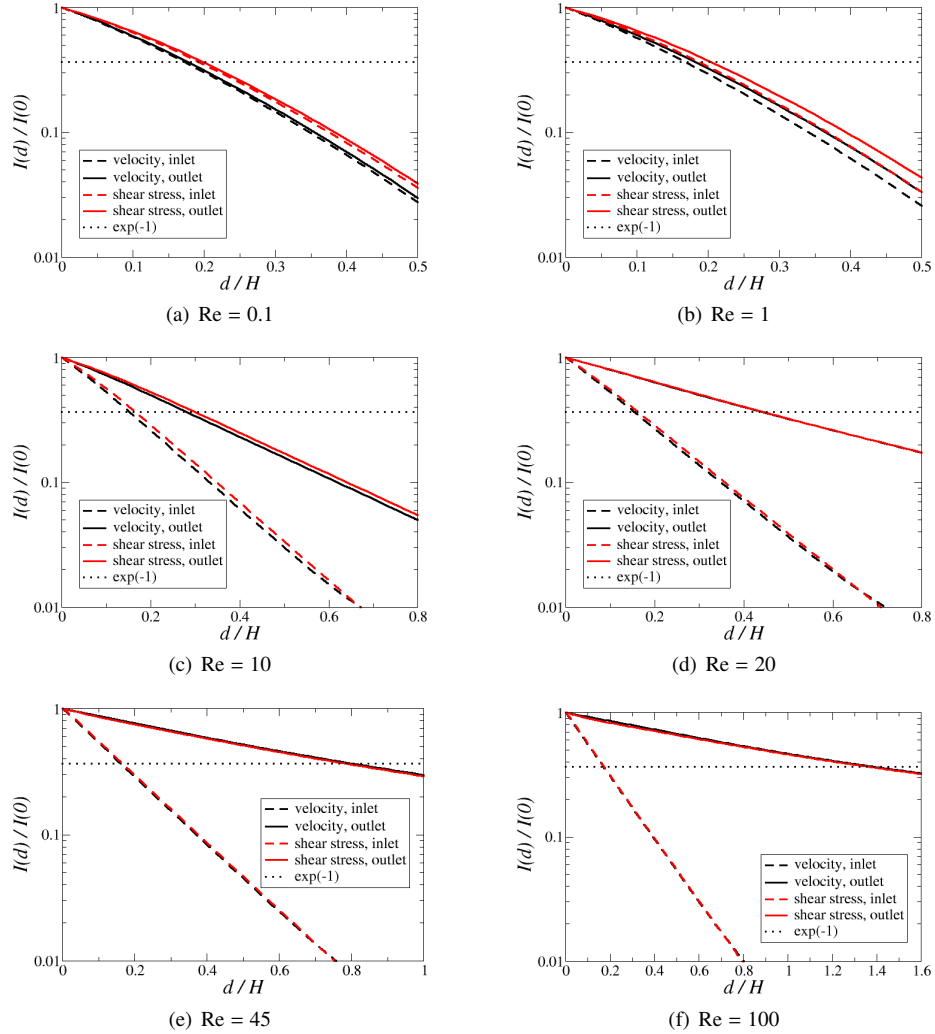
Figure 5: Presentation of the normalized indexes of distortion I_u and I_σ extracted from the simulation data. The indexes of distortion are defined as the relative deviations of the velocity/shear stress profiles at a given cross-section with a distance d from the constriction compared to the reference profile at the inlet, cf. Eqs. (10) and (11). For each Reynolds number, the normalized indexes of distortion are logarithmically plotted as function of the distance d/H from the beginning of the constriction to the inlet and from the end of the constriction to the outlet, respectively. Additionally, the $\exp(-1)$-level is marked, defining the ranges λ_u/H and λ_σ/H. Note that the ranges on the d-axis are different for the subfigures.

14
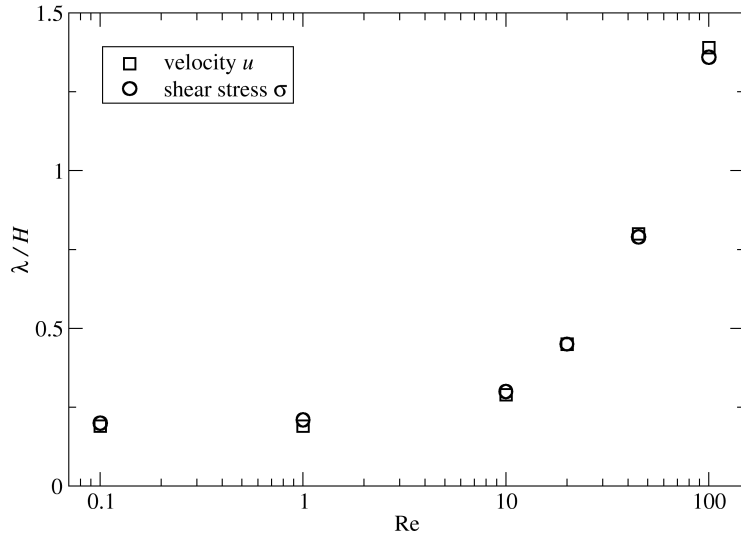
Figure 6: The computed ranges of decay λ_u, λ_σ in the outlet direction from Tab. 5 are shown as function of the Reynolds number. For Re ≤ 1, the ranges are constant, and the Stokes approximation is valid. For Re > 1, inertia effects are important and the relaxation of the fluid is significantly delayed. The results for λ_u and λ_σ are virtually identical for a given Reynolds number.
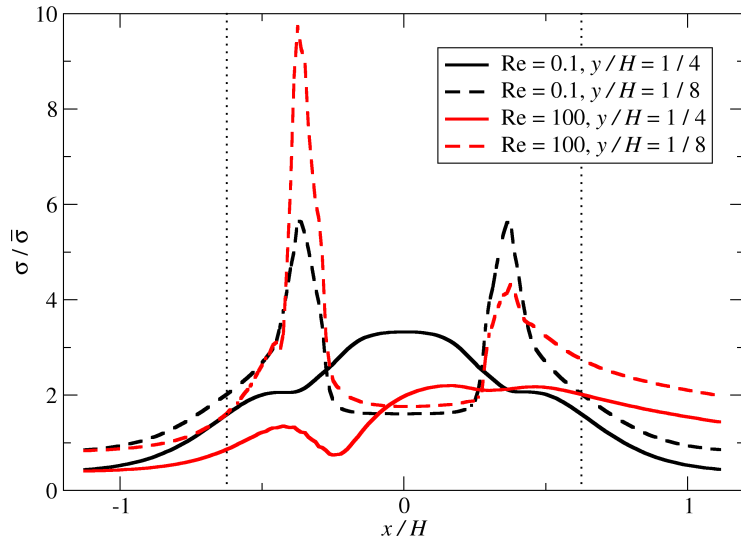

Figure 7: The shear stress $\sigma/\bar{\sigma}$ as a function of axial position x in the constriction at $z = 0$ (midway between bottom and top walls). For the Reynolds numbers 0.1 and 100, the shear stress evolution for two different lateral positions, $y/H = 1/8$ and $y/H = 1/4$, is shown ($y = 0$ corresponds to the central axis). The center of the constriction is located at $x = 0$. The vertical dotted lines mark the beginning and end of the constriction. For Re = 0.1, the slopes are symmetric with respect to $x = 0$. The shear stress near the lateral constriction walls ($y/H = 1/4$) is larger than closer to the central axis ($y/H = 1/8$). For comparison, see also Fig. 4(b).

15
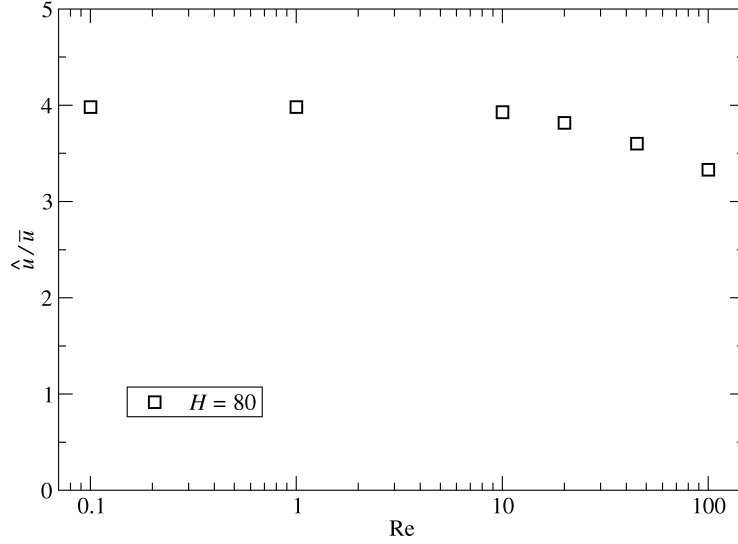
(a) maximum velocity magnitudes
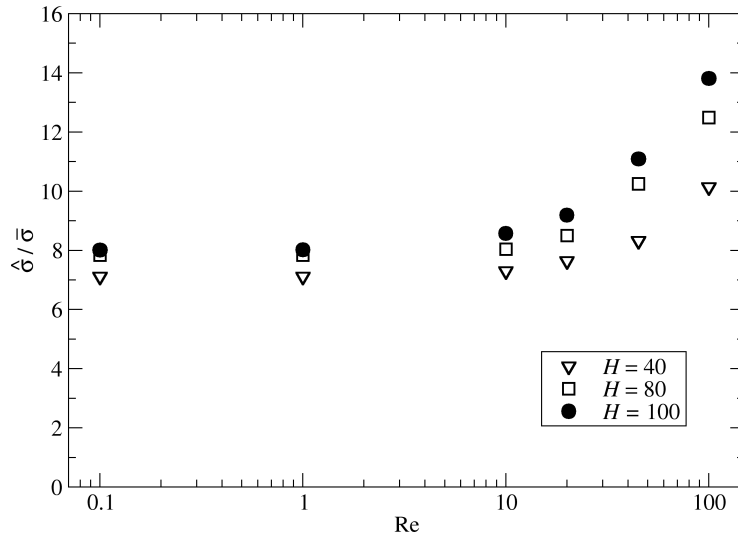
(b) maximum shear stress magnitudes

Figure 8: Maximum magnitudes of (a) the velocity and (b) the shear stress $\hat{\sigma}$ found in the entire simulation volume, normalized by the scales $\bar{u}$ and $\bar{\sigma}$ defined on the inlet, Eqs. (12) and (13). The shear stress results are shown for three different spatial resolutions (H = 40, 80, and 100), the velocity results only for H = 80. At small Reynolds numbers, $\hat{u}/\bar{u}$ and $\hat{\sigma}/\bar{\sigma}$ do not depend on Re, and inertia is negligible. At larger Re, the shear stress $\hat{\sigma}/\bar{\sigma}$ is increasing while the velocity drops. Those are effects caused by the non-linear terms in the Navier-Stokes equations.

16

those considerations into account, the agreement between experiments and simulations is satisfactory.

In order to test the confidence in the simulations, we have decreased the numerical resolution from $H = 100$ to $H = 80$ and 40 (data not shown). We observe that the numerical results for $H = 80$ are virtually identical to those for $H = 100$ indicating that the resolution is sufficient to capture the correct physics. Even for $H = 40$, the velocity data is accurate whereas the shear stress data starts to become unreliable. Thus, we believe that the simulation data is reliable. In the following, we will only report results extracted from the simulations since velocity and shear stress data is available locally at each point in the geometry.

In Fig. 5, the numerically obtained indexes of distortion for the velocity I_u and the shear stress I_σ are presented as function of the distance d from the constriction. The corresponding ranges of decay λ_u and λ_σ are shown in Tab. 5 and Fig. 6. It is obvious that the slopes of $I_u(d)$ and $I_\sigma(d)$ can be excellently described by simple exponentials with decay lengths λ_u and λ_σ, respectively. This justifies the approximations in Eqs. (14) and (15) and the introduction of the decay lengths λ_u and λ_σ.

For small Reynolds numbers (Re = 0.1 and 1), the curves of I_u and I_σ hardly depend on Re, cf. Figs. 5(a) and 5(b). This is a first hint that Re = 1 still is a good approximation for Stokes flow. A significant change in the slopes is visible for larger Reynolds numbers (Re > 1) which can be seen from Figs. 5(c) through 5(f). This is related to the influence of inertia.

There are only small differences between the inlet and outlet curves of I_u and I_σ for small Reynolds numbers, i.e., the flow fields are nearly symmetric with respect to the regions before and behind the constriction, cf. Figs. 5(a) and 5(b). This is another hint for the validity of the Stokes limit at Re $\leq$ 1. For larger Re, the indexes of distortion towards the outlet are always larger than those towards the inlet, indicating that the constriction mainly influences the flow behind itself, cf. Figs. 5(c) through 5(f). Obviously, the symmetry is broken due to the presence of inertia. This can also be seen in Fig. 7 where two examples of the spatial shear stress evolution are shown. For Re = 0.1, the curves are symmetric with respect to the center of the constriction, but for Re = 100, the asymmetry is clearly visible.

Analyzing the data shown in Fig. 5, it is obvious that the decay characteristics of the distortion of the velocity and the shear stress are similar if not identical, i.e., $I_u(d) \approx I_\sigma(d)$ and $\lambda_u \approx \lambda_\sigma$ for a given Reynolds number. Since the shear stress is related to the spatial derivatives of the velocity, this observation indicates that the velocity field uniformly relaxes. Deviations in the velocity gradient are diminished at the same rate as the deviations of the velocity themselves. In other words, there is only one characteristic decay length both for the velocity and the shear stress.

The increase of the outlet values of λ_u and λ_σ with Re is shown in Tab. 5 and Fig. 6. Qualitatively, the behavior of λ(Re) can be understood from Eq. (16), defining the development length L_D of the velocity in a pipe as function of the Reynolds number. Although the definitions of λ_u and λ_σ on the one hand and L_D on the other hand are not equivalent, both describe the same physics, namely the relaxation behavior of the fluid as a function of the Reynolds number. In Stokes flow, Eq. (16) yields a constant development length which is also the case in Fig. 6. There is a transition region for Reynolds numbers in the interval $[10 - 100]$ after which L_D(Re) becomes linear again.

The second linear region of λ_u and λ_σ, however, has not been probed in our simulations.

From Tab. 5 we find that the ranges of decay λ_u and λ_σ towards the inlet are always about $0.2H$, regardless of the Reynolds number. The interpretation is that inertia affects only the fluid inside and behind the constriction. The fluid approaching the constriction from the inlet feels the presence of the constriction only by momentum diffusion, and the Reynolds number does not play a significant role. This can also be seen by comparing the velocity and shear stress fields at different Re upstream of the constriction shown in Fig. 4. For Re = 0.1 and 100, the regions before the constriction look similar, but there are pronounced differences downstream. Applied to blood flow, this means that the constriction cannot cause clotting in the upstream region.

The previous discussions clearly show that non-linear effects become important at large Reynolds numbers. In Fig. 8, we present the peak magnitudes of the velocity $\hat{u}$ and the shear stress $\hat{\sigma}$ found in the entire simulation volume, normalized by the characteristic values $\bar{u}$ and $\bar{\sigma}$. In the Stokes limit, $\hat{u}/\bar{u}$ and $\hat{\sigma}/\bar{\sigma}$ do not depend on Re since non-linear effects are absent. The location where the fluid reaches its peak velocity $\hat{u}$ is on the central axis, either in the middle (smaller Re) or behind the middle of the constriction (larger Re), cf. Fig. 4(a). The maximum shear stress $\hat{\sigma}$ can be found at the side walls of the constriction, cf. Fig. 4(b). For large Re, the shear stress is maximum in the entrace region of the constriction. Inspecting the data for $\hat{u}/\bar{u}(\mathrm{Re})$ and $\hat{\sigma}/\bar{\sigma}(\mathrm{Re})$ in Fig. 8, one notices that there is no change for small Reynolds numbers (Re $\leq$ 1), i.e., inertia effects are still negligible. However, at larger Reynolds numbers, $\hat{u}/\bar{u}$ decreases. This can be understood qualitatively by comparing the time scales for diffusion and advection. On the one hand, at small Reynolds numbers, a distortion in the fluid mainly propagates by diffusion, and advection is negligible. On the other hand, advection is dominant at large Reynolds numbers. Since the constriction is a localized perturbation at the lateral walls, it takes some time until it can affect the fluid in the vicinity of the centerline. This time can be estimated by the diffusion time scale

$$t_D = \frac{H^2}{8\nu} \tag{18}$$

where $\nu = \eta/\rho$ is the kinematic viscosity. In this time, however, the fluid has already propagated by a characteristic distance $L_{DP} = \bar{u}t_D$ where $L_{DP}/H \propto \mathrm{Re}$. If L_{DP} is large with respect to the length of the constriction, the fluid leaves the constriction and starts to relax again before the fluid near the central axis is fully aware of the perturbation caused by the constriction. Hence, the centerline velocity does not as strongly increase during the passage through the constriction as for smaller Reynolds numbers. This is also the reason for the increase of $\hat{\sigma}/\bar{\sigma}$ with Re in Fig. 8(b). The volume flux of the fluid through any cross-section perpendicular to the x-axis has to be constant. Thus, the average fluid velocity must become larger inside the constriction. When the velocity near the centerline is not proportionally increased (which is the case at large Re), the fluid near the walls has to be faster to compensate. This, on the other hand, leads to a disproportionate increase of the shear stress near the walls. In fact, for Re = 100, $\hat{\sigma}/\bar{\sigma}$ is about 70% larger than in the viscous limit. This is a significant inertia effect which will be even more severe at Re > 100. The implication is that unfavorable blood vessel geometries in combination with large Reynolds numbers can lead to a significant

non-linear build-up of shear stress causing further complications during stress-induced blood clotting.

5. Conclusions

Large shear stresses in blood flow can lead to a conformation change of the protein von Willebrand factor. This may trigger undesired blood clotting in arteries which can eventually lead to a coronary thrombosis. In order to estimate the impact of inertia on the shear stress in coronary arteries, we have employed the lattice Boltzmann method to simulate the flow in a constricted geometry with Reynolds numbers between 0.1 and 100. We assume the fluid to be Newtonian since the particulate nature of blood and its non-Newtonian properties are only significant in small blood vessels like venules and arterioles.

The major observation is that the peak value of the effective von Mises stress σ_{vM} grows disproportionally fast with the Reynolds number in the inertial regime, Re $\geq$ 10. At Re = 100, a common value of the Reynolds number in coronary arteries, the peak value of σ_{vM} is about 70% larger than expected from assuming the validity of Stokes flow. This observation indicates that a combination of pathological blood vessel geometries and large Reynolds numbers may increase the risk of an heart attack. This is a pure hydrodynamic effect.

We further observe that the influence of the constriction is noticeable only inside and behind itself, i.e., upstream of the constriction, the flow field and the shear stress are not significantly influenced. The downstream distortion decays exponentially with the distance to the constriction, and its range grows linear with the Reynolds number for large Re. In particular, the inertial effects break the symmetry of the flow field upstream and downstream of the constriction.

With this article, we point out that pure hydrodynamic effects could be the reason for an increased tendency to blood clotting in pathologically altered blood vessel geometries in combination with large Reynolds numbers.

References

[1] S. W. Schneider, S. Nuschele, A. Wixforth, C. Gorzelanny, A. Alexander-Katz, R. R. Netz, M. F. Schneider, Shear-induced unfolding triggers adhesion of von Willebrand factor fibers, Proc. Natl. Acad. Sci. U.S.A. 104 (19) (2007) 7899–903.

[2] P. Libby, Current Concepts of the Pathogenesis of the Acute Coronary Syndromes, Circulation 104 (3) (2001) 365–372.

[3] A. Jeremias, B. Sylvia, J. Bridges, A. J. Kirtane, B. Bigelow, D. S. Pinto, K. K. L. Ho, D. J. Cohen, L. A. Garcia, D. E. Cutlip, J. P. Carrozza, Stent Thrombosis After Successful Sirolimus-Eluting Stent Implantation, Circulation 109 (16) (2004) 1930–1932.

[4] S. Chen, G. D. Doolen, Lattice Boltzmann Method for Fluid Flows, Annu. Rev. Fluid Mech. 30 (1998) 329–364.

[5] S. Succi, The Lattice Boltzmann Equation for Fluid Dynamics and Beyond, Oxford University Press, ISBN 978-0198503989, 2001.

[6] M. Sukop, D. Thorne, Lattice Boltzmann Modeling, an Introduction for Geoscientists and Engineers, Springer, ISBN 978-3540279815, 2005.

[7] B. Dünweg, A. J. C. Ladd, Lattice Boltzmann Simulations of Soft Matter Systems, vol. 221 of *Advanced Computer Simulation Approaches for Soft Matter Sciences III, Advances in Polymer Science*, Springer, 89, 2009.

[8] S. Chien, Shear Dependence of Effective Cell Volume as a Determinant of Blood Viscosity, Science 168 (3934) (1970) 977–979.

[9] W. Hort, H. Lichti, H. Kalbfleisch, F. Köhler, H. Frenzel, U. Milzner-Schwarz, The size of human coronary arteries depending on the physiological and pathological growth of the heart the age, the size of the supplying areas and the degree of coronary sclerosis, Virchows Archiv 397 (1) (1982) 37–59.

[10] H. Hikita, A. Sato, T. Nozato, T. Kawashima, Y. Takahashi, T. Kuwahara, A. Takahashi, Low coronary flow velocity and shear stress predict restenosis after sirolimus-eluting stent implantation, Scand. Cardiovasc. J. 43 (5) (2009) 298–303.

[11] M. H. Sadd, Elasticity: theory, applications, and numerics, Academic Press, ISBN 978-0123744463, 2009.

[12] R. Haberman, Applied Partial Differential Equations: with Fourier Series and Boundary Value Problems, Pearson Prentice Hall, ISBN 978-0130652430, 2004.

[13] J. Latt, B. Chopard, O. Malaspinas, M. Deville, A. Michler, Straight Velocity Boundaries in the Lattice Boltzmann Method, Phys. Rev. E 77 (5) (2008) 056703–16.

[14] T. Krüger, F. Varnik, D. Raabe, Shear stress in lattice Boltzmann simulations, Phys. Rev. E 79 (4) (2009) 046704–14.

[15] M. Friedmann, J. Gillis, N. Liron, Laminar flow in a pipe at low and moderate reynolds numbers, Appl. Sci. Res. 19 (1) (1968) 426–438.

[16] B. Atkinson, M. P. Brocklebank, C. C. H. Card, J. M. Smith, Low Reynolds number developing flows, AIChE Journal 15 (4) (1969) 548–553.

[17] F. Durst, S. Ray, B. Unsal, O. A. Bayoumi, The Development Lengths of Laminar Pipe and Channel Flows, J. Fluid Eng. 127 (6) (2005) 1154–1160.

[18] Y. H. Qian, D. D'Humières, P. Lallemand, Lattice BGK Models for Navier-Stokes Equation, Europhys. Lett. 17 (1992) 479.

[19] X. He, L.-S. Luo, Lattice Boltzmann Model for the Incompressible Navier–Stokes Equation, J. Stat. Phys. 88 (3) (1997) 927–944.

[20] L.-S. Luo, The lattice-gas and lattice Boltzmann methods: past, present, and future, in: Proceedings of the International Conference on Applied Computational Fluid Dynamics, Beijing, China, 52–83, 2000.

[21] A. J. C. Ladd, R. Verberg, Lattice-Boltzmann simulations of particle-fluid suspensions, J. Stat. Phys. 104 (5) (2001) 1191–1251.

[22] D. Raabe, Overview of the Lattice Boltzmann Method for Nano- and Microscale Fluid Dynamics in Materials Science and Engineering, Model. Simul. Mater. Sc. 12 (2004) 13.

An Experimental Study of the Influence of Coupling Configuration on the Efficiency of Surface Acoustic Streaming

Mohammad Amin Fallah*, Thomas Franke*, Achim Wixforth*

*Chair of Experimental Physics I, Physics Institute, University of Augsburg, Augsburg 86159, Germany

Corresponding Author:

Mohammad Amin Fallah
Universität Augsburg
Institut für Physik
Lehrstuhl für Experimentalphysik I
Geb. R, Ebene 3
Universitätsstr. 1
D-86159 Augsburg

Phone No: +49 (821) 598 33 11
Fax No: +49 (821) 598 32 25
mohammad.fallah@physik.uni-augsburg.de

Abstract

Microfluidics on a chip is an engineering challenge due to the considerable increase of the surface to volume ratio, when compared to macrosystems. Hence, there have been many challenging problems to be solved when it comes to designing effective functional microfluidic systems on a chip. For instance, the necessity of pumping and mixing in sub-micro-liter volumes calls for avoiding conventional pumps and actuators and for the development of novel schemes. Some of these issues have recently been partially resolved by the application of acoustic streaming mediated by surface acoustic waves (SAW). To mix nano-liter volume of reagents by the employment of such SAW generated by an interdigitated transducer (IDT) have proven to be a very effective application of a novel physical phenomenon. The same principle has been applied for actuating liquids in form of a droplet on a chip surface [Wixforth et.al]. However, when it comes to pumping fluids in low volume tiny 3 dimensional capped micro-channels, the conventional transducer-microchannel coupling configuration seems to lack efficiency. Hence, we have experimentally studied the possibility of improving the efficiency by finding more beneficial transducer-microchannel coupling configurations. The result would be the optimization of acoustic streaming by improving the actuator channel coupling configuration; making the acoustic streaming even more favorable for commercial and research application than before.

Keywords: Acoustic Streaming, Surface Acoustic Waves, Interdigitated Transducer, Capped Micro-channels.

1. Introduction

Integration of the external parts of a fluidic system (pumps, valves, reactors etc.) into the system, together with downsizing is an important task that needs considerable attention. Downsizing a macro-fluidic system into a micro-fluidic one has many very well-known advantages discussed elsewhere in details [1]. However, the most novel vision is the possibility of the integration of different components of a conventional laboratory on to a "Lab-on-a-Chip" system. One of the components of a Lab-on-a-chip device that plays a crucial role in downsizing and integration is the fluid pump. In fact, the generation of a stable flow at low Re regimes has been shown to be the most challenging part. A fluid in such

systems is usually driven by external means such as pneumatic pressure or syringe pumps, or integrated pumping schemes like electrophoresis or employing soft layer lithographic tools [2]. Complex handling and the possibility of contamination are common drawbacks of such systems [3]; not forgetting that an external conventional pump together with tubes and all the other necessary components create undesired dead volumes and changes the total lab-on-a-chip system into a bulkier conventional fluidic system with micro-tracks/channels. Even internal pumping methods like electro-osmotic flow or valve type micro pumps which operate based on piezoelectric actuations exhibit some deficiencies discussed in details elsewhere [4,5].

Surface acoustic waves (SAWs) have been applied in different research disciplines not only in our labs but also in commercial scales for some years now [6-9]. SAWs of well-defined polarization can be excited by application of a radio frequency signal to an Inter-Digitated Transducer (IDT) on a piezoelectric substrate. An IDT is composed of metallic interdigitated electrodes deposited on top of a piezoelectric substrate. The small surface displacement caused by the radio frequency signal introduced to the IDT propagates as a well-defined surface wave along the surface of the substrate and can couple to the liquid on top of its surface. There, it induces acoustic streaming [6-10]. In brief, a SAW is essentially a sound wave of about 1nm in amplitude and wavelength of typically a few micrometers travelling along a solid-air interface. Due to the poor impedance match between substrate and air (large difference in sound velocities in the media), only very little energy is dissipated for this "pure mode". However, when a SAW encounters a solid-liquid interface, the impedance matching changes drastically, causing a large dissipation of acoustic energy into the fluid (Fig. 1). The energy dissipation causes an exponential decay of the SAW amplitude along its propagation direction within a characteristic length scale of a few wavelengths. This in turn causes an acoustic pressure gradient driving the liquid to flow. Considering a typical channel length of a

few centimeters and a decay length L_D of about 100μm, the pump essentially acts as a point-like pressure source driving the liquid to flow according to conservation of mass (Fig.1.).
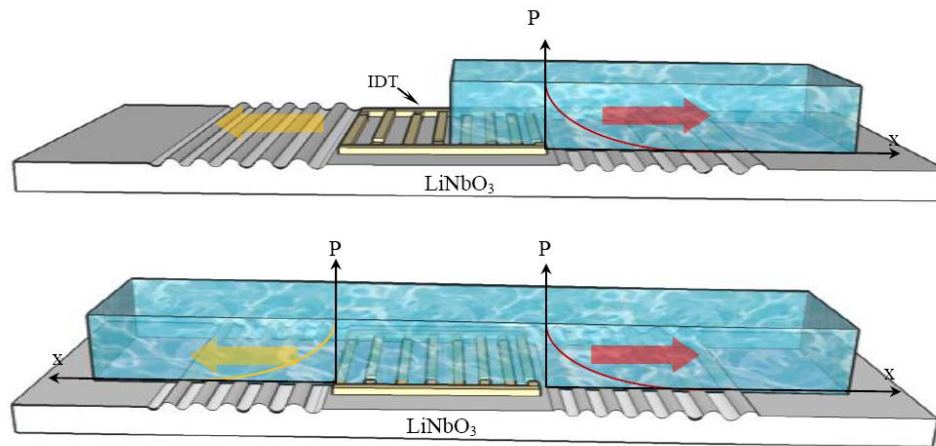

Fig.1. A schematic sketch of Acoustic Streaming. The piezoelectric lattice distortion caused by strong local electric fields generated by application of a radio frequency signal to a transducer, excites the SAWs. The acoustic waves can couple to a liquid in contact with the surface of the piezoelectric. The decay of the SAWs causes a pressure gradient along the waves' propagation direction. The pressure gradient moves the fluid along the wave decay direction. Fig.1.a. (Top) A schematic representation of acoustic streaming in the conventional IDT-channel coupling mode. Just the forward waves are used for inducing acoustic streaming in the μ-channel. Fig.1.b. (Below). A schematic representation of a new coupling mode between the transducer and μ-channel, which enables the system to benefit from streaming caused by the backward (orange color) SAWs, in order to increase pumping efficiency. In a closed circulation μ-channel, it is necessary to reflect the streaming caused by the backward-waves back into the desirable pumping direction.

Acoustic streaming can be induced in different types of fluid tracks and micro-channels, including modified hydrophobic/hydrophilic tracks, uncapped micro-channels, and finally capped microchannels. The modified tracks and uncapped micro-channels are favorites when it comes to lab-on-a-chip systems due to simplicity of automation, and ease of setting multiple new configurations. The capped channels, on the other hand, have advantages like reduced fluid evaporation (especially at elevated temperatures) and less chance of contamination. Also, loading closed channel system with biological or hazardous material in a safe environment represents a clear advantage in some cases as compared to an open system. It makes the handling of dangerous and expensive materials much safer and easier.

In this work, an interdigitated transducer is employed for the creation of acoustic streaming in capped micro-channels (Fig. 1). Due to the symmetrical structure of the

transducer's electrodes and the anisotropic nature of the piezoelectric substrate (in our work LiNbO$_3$, 128° y-cut, z propagating), the transducer excites SAWs perpendicular to the electrodes in both opposite directions (Fig. 1). Usually, a proper design of the transducer-channel coupling configuration ensures SAW excitation into one of the directions (Fig. 1.a). This method simplifies acoustic pumping, but non-evidently results in an immediate energy loss of 3dB or 50%. A way out would be the use of single phase unidirectional transducers (SPUDT), which however, are more expensive to produce than the simple ones.

Hence, in order to reduce the losses, we have decided to study the possibility of reflecting at least a part of the backward SAWs' lost energy by changing the channel-IDT coupling configuration experimentally.

2. Set-up and the Experiments

2.1. Set-up

The components of our set-up are: a tranducer, microchannels, radio frequency signal generator, and a fluorescence/phase contrast microscope to record live videos of our experiments.

For our experiments, the SAW is excited on an anisotropic piezoelectric material (LiNbO$_3$, 128° y-cut, z propagating) and is well described by the so called Rayleigh mode [11-12]. A pair of interdigitated metal electrodes are deposited on top of the substrate using standard lithography and a high frequency signal is to generate the SAW. Each individual electrode consists of a set of fingers which interdigitate with the ones of the other electrode. Pitch and spacing of these fingered electrodes defines the impedance and in lowest order also the resonance frequency:

$$f = {c_{SAW}}/{\lambda} \qquad\qquad\qquad\qquad\qquad\qquad\qquad (1)$$

The generation of a SAW requires a radio frequency (RF) input signal between 100Mhz and 1GHz and an amplitude between -40 dBm and +29 dBm, in our case. We generate these RF voltages using a simple signal generator (voltage controlled oscillator "ZX95-200-S", Mini Circuits, USA, Brooklyn). The signal from the voltage controlled oscillator has an amplitude of 10 dBm, that is amplified to an operational amplitude of up to +29 dBm by using an amplifier (ZHL-2, Mini Circuits, USA, Brooklyn).

Grace to the optical transparency of the piezoelectric material used, we are able to monitor the microfluidic chip with an inverted microscope (Zeiss Axiovert 200, Zeiss, Göttingen, Germany). Employing this phase contrast microscope, one can observe and monitor the streaming in the microchannel by tracking the tracer beads (Yellow Green Sulfate Latex Beads, Interfacial Dynamics Corporation, Oregon, USA). Also, either phase contrast microscopy or fluorescence microscopy can be easily employed. A CCD camera (C8484-05C, Hamamatsu, Japan) is used for the documentation of experiments in the form of videos and still pictures.

The desired geometrical structure of the micro channel is first sketched using AutoCAD software. The generated pattern can be transferred to a mold by photolithography or by micro milling techniques. For the presented experiments, the latter technique was applied. The resulting mold is a negative of the final micro-channel. Then, the mold is filled with an elastomer Polydimethylsiloxane (PDMS) (Dow Corning GmbH, Wiesbaden, Germany), a biocompatible transparent polymer. This way, one obtains the desirable channel structure after removing the PDMS from the mold. However, it turns out that a 'remote' coupling of the SAW into the channel is favorable as compared to a monolithic solution. For this reason, we mount the PDMS channel on a glass slide and couple this to the SAW

supporting chip with the IDT underneath. The optimum coupling is achieved by index-matching the glass slide and the LiNbO$_3$ chip with a coupling fluid.

2.2. Experiments
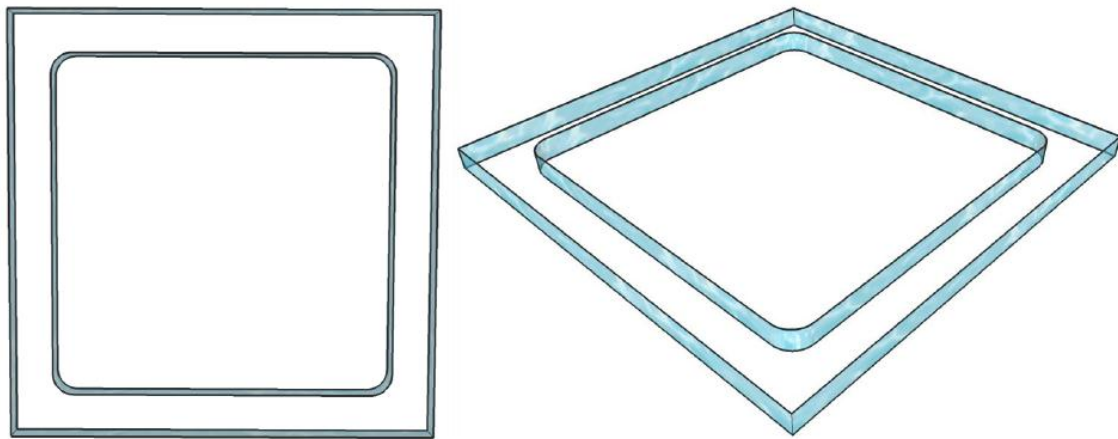
Fig.2. A schematic Sketch of the most conventional capped µ-channel geometry employed for studying the role of the IDT-channel coupling configuration in this work, from two perspectives. Width of the channel reads 1mm, and height is equal to 0.5mm.

To achieve optimum SAW coupling to the fluid in the channel, we have systematically varied the geometrical position of the IDT with respect to the channel. Also, we have employed SAW reflector structures at the side of the IDT opposing the channel. Three different factors might be envisioned to the coupling into the desired streaming direction. These are geometrical channel designs at the coupling point, the coupling position, and the last but not the least the coupling angle with respect of the channel axis. Figure.1.a is schematic sketch of the simplest IDT-channel coupling, with a non-evitable loss into the backward direction (yellow arrow). The fluidic channel and the IDT reside on the same substrate with only half of the IDT covered by the fluid. Streaming in this configuration is induced only into one direction but half of the acoustic energy is lost. In contrast we show the

scheme depicted in figure.1.b; here the channel-IDT coupling configuration also allows for the coupling of backward SAWs into a liquid, resulting in a backward streaming.

In figure.2, we depict the most conventional geometry of capped channels applied for acoustic streaming in micro-fluidic devices. As the SAW acts as a point source with limited extension into the direction of the streaming, a closed loop is chosen for the channel to ensure a continuous flow. To couple a SAW into such a channel, we show the IDT together with the channel in figure.3.
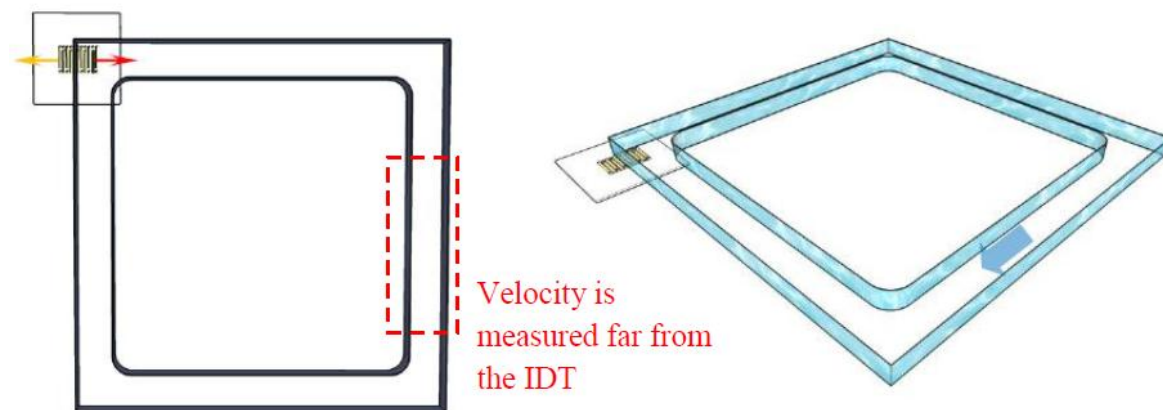

Fig.3. A 3D sketch of the conventional IDT-channel coupling. The desired streaming direction is clockwise (shown in dark blue).

Thus, for improving the pumping in such simple configurations, we have tried 6 different coupling positions for the channel geometry; where in the first configuration half of the length of the IDT is coupled under the microchannel footprint (Fig.4.). Some of such different inferring positions are sketched in figure.4. The position of the center of the exciting IDT is varied by about half of its length toward the middle of the channel. As shown in figure.4, in the first three configurations (1, 2, and 3) the IDT is coupled in a way that the IDT's outer sideline corresponds to under the channel's outer side line. Accordingly, the

second three configurations (4,5, and 6) are chosen such that the lower sideline of the IDT corresponds to the inner sideline of the micro-channel. The fluid velocity is measured far from the IDT as depicted in figure 3.
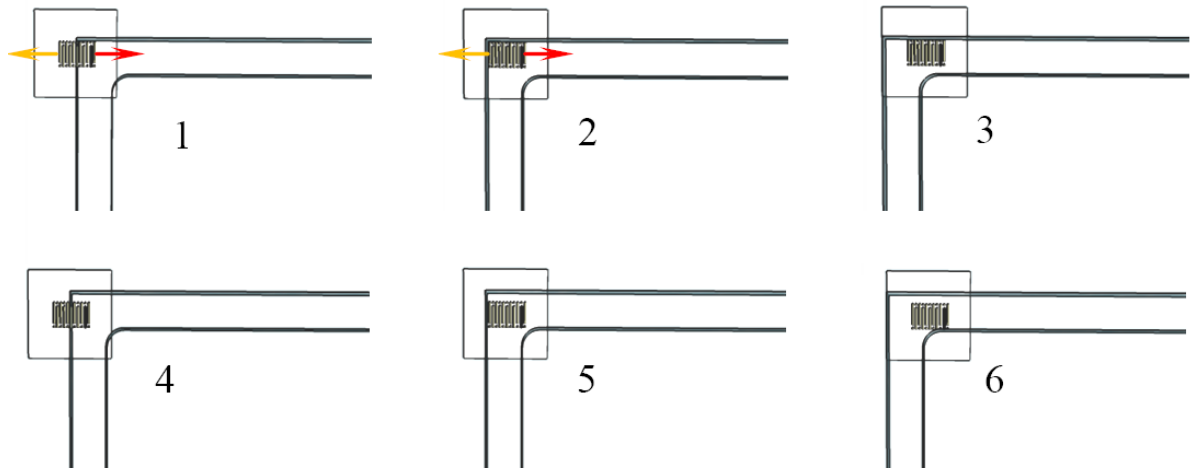

Fig.4. Schematic sketch of the 6 different coupling positions studied for the conventional μ-channel. Considering the length and width of the employed IDT to be respectively 0.9mm and 0.6mm, the coupling positions are the result of dislocation of the IDT equal to half of its length in each step, along the lower and higher side lines of the channel. In this way, one can systematically study the possibility of reflecting the backward streaming (shown with an orange arrow) excited by the IDT into the desired streaming direction, inside the channel.

Also, the role of coupling angle for the streaming efficiency has been studied at each of the described coupling positions (Fig.5). This was expected to have an effect on reflection of backwards waves into the desired streaming direction, especially for those positions of the IDT which are completely underneath the channel.
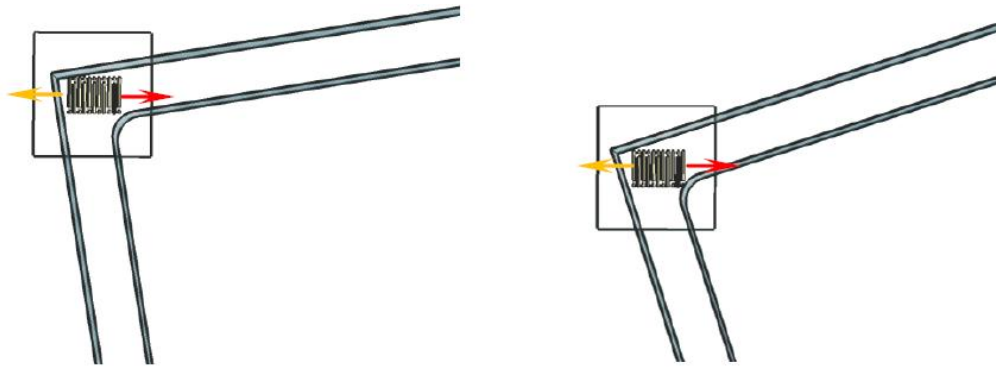
Fig.5. At each of the 6 coupling positions shown in fig.4 the IDT is coupled to the μ-channel with 3 different coupling angles. A coupling angle of zero degree refers to the transducers' length completely parallel to the channel's axis. Coupling angles of 20° and 40° are also investigated for each coupling position. In this figure coupling angles of 20° and 40° are schematically illustrated for an arbitrary coupling position, in order to provide a better understanding.

Our study of the different coupling angles at each coupling position reveals the need for optimization of the micro-channel geometry at the coupling point. Hence, a total of 5 different channel geometries have been designed. The goal was to explore a possible positive use of backwards wave reflections. Figure No.6 shows a sketch of how different geometrical patterns may be used to reflect backward-SAWs into the desired streaming direction.
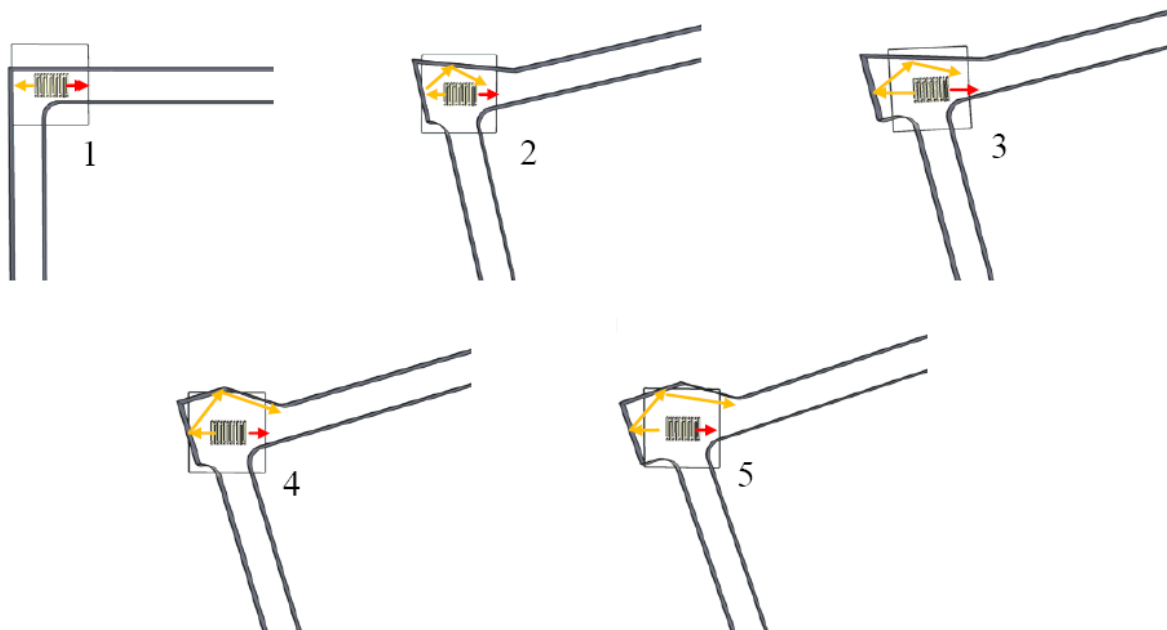

Fig. 6. 5 different geometries have been designed in order to study the effect of μ-channel's geometrical design on the backward waves' reflection. The aim is reflecting the backward waves back into the desired streaming direction. The red arrows represent a schematic sketch of forward SAWs in random coupling configurations for any of the 5 designed geometrical designs. Orange arrows represent a schematic of probable reflection of backward SAWs due to the channel structure at the coupling point. Note.1: Coupling positions are chosen randomly out of the 18 studied coupling configurations for each geometrical design. Note.2: Arrows' length does not represent the waves' magnitude.

In order to systematically conduct the experiments, one has to couple the transducer to comparable positions for all the 5 geometries. The goal here is the investigation of the role of the back reflector geometries in comparison to the conventional micro-channel. The 6 different coupling positions together with four different reflector geometries are shown in fig. 7.
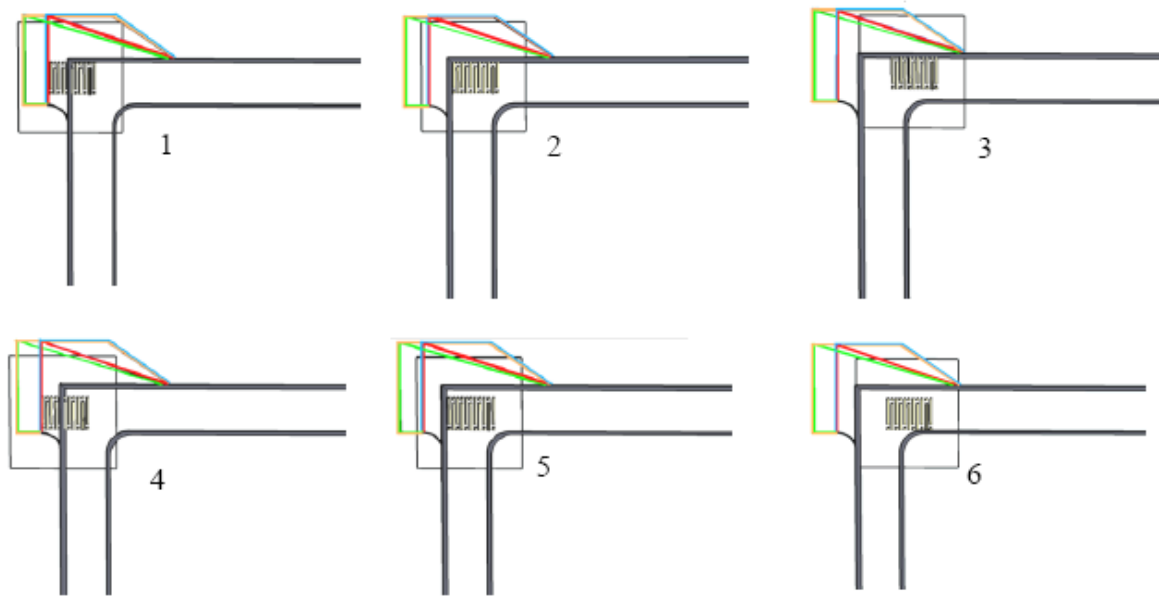

Fig.7. A schematic sketch of 5 different geometrical designs studied in this work at each of the 6 coupling configurations with 0° coupling angle (SAW propagation parallel to the channel's axis). In addition to the standard conventional micro-channel which has no specific back-reflector structure , there are 4 nearly identical other channels, that differ only based on their back reflecting structures(shown in colors) at the point of coupling. 6 different coupling configurations are studied for each channel geometry, in order to provide a better understanding of the channel-IDT coupling role in acoustic streaming, providing us a total 30 different experimental configurations, for 0° coupling angle. The digits 1-6 represent the coupling position, and the back-reflectors are shown in colors.

As discussed before, the coupling angle can be another important factor on the efficiency of the acoustic streaming in a closed channel loop. In order to investigate the role of this coupling angle, all the coupling configurations in Fig. 7 are also investigated for other coupling angles of 20° and 40° with respect to the channel axis (Figure.8).
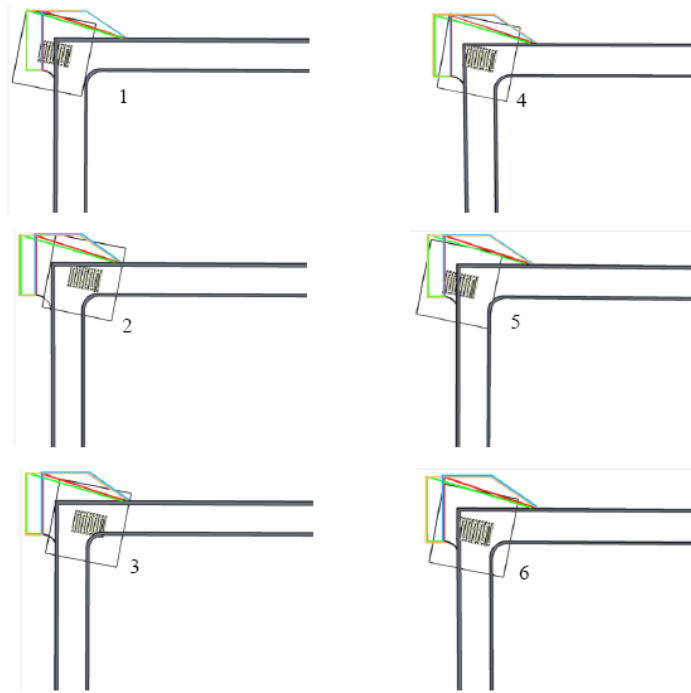
Fig. 8. A schematic sketch of different coupling configurations for the 5 studied micro-channels at non-zero coupling angles. As shown, one can see that the coupling angle is not anymore 0°, which means that the SAW propagation is not anymore completely parallel to the micro-channles's axis. At each of the 6 coupling configuration, for all the 5 channels geometries two different coupling angles of 20° and 40° are studied experimentally. Hence, streaming velocity in a total of 90 different experimental configurations is explored. The digits 1-6 represent the coupling position. The back-reflectors are shown in colors.

During the investigation of the aforementioned total of 90 configurations an interesting phenomenon was observed. It is well known that in the volume right above the IDT, SAW induced vortices appear [13]. We found that when the channel is narrower at the coupling position, the size (diameter) and also the number of observable vortices changes. Since all the experiments are conducted using the same transducer and applying the same frequency and power for SAW generation, our experimental findings indicate that with reducing the number and the diameter of the vortices power is more efficiently used to actuate the fluid. This is understandable as the energy dissipated in a vortex is basically lost for the pumping.

In order to investigate this phenomen, a new channel geometry has been designed (Fig.9), where in addition to the 6 standard coupling positions, 3 other coupling configurations (7,8, and 9) with varying channel widths are also investigated. This geometry

helps us to understand the role of the channel geometry in reducing the negative effect of the vortices on the acoustic streaming.
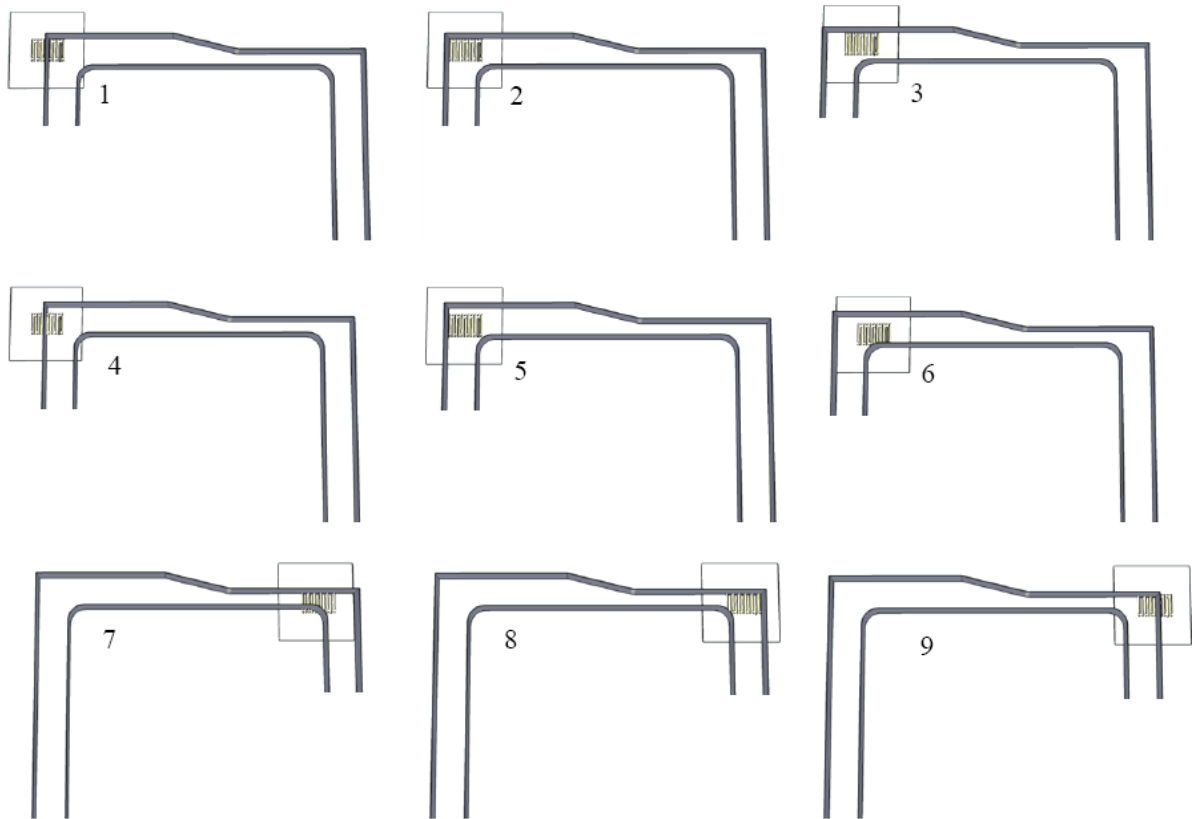

Fig. 9. A schematic sketch of the 6'th geometrical design and its 9 different coupling configurations. The channel geometry and its coupling configurations are designed in order to study the role of channel geometry on vortices formation at the point of coupling .

3. Results

In Fig. 10, we comprise the findings of our experiments in terms of a coupling efficiency as a function of coupling configuration. Fig. 10a shows the results for a coupling angle of 0°, in Fig. 10b we depict the same results for an angle of 20°, and in Fig. 10c, the measurements for an angle of 40° are shown. Each of the panels summarizes our findings for the five different channel geometries and the 6 different coupling positions discussed above.

To parameterize the coupling efficiency, we have chosen to measure the streaming velocity far away from the IDT on the opposite branch of the channel loop. For the 5 studied channel varieties; The general trend shows an increase of streaming velocity when the IDT is located completely underneath the channel. Despite a few exceptions, the streaming velocity is higher at coupling positions 2, 3, 5, and 6, as compared to coupling position 1 and 4. This trend endorses our hypothesis of streaming enhancement by reflection of backward SAWs. The only exception is the pattern no. 3 at coupling positions 1, 2, and 3 where a decrease of streaming velocity is measured. The channel pattern no.1 seems to be completely immune towards a change of the coupling positions.

Figures 10.a and 10.b show the effect of changing the coupling angle on the streaming velocity. At a glance, the aforementioned observations seem to be more inconsistent for the coupling angle of 20°, than of 0°, but with an exception of geometrical pattern no.1, an increase of streaming velocity by coupling the channel at coupling positions 2, 3, 5, and 6 in comparison to coupling positions 1, and 4 is observed. The mean velocity, however, is reduced in comparison to the 0° coupling angle.

Figure 10.c. represents the streaming velocity in the case of coupling angle of 40°. There is no discernible trend to see except for a steep decrease of the streaming velocity at 40° coupling angle as compared to the 0° configuration. In many cases, even negative velocity values have been obtained, representing a streaming in the undesirable direction (counter-clockwise in the sketches).
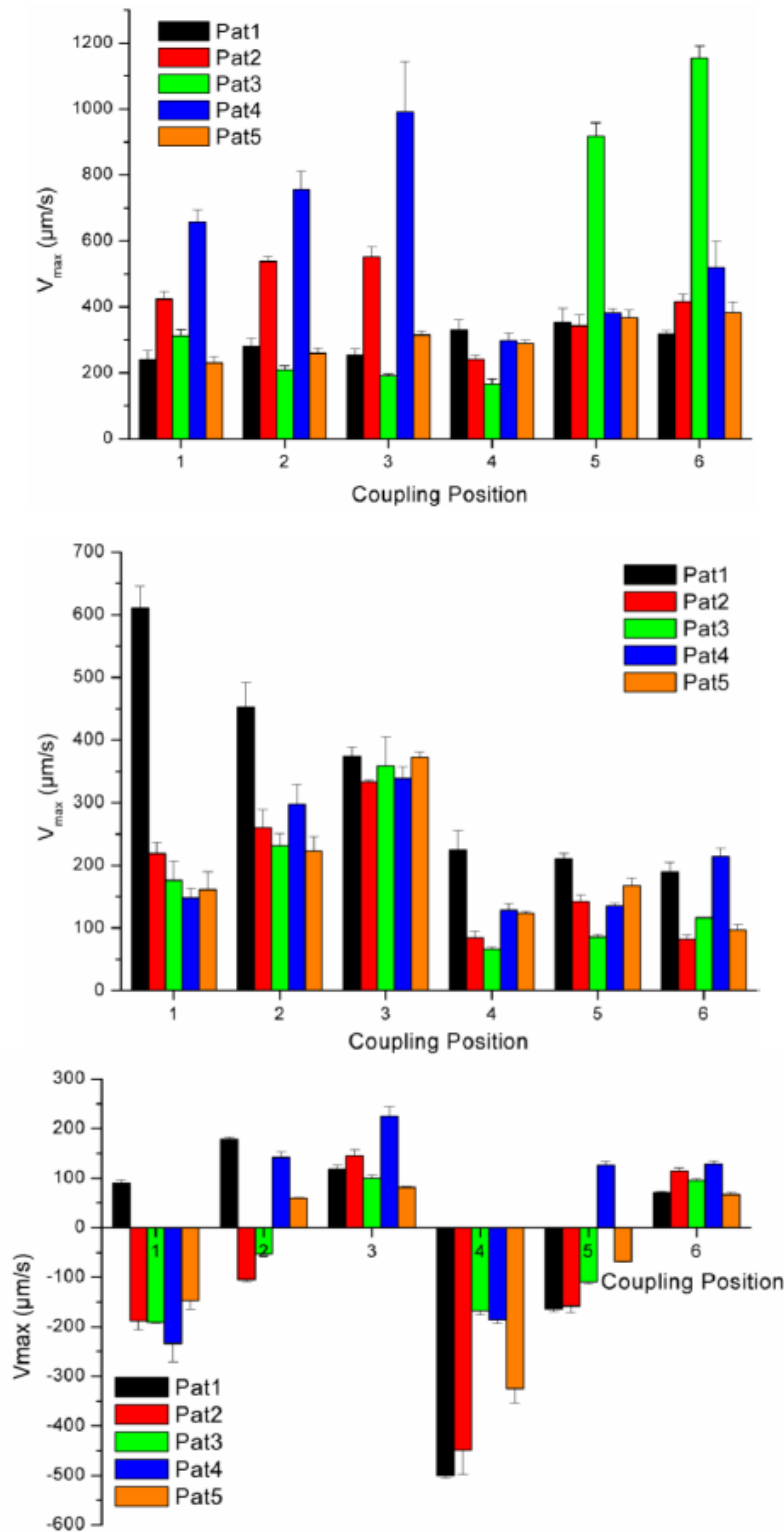
Fig. 10. A. Maximum streaming velocity at different coupling positions, for different geometrical patterns, at different coupling angles: A. (top): 0° coupling angle. B. (middle): 20° coupling angle. C: (bottom): 40° coupling angle. The very first pictures that comes into one's mind is the decrease of streaming velocity with the increase of coupling angle. The trend of streaming velocity for the case of 0° coupling angle is discussed in details in text.
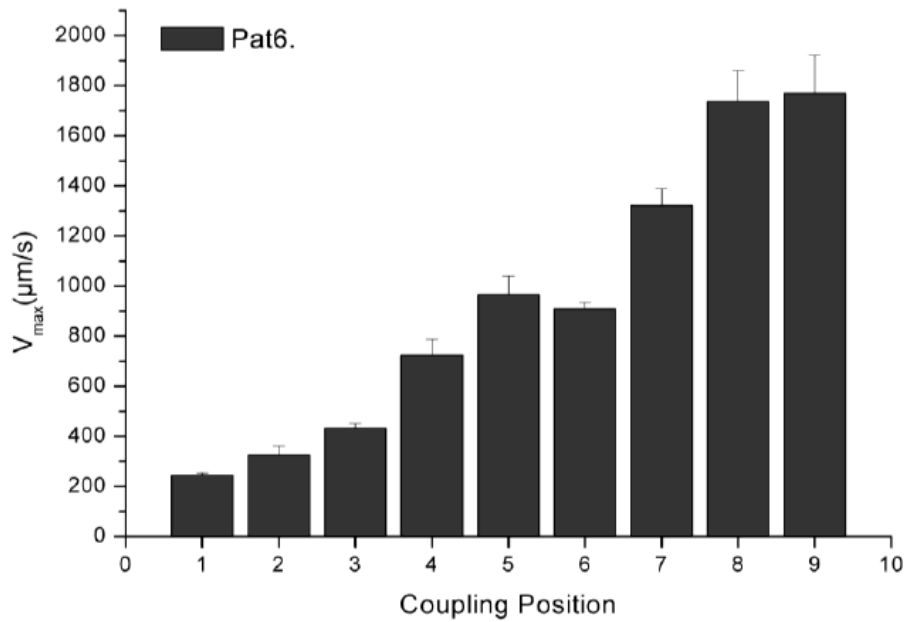
Fig. 11. Maximum streaming velocity at different coupling positions, for the 6'th geometrical pattern, at different coupling positions. A significant increase in streaming velocity is observed where the channel is narrower than the IDT itself. The maximum streaming velocity is also observed in the 9'th configuration of this pattern.

In figure 11 we comprise the rising streaming velocity trend at coupling positions 2, 3, 5, and 6 in comparison to coupling positions 1, and 4. This finding again endorses our hypothesis of backward SAWs reflections. Although, the maximum velocities arise at positions 7, 8, and 9 which originally had been designed in order to investigate the effect of the channel geometry (width) at the coupling point, on the vortices; In order to, investigate the possibility of energy win by reducing the diameter and volume of vortices in action. Interestingly, the highest streaming velocity ($\approx$2000μm/s) is attained when a narrower channel geometry (Pattern 6, coupling positions 7, 8, and 9) is simultaneously coupled at a coupling configuration, where the IDT is completely underneath the channel (coupling position 9). Hence, in this configuration one can benefit the backward SAWs and a less destructive role of vortices (Fig. 12) probably due to smaller vortices.
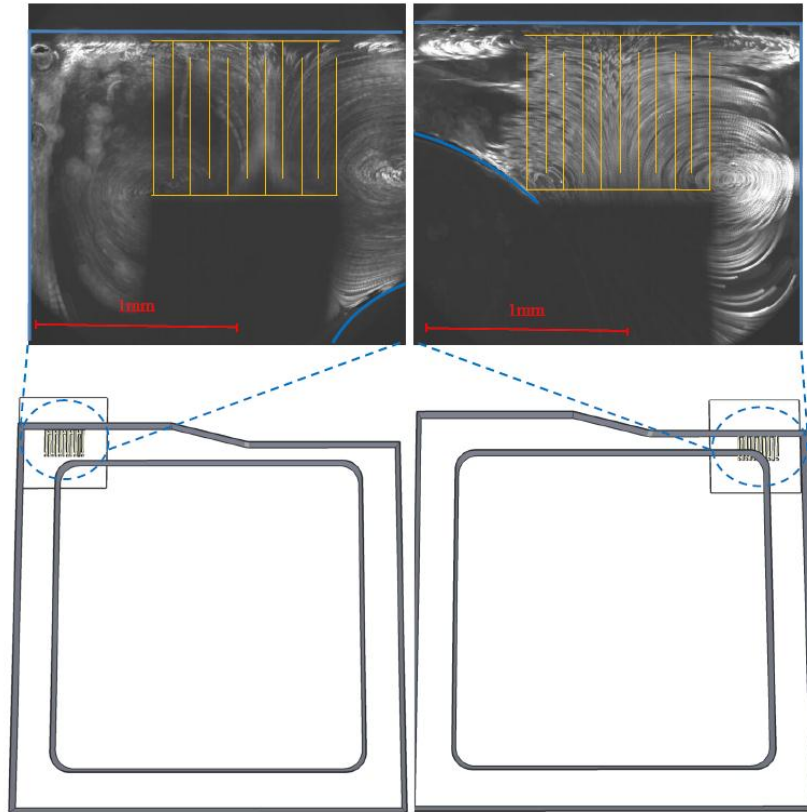
Fig. 12. A schematic comparison of the vortices formed in the fluid at coupling configurations No.9 and coupling configuration No.3, geometrical pattern No.6. It is believed that the higher streaming velocity increases by narrowing the channel at the coupling point, since the channel side walls can suppress the vortices more effectively, which leads to a smaller energy loss due to minimized rotation of fluid.

5. Discussion

In spite of the complicated nature of interpreting the results while studying so many different configurations, one can clearly state that changing the coupling angle from 0° to 20° and consequently to 40° is counterproductive. The recommended coupling angle in the absolute majority of configurations is 0°, as expected.

At the recommended 0° coupling angle, with just very few exceptions, positioning the IDT completely underneath the channel is recommended. The quality of reflection can still be improved by using materials with better reflective properties than PDMS.

The most effective method for an improvement of the acoustically mediated streaming velocity inside capped channels is to deliberately control the size of the inevitable vortices. This can be achieved by changing the channel geometry at the location of the coupling; this together with benefiting from the backward SAWs have resulted in an increase of streaming velocity from 200μm-300μm per second to 1800μm-2000μm per second, just by employing minor changes in channel geometry and coupling configurations. This method enables us to benefit the already well-established set-ups and research infra-structure, that are laid based on the transducer-liquid, transducer-channel couplings; and upgrading them to up to 10 times faster systems.

References:

1. Patrick Tabeling, Introduction to Microfluidics, Oxford University Press(2005), ISBN 0-19- 856864-9 978-0-19-856864-3, P.1-21, P.75-96, P.248- 254.

2. M. A. Unger, H. P. Chou, T. Thorsen, A. Scherer, S. R. Quake, Monolithic microfabricated valves and pumps by multilayer soft lithography, Science. 2000 Apr 7;288(5463):113-6.

3. E. M. Purcell, "Life in low Reynolds numbers", Am. J. Phys., Vol.45, No.1, January 1977, P.3-11. H. Andersson,

4. A. van den Berg, Lab-on-Chips for Cellomics, Micro and Nanotechnologies for Life Science, Springer, Amsterdam, 2005.

5. N. Lion, T. C. Rohner, L. Dayon, I. L. Arnaud, E. Damoc, N. Youhnovski, W.Zhi-Yong, C. Roussel, J. Josserand, H. Jensen, J. S. Rossier, M. Przybylski, H. H. Girault, Electrophoresis 2003, 24, 3533.

6. A. Wixforth, C. Strobl, C. Gauer, A. Toegl, J. Scriba, Z. Guttenberg, Anal. Bioanal. Chem. 2004, 379, 982.

7. Z. Guttenberg, H. Muller, H. Habermuller, A. Geisbauer, J. Pipper, J. Felbel, M. Kielpinski, J. Scriba, A. Wixforth, Lab Chip 2005, 5, 308.

8. Z. Guttenberg, A. Rathgeber, S. Keller, J. O. Radler, A. Wixforth, M. Kostur, M. Schindler, P. Talkner, Phys. Rev. E 2004, 70, 056311.

9. K. Sritharan, C. J. Strobl, M. F. Schneider, A. Wixforth, Z. Guttenberg, Appl. Phys. Lett. 2006, 88, 054102.

10. W. L. M. Nyborg, "Acoustic streaming," in *Physical Acoustics,* vol.2B, W. P. Mason, Ed. New York: Academic Press, 1965, pp. 256–331.

11. L. J. W. S. Rayleigh, "On waves propagating along the planar surface of an elastic solid," Proc. Lond. Math. Soc., vol. 17, no. 3, pp.4–11, 1885.

12. R. M. White and F. W. Voltmer, "Direct piezoelectric coupling to surface elastic waves," *Appl. Phys. Lett.*, vol. 7, no. 12, pp. 314–316, 1965.

13. T. Frommelt, D. Gogel , M. Kostur, P. Talkner, P. Hänggi , A. Wixforth, "Flow patterns and transport in Rayleigh surface acoustic wave streaming: combined finite element method and raytracing numerics versus experiments", IEEE Trans Ultrason Ferroelectr Freq Control. 2008 Oct;55(10):2298-305.

Authors' Vitae:

Prof. Dr. Achim Wixforth:

Dr. Wixforth graduated in physics at the University of Hamburg,Germany where he received his PhD in 1987. He spent a postdoctoral year at the University of California, Santa Barbara, where he cooperated with Profs. Gossard, Kroemer, and Petroff as an Assistant Research Engineer. Back to Germany, he received his „Habilitation" from the University of Munich in 1994 where he was senior scientist and lecturer before accepting the chair in Augsburg. He is author and co-author of more than 180 scientific papers, and looks back on a long list of invited talks. Amongst other awards he received the „Walter-Schottky-Prize" in 1998 for solid state research, one of the most prestigous scientific awards in Germany.

Prof. Achim Wixforth was co-founder and Chief Technology Officer of Advalytix AG, a spin-off company of the Center for NanoScience (CeNS) of the University of Munich. Presently, Achim is full professor for experimental physics at the University of Augsburg and member of the Cluster of Excellence „Nanosystems Initiative Munich, NIM".

Dr. Thomas Franke:

Thomas Franke received his physics diploma from University of Göttingen and Max Planck Institute of Biophysical Chemistry, Göttingen, and the Ph.D. degree from the Max-Planck-Institute of Colloids and Interfaces, Potsdam, Germany, in 2004. He was a Postdoctoral Researcher at the University of Ulm, Ulm, Germany, and later joined the Dynamics of Complex Fluids group at the Max Planck Institute for Dynamics and Self-Organization, Göttingen. Since 2005, he has been a Research Group Leader with the Chair of Experimental Physics, University of Augsburg, Augsburg, Germany. In 2008, he spent a sabbatical at the School of Engineering and Applied Sciences, Harvard University, MA. His research interests include microfluidics, cell mechanics, and complex fluids.

Mohammad Amin Fallah:

Amin is currently a Ph.D. student at the University of Augsburg, Germany. In 2005, he has received a bachelor's degree in Metallurgical Engineering from Shahid Bahonar University of Kerman, Iran. Later in 2005 he joined the master's class for materials science at the University of Augsburg, Germany, where he received his Master's degree in 2008. Since then he has been a Ph.D. student at Prof. Wixforth's chair for Experimental Physics I.

Curriculum Vitae

Persönliche Angaben

Name   Mohammad Amin Fallah

Geburtsdatum   08.05.1981

Gebortsort   Teheran, Iran

Schule

Sep 1987 - Juni 1992   Grundschule in Teheran, Iran

Sep 1992 - Juni 1995   Mittelschule in Teheran, Iran

Sep 1995 - Juni 1998   Gymnasium in Teheran, Iran

Sep 1998 - Juni 1999   voruniversitäre Bildung in Teheran, Iran

Hochschulausbildung

Sep 1999 - Mai 2005   B.Sc. Metallurgie, Kerman, Iran

Okt 2005- März 2008   M.Sc Materialwissenschaften, Augsburg, Deutschland

Masterarbeit: "SAW induced acoustic streaming in microchannels of different geometry"

seit Mai 2008   Wissenschaftlicher Mitarbeiter

Promotion in Biophysik: "Thrombocyte and Melanoma Cell Adhesion under Various Complex Flow Conditions"

03.08.2011, Augsburg